

Geometric QCD II: The Confining Twistor String and Meson Spectrum

Alexander Migdal

Institute for Advanced Study, Princeton, NJ 08540, USA

Abstract

We develop a continuum framework for confining planar QCD ($N_c \rightarrow \infty$) by quantizing the Fermi-string (1981) degrees of freedom on the rigid Hodge-dual minimal surface constructed in Geometric QCD I. The internal Majorana fermions on the worldsheet provide the algebraic mechanism required by the Makeenko–Migdal loop equations: by the Pauli principle, they enforce cancellations of non-planar self-intersection contributions, leaving the planar factorization structure. The Liouville instability of the original random-surface formulation is avoided because the bulk geometry is rigid and fixed holographically by the boundary loop, with no summation over fluctuating worldsheet metrics.

A key outcome is a formulation in momentum loop space, where coordinate-space cusp/contact singularities are integrated out, and the relevant quark-loop amplitudes admit a finite local limit. A central technical step is an explicit change of variables in the quark-loop phase-space path integral: after gauge fixing the reparametrization symmetry (Virasoro constraint), the reduced loop-space measure is parametrized by boundary twistors and an induced Jacobian, yielding a concrete twistor-string functional integral derived directly from the planar QCD amplitude rather than postulated as an abstract string model.

In the local limit, the theory becomes a confining (analytic) twistor string: a boundary sigma model $S^1 \rightarrow (S^3 \times S^3)/S^1$ coupled to a holographically determined Liouville field $\rho(z, \bar{z}) = \log(|\lambda(z)||\mu(z)|)$ obtained by analytic continuation of the boundary twistor data (Hilbert/Plemelj reconstruction).

The meson spectrum is encoded in a one-dimensional functional integral over the boundary twistor trajectory $\lambda(z), \mu(z), |z| = 1$. While we evaluate this integral numerically using a reweighted Complex Langevin approach—successfully extracting approximately linear Regge trajectories as a proof of concept—our ultimate finding is analytical. By analyzing the monodromies of complexified effective action, we reveal that the discrete mass spectrum is exactly governed by Catastrophe Theory and classified by the topological number of twistor poles inside the unit circle. The simplest sector with just one pole has the spectrum $m^2 = \pi\sigma \left(n + \frac{1}{12}\right)$.

1. Introduction

The identification of the string description of large- N_c QCD has been a central challenge of strong-interaction theory since the advent of the loop equations. At leading order in the $1/N_c$ expansion, the Makeenko–Migdal hierarchy exhibits the characteristic factorization properties of a string theory, yet a concrete, mathematically controlled continuum realization has remained elusive.

Historically, the main obstruction is the ultraviolet singular nature of the coordinate-space Wilson loop functional $W[C]$. Even after renormalization, $W[C]$ exhibits cusp and perimeter divergences, and the loop equation contains a contact term $\delta^{(4)}(x-y)$ at self-intersections. In the standard coordinate representation, this makes the local limit technically delicate and conceptually opaque: the loop

equation is local, while the perturbative solution is nonlocal and develops logarithmic singularities tied to cusp geometry.

In this paper, we adopt a different viewpoint: rather than attempting to “repair” the coordinate-space Wilson loop as an observable object, we formulate the dynamics directly in *momentum loop space*. The momentum loop functional $W[P]$ was introduced in earlier work as the functional Fourier transform of $W[C]$. Its decisive advantage is structural: the planar loop equation in momentum space becomes an exact algebraic-differential functional equation with no coordinate-space delta functions. In this representation, the geometric cusp singularities of $W[C]$ are integrated out, and the continuum equations admit a local formulation that is finite in the sense relevant for physical quark-loop amplitudes.

The goal of this second paper in the *Geometric*

Email address: amigdal@ias.edu (Alexander Migdal)

QCD series is to provide the *dynamics* that complement the *kinematics* established in Part I [1]. Part I constructs the rigid vacuum geometry: the Hodge-dual additive minimal surface $S_\chi[C]$ whose (anti)self-dual area derivative yields a zero mode of the loop operator, producing the confining dressing factor $\exp(-\kappa S[C])$. Here, we attach dynamical worldsheet degrees of freedom to this rigid background without summing over fluctuating metrics and show how the (regularized) planar loop equations are **satisfied** by this Ansatz for $W[C]$.

Our framework synthesizes three ingredients:

1. **Fermi string (“Elfin theory”).** We revisit the fermionic construction in which internal Majorana degrees of freedom on the worldsheet implement the required sign structure at intersections. In particular, the Pauli principle enforces cancellations between nonplanar intersection configurations, leaving the planar factorization pattern.
2. **Rigid Hodge-dual minimal surface.** The fermions are not placed on a random surface. Instead, they live on the rigid Hodge-dual minimal surface determined holographically by the boundary loop. This removes the dynamical Liouville instability that afflicted the original random-surface formulation: there is no summation over worldsheet metrics, and the geometry is fixed by the loop data.
3. **Momentum loop dynamics and the twistor resolution.** In momentum loop space, the loop equation becomes an exact algebraic-differential equation, stripped of coordinate-space contact singularities. We rigorously demonstrate that while this equation admits a functional Taylor-Magnus expansion at low orders, a purely one-dimensional algebraic Master Field solution violently breaks down at the eighth order ($\mathcal{W}^{(8)}$). This mathematical catastrophe proves that a 1D topological string fundamentally lacks the internal degrees of freedom to absorb the macroscopic spatial stress of Planar QCD. To resolve this geometric anomaly, the reduced loop-space measure must be parametrized by 4D continuous boundary twistor variables. This leads to an effective “analytic twistor string” description: a boundary sigma-model (a coset built from two S^3 spinors modulo a local $U(1)$) coupled to a *holographic* Liouville field whose bulk values are determined by the unique holomorphic extension of the boundary twistors.

Remark 1.1 (Equation solving vs. model building). *The starting point of this work is not a proposed “string model of QCD,” but the planar Makeenko–Migdal loop equations, treated as the nonperturbative defining equations of large- N_c*

Yang–Mills/QCD. The aim is constructive: to exhibit explicit variables and an explicit functional measure in which the loop equations admit a finite continuum solution and yield physical observables. The principal ingredients of the present construction are not adjustable assumptions. The rigid Hodge-dual minimal surface enters because strict additivity and an (anti)self-dual area derivative are algebraically required for compatibility with the loop hierarchy, while the Majorana determinant enters because its Pauli-principle sign structure enforces planar factorization.

The main technical discovery of this work is the twistorization of the reduced loop-space measure: starting from the quark-loop phase-space integral, we fix $\text{Diff}(S^1)$ by the Virasoro condition and perform a change of variables to holomorphic twistors that parametrize the rigid minimal-surface moduli. With the bulk fields reconstructed by analytic continuation from boundary data, this provides a direct, computable bridge from planar QCD amplitudes in $D = 4$ to a confining analytic twistor-string representation.

The culminating result of this paper is the exact reduction of the meson spectroscopy problem to a one-dimensional functional integral over boundary twistor data ($\lambda(z), \mu(z), |z| = 1$). While we initially evaluate this integral numerically via a reweighted Complex Langevin (CLE) approach—successfully extracting approximately linear Regge trajectories as a computational proof of concept—our ultimate finding is analytical. By evaluating the monodromies of the complexified effective action, we reveal that the discrete mass spectrum is deterministically governed by Catastrophe Theory. The path integral exactly localizes at critical resonance energies where the Lefschetz thimbles become degenerate. Because the integration variables are coupled holomorphic twistors, this degeneracy intrinsically possesses a corank of 2, mathematically upgrading generic semiclassical branch cuts into the exact simple poles of hadronic states. Planar QCD thus ceases to be a theory of stochastic quantum fluctuations; the extraction of the exact spectrum reduces to a deterministic, classical generalized eigenvalue problem. While we initially evaluate the one-dimensional functional integral over the boundary twistor trajectory numerically using a reweighted Complex Langevin approach—successfully extracting approximately linear Regge trajectories as a proof of concept—our ultimate finding in this paper is analytical.

By analyzing the monodromies of the complexified effective action, we reveal that the discrete mass spectrum is deterministically governed by Catastrophe Theory. The S -matrix poles are generated by non-compact flat valleys in the effective action, which lead to the divergence of the steepest de-

scint integral. We demonstrate that these flat valleys are dynamically produced by the multi-valued monodromy of the holomorphic twistor fields; along these winding trajectories, higher-order functional corrections to the action are strictly absent. Furthermore, the discrete spectrum is classified by the topological number of twistor poles inside the unit circle. This topological sector is rigorously protected: the crossing of the unit circle by a twistor pole leads to a divergent action, creating an impenetrable topological barrier, because the conjugate poles z_0 and $1/\bar{z}_0$ inevitably pinch the physical integration loop $|z| = 1$. By analytically continuing the action to the boundary and summing over the exact monodromy phases, we obtain an exact Bohr-Sommerfeld quantization condition. For the simplest sector with just one pole, this yields the spectrum:

$$m^2 = \pi\sigma \left(n + \frac{1}{12} \right) \quad (1.1)$$

Remarkably, the universally correct Lüscher open-string intercept $(+1/12)$ emerges directly and purely algebraically from the 2D Liouville kinetic anomaly interacting with the twistor pole monodromy, without any ad hoc assumptions of string vibrations.

Organization of the paper and navigation points.

To assist the reader in navigating the conceptual shifts and technical machinery of this framework, we have integrated our structural outline with four specific navigation points that address anticipated physical and computational questions.

Section 2 summarizes the loop-equation zero modes and recalls why the Hodge-dual minimal surface provides the appropriate rigid geometric background. For readers concerned about (i) *the physical meaning of loop-equation zero modes*, Sec. 2.3 explicitly details the underlying multi-instanton and vacuum ambiguity in loop space. Sections 3 to 9 then develop the fermionic determinant on this rigid surface and derive the corresponding loop equation, including its local limit.

Sections 10 to 12 introduce momentum loop space and the twistor string framework. To clarify (ii) *the status of Wilson-loop “renormalization,”* Sec. 10.1 sharply outlines our perspective: $W[C]$ is kept regularized at a finite Elf mass, physical observables are constructed natively in momentum loop space $W[P]$ (where coordinate-space singularities are integrated out), and only then is the local limit taken. Following this, Sections 11 to 12 execute the central change of variables. Addressing (iii) *the parametrization of the quark loop in phase space by boundary values of holomorphic twistors*, Sec. 11 details how the linear phase-space measure is transformed into twistor variables by factoring out the volume of the diffeomorphism group using the Virasoro constraint.

Section 13 discusses the semiclassical (WKB) limit and the emergence of linear Regge behavior. Section 14.1 presents the twistor-holographic (“gauge holography”) interpretation and clarifies the relation of the resulting analytic confining twistor string to standard holography and to topological twistor strings.

Then, we address (iv) *the discrete approximation and numerical implementation of the path integral*. Section 15 summarizes the CLE evaluation, while Appendix E provides exhaustive details on the CLE implementation and topological analysis. Section 16 details the unsupervised phase-information clustering used to isolate the spectral branches.

Finally, we highlight (v) *the exact analytic extraction of the mass spectrum*. Section 17.1 reformulates the whole problem of the QCD mass spectrum as a complex saddle point equation with a degenerate Hessian, corresponding to the collision of two saddle points in the spirit of Catastrophe theory. This last observation reveals the true geometric nature of Planar QCD: **the main theoretical result of this work**. Section 17.6 discusses the geometric origin of QCD, and Section 18 concludes. The remaining appendices collect vital technical material, including the exact algebraic demonstration of the $\mathcal{W}^{(8)}$ Master Field breakdown in Appendix C.

2. Zero modes of Loop equation

Let us summarize the theory of Hodge-dual minimal surfaces and its relevance to the MM loop equation. For a detailed discussion and proofs of relevant theorems, the reader may look into the latest paper [1], and the details of the new loop calculus without divergences can be found in [2, 3].

2.1. Self-dual area derivative and loop equation

Let us recall why we are looking for the self-dual minimal surface, as suggested in [2]. In this section, we follow the arguments of our recent paper [1], but our goal is not to present the Hodge-dual surface per se, but rather to view it as a hologram of the QCD string, with Fermi degrees of freedom attached.

The area derivative for a general functional $W[C]$ was defined in that paper as a discontinuity of the second variation of the area

$$\frac{\delta W}{\delta\sigma_{\mu\nu}(\theta)} = \frac{\delta^2 W}{\delta\dot{C}_\mu(\theta-0)\delta\dot{C}_\nu(\theta+0)} - \mu \leftrightarrow \nu \quad (2.1)$$

This definition implements the geometric definition of [4, 5] and is formally equivalent to the functional derivative implementation by Polyakov [6]. The crucial difference is the lack of divergences in this new definition and its unbroken parametric invariance. In the old, singular implementations, the zero

modes were obscured by kinematic divergencies, interfering with potential small-distance singularities of perturbative QCD.

The new loop equation for the Yang–Mills gradient flow was shown in [2] to reduce to the loop space diffusion equation, which allows the solution $W = \exp(-\kappa S[C])$ provided that $S[C]$ is a zero mode of this equation

$$\mathcal{L}_\nu(S) = 0; \quad (2.2)$$

$$\mathcal{L}_\nu = \left(\frac{\delta}{\delta \dot{C}_\mu(\theta+0)} - \frac{\delta}{\delta \dot{C}_\mu(\theta-0)} \right) \frac{\delta}{\delta \sigma_{\mu\nu}(\theta)} \quad (2.3)$$

The basic observation made in that paper was that there is a Hodge-dual solution similar to the Yang–Mills multi-instanton. The loop space diffusion equation (2.3) is identically satisfied for any functional $S[C]$ with self-dual (SD) or anti-dual (ASD) area derivative

$$\frac{\delta S_\pm}{\delta \sigma_{\mu\nu}(\theta)} = \pm * \frac{\delta S_\pm}{\delta \sigma_{\mu\nu}(\theta)}; \quad (2.4)$$

$$e_{\alpha\mu\nu\lambda} \left(\frac{\delta}{\delta \dot{C}_\alpha(\theta+0)} - \frac{\delta}{\delta \dot{C}_\alpha(\theta-0)} \right) \frac{\delta S_\pm}{\delta \sigma_{\mu\nu}(\theta)} \equiv 0; \quad (2.5)$$

The last equation (Bianchi identity) is valid at the kinematical level as a Jacobi identity for a triple commutator (see [2] for a proof). The matrix in the Dirichlet boundary conditions (BC) for $X \sim QC$ should be chosen so that the area derivative represents the SD or ASD tensor. This choice would make the exponential of the Hodge-dual minimal area an exact solution to the loop equation.

The existence of this zero mode is based on the so-called Leibniz property of the loop operator and similar singular loop operators in loop calculus.

$$\mathcal{L}_\nu f(\Phi[C]) = f'(\Phi[C]) \mathcal{L}_\nu \Phi[C]; \quad (2.6)$$

$$\mathcal{L}_\nu(A[C]B[C]) = \mathcal{L}_\nu(A[C])B[C] + A[C]\mathcal{L}_\nu(B[C]) \quad (2.7)$$

It was heuristically claimed in the original MM papers [7, 5], and rigorously proven in the loop calculus [2], section 3, eqs (39), (40). Due to the Leibnitz property,

$$\begin{aligned} \mathcal{L}_\nu(\exp(-\kappa S[C]) W_0[C]) &= \\ -\kappa \mathcal{L}_\nu(S[C]) \exp(-\kappa S[C]) W_0[C] &+ \\ + \exp(-\kappa S[C]) \mathcal{L}_\nu(W_0[C]) &= \exp(-\kappa S[C]) \mathcal{L}_\nu(W_0[C]) \end{aligned} \quad (2.8)$$

We are looking for such a self-dual minimal surface which is *additive* at the self-intersecting loops. This condition will be discussed in detail below. It is critical for the whole theory—due to this additivity, the confining factor $\exp(-\kappa S[C])$ is compatible with the whole chain of the loop equations.

2.2. Compatibility with the MM loop equations.

The full chain of loop equations for the Wilson loops with a finite number of colors N_c [7, 5] has

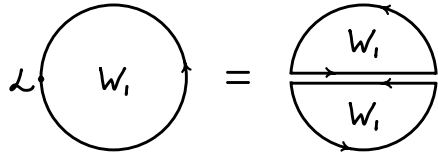


Figure 1: The MM equation, with the loop diffusion operator on the left side, and the integral term on the right side. The double line on the right stands for the delta function $\delta^4(x-y)$ enforcing self-intersection.

the same loop operator (2.3) as the Yang–Mills gradient flow, except there is no time derivative. In this paper, we are only considering the leading order of the $1/N_c$ expansion. We use the **loop calculus** developed in the paper [2], as it applies to the loop diffusion operator (2.3), which is the same in the multiloop MM chain and in the Yang–Mills gradient flow equation. The MM loop equation has the structure (see Fig.1)

$$W[C] = 1/N_c \left\langle \text{tr} \hat{P} \exp \left(\oint_C dx_\mu A_\mu(x) \right) \right\rangle; \quad (2.9)$$

$$\mathcal{L}_\nu(W[C]) = \lambda \int_C dy_\nu \delta^4(x-y) W[C_{xy}] W[C_{yx}] \quad (2.10)$$

Here $\lambda = N_c g_0^2$ is the 't Hooft's coupling constant in the limit of $N_c \rightarrow \infty$. This equation is singular at self-intersections, so it must be understood in the sense of distributions in loop space. It is manifestly parameterization-invariant, and the confining factor $\exp(-\kappa S[C])$ factors out from the right side by additivity of $S[C]$ and cancels with the same factor on the left side.

Let us stress that this factorization takes place *independently* of the splitting points $x, y \in C$. For every self-intersection $x, y \in C$ such that $C(x) = C(y)$, the product of two factors $\exp(-\kappa S[C_{xy}])$ and $\exp(-\kappa S[C_{yx}])$ exactly equals the factor $\exp(-\kappa S[C])$ on the left side of the MM equation; Thus, it can be taken out of the integral, after which it cancels on both sides of the MM equation.

The *physical hypothesis* of that paper was that the actual gluonic vacuum of QCD is described by this dressed solution, choosing the "fluctuative" factor W_{fluct} as the seed. While the symmetry is exact, the separation into a fluctuative factor and a purely geometric area law is ambiguous. It is physically most distinct in the *large-loop limit*, where the area term dominates over W_{fluct} , which is assumed only to contribute the term proportional to a perimeter of the loop.

In the present paper, we construct an explicit solution for this factor W_{fluct} , adapting the fermionic determinant from the '81 paper [8] to the Hodge-dual minimal surface instead of a random surface, assumed in that work. The confining factor becomes the vacuum energy of that rigid Fermionic

string, and planar graphs emerge as a strong coupling expansion of that 2D fermi system in terms of a sum over fermionic loops on a Hodge-dual minimal surface. The Pauli principle leads to repulsion of these loops, making them topologically equivalent to planar graphs of QCD.

The comparison of the contour equation for these fermionic determinants from the '81 work with the MM equation establishes the correspondence between the 't Hooft coupling constant λ and the parameters of the Elfin theory (the bare fermionic mass and the vacuum energy).

2.3. The Physical Vacuum and Multi-Instanton Resummation

Before we formulate the dynamics of the Fermi string on the minimal surface, we must clarify the physical origin of this rigid geometric background. The Makeenko-Migdal (MM) loop equations serve as the exact quantum equations of motion for Planar QCD. Like any equations of motion, they possess an inherent ambiguity corresponding to the choice of the physical vacuum. The mathematical freedom to multiply the perturbative loop functional by a zero mode exactly reflects this physical vacuum ambiguity.

In the traditional gauge-field picture, the nonperturbative QCD vacuum is a highly complex mixed state, often modeled as a nontrivial distribution in the multi-instanton space. Because any single multi-instanton solution explicitly breaks translation invariance by localizing topological charge at specific spacetime points, restoring Poincaré symmetry requires an exceedingly complicated integration over the entire multi-instanton moduli space (positions, sizes, and color orientations).

The loop-space formulation achieves this summation geometrically. Just as instantons are characterized by the self-duality of the gauge field strength ($F_{\mu\nu} = \pm * F_{\mu\nu}$), our exact zero mode is characterized by the self-duality of the loop-space area derivative.

Thus, the complex mixed state of multi-instantons in coordinate space simplifies to a single, fully translation-invariant, exact geometric object in loop space: the Hodge-dual minimal surface.

Note that the mere Hodge duality condition leaves the freedom of an arbitrary topological charge and arbitrary moduli of the multi-instanton solution. Therefore, our Hodge-dual minimal surface, by satisfying this requirement, represents a general statistical mixture of multi-instanton solutions, implicitly summed over topological charges and integrated over moduli with some unknown measure. This implicit integration is precisely what provides the exact translation invariance and spatial isotropy of the minimal area solution. The profound advantage of the loop-space approach is

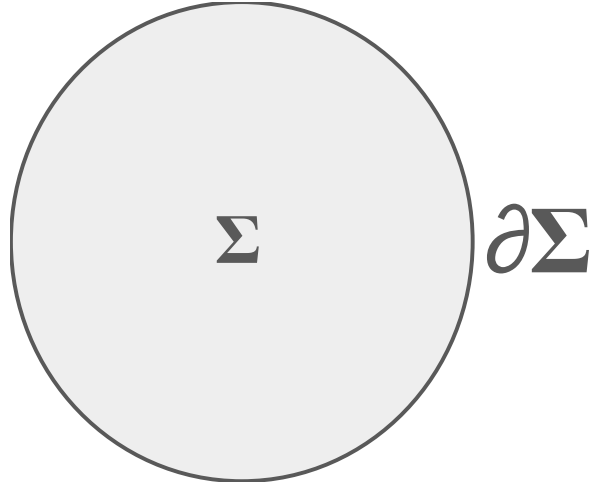


Figure 2: The unit disk Σ is mapped to $\mathbb{R}^3 \otimes \mathbb{R}^4$ and then projected to \mathbb{C}^4 by a holomorphic map, minimizing the area functional.

that we do not need to know the explicit details of this distribution of topological charge and multi-instanton moduli: the loop equations can be solved directly without ever specifying this measure.

Therefore, the rigid background upon which our worldsheet fermions propagate is not merely a mathematical ansatz. It is the exact holographic representation of the translation-invariant, nonperturbative QCD vacuum, naturally incorporating the sum over topological sectors that is analytically prohibitive in the standard gauge-field path integral.

3. Hodge-dual minimal surface

Now, we are going to define the solvable functional $S[C]$ satisfying both the duality and additivity. We are following the definitions and derivations from [1], adapting them for the present purpose of a base for the fermions living on that minimal surface.

3.1. The external and internal geometry

We define the surface coordinates $X_\mu^i(\xi)$ (for $\xi = (\xi_1, \xi_2)$, $i = 1, 2, 3$).¹ The field $X_\mu^i(\xi)$ maps the disk Σ (Fig 2) to $\mathbb{R}^3 \otimes \mathbb{R}^4$. Our surface area is defined as

$$S_\chi[C] = \min_X \int_\Sigma d^2\xi \sqrt{\Sigma_{\mu\nu}^2/2}; \quad (3.1)$$

¹This surface was first proposed in [2] as a zero-mode of the loop operator in the context of the Yang-Mills gradient flow, but unfortunately, the wrong number of components (four instead of three) was chosen for the X_μ^A , $A = 1, 2, 3, 4$. The rest of the theory in that paper was validated by our recent work [1], including the loop calculus and the Hodge-duality of the minimal surface.

The area element is defined as

$$\Sigma_{\mu\nu} = \epsilon_{ab} \partial_a X_\mu^i \partial_b \bar{X}_\nu^i; \quad (3.2)$$

The Hodge chirality $\chi = \pm 1$ enters through the boundary conditions

$$X_\mu^i(\partial\Sigma) = \eta_{\mu\nu}^{\chi,i} C_\nu; \quad (3.3)$$

Here $\eta_{\mu\nu}^{\chi,i}$ are 't Hooft's matrices corresponding to Hodge duality $\chi = \pm 1$

$$\eta_{\mu\nu}^{\chi,i} = \delta_{i\mu} \delta_{\nu 4} - \delta_{i\nu} \delta_{\mu 4} + \chi \epsilon_{i\mu\nu 4}; \quad (3.4)$$

The coordinate functions $X_\mu^a(\xi)$ satisfy the general Euler-Lagrange equations for the area density $\mathcal{L} = \sqrt{\Sigma^2}/2$:

$$[\text{E-L Equations}]_\mu^a = \epsilon_{lm} \partial_l \left(\frac{\Sigma_{\mu\nu} \partial_m X_\nu^a}{\sqrt{\Sigma^2}} \right) = 0. \quad (3.5)$$

Assuming the bulk variation vanishes by the Euler-Lagrange equations, we use Stokes theorem and get the boundary term

$$\delta S = 2 \int d\theta \frac{\delta X_\mu^i \Sigma_{\mu\nu} \partial_\theta X_\nu^i}{\sqrt{\Sigma^2}} \quad (3.6)$$

Substituting the boundary conditions (3.3) for δX , $\partial_\theta X$ and summing over $a = 1, 2, 3$ we find

$$\delta S = -2 \int d\theta \frac{\delta C_\mu \Sigma_{\mu\nu} \partial_\theta C_\nu}{\sqrt{\Sigma^2}}; \quad (3.7)$$

$$\frac{\delta S}{\delta \sigma_{\mu\nu}} = -2 T_{\mu\nu}; \quad (3.8)$$

$$T_{\mu\nu} = \frac{\Sigma_{\mu\nu}}{\sqrt{\Sigma^2}} \quad (3.9)$$

Note the change of sign, compared with the ordinary area derivative of the minimal surface in four Euclidean dimensions.

Regardless of this sign change, the Hodge duality of the area element Σ with these boundary conditions for a generic field $X_\mu^a(z, \bar{z})$ leads to the same Hodge duality of the area derivative.

This self-duality of the area derivative makes our Hodge-dual minimal area a zero mode of the loop diffusion operator, leading to the solution of the MM loop equations [7, 5], as we argue in the next section.

Note that this area functional is invariant under the reparametrizations of the boundary loop $\delta_{\text{param}} C_\mu(\theta) = \epsilon(\theta) \partial_\theta C_\mu(\theta)$

$$\delta_{\text{param}} S = -2 \int d\theta \epsilon(\theta) \frac{\partial_\theta C_\mu \Sigma_{\mu\nu} \partial_\theta C_\nu}{\sqrt{\Sigma^2}} = 0 \quad (3.10)$$

by the skew symmetry of $\Sigma_{\mu\nu}$.

The Hodge-dual area is defined as a minimum of this functional under an extra duality constraint

$$*\Sigma_{\mu\nu} \equiv \frac{1}{2} \epsilon_{\mu\nu\alpha\beta} \Sigma_{\alpha\beta} = \chi \Sigma_{\mu\nu} \quad (3.11)$$

In the previous papers [2, 1], we found a complete solution for the Hodge-dual surface in terms of holomorphic map.

3.2. The Holomorphic Map

We resolve the duality constraint using the following holomorphic Ansatz:

$$X_\mu^i = \eta_{\mu\nu}^{\chi,i} Y_\nu \quad (3.12)$$

$$Y_\mu = f_\mu(z) + \bar{f}_\mu(\bar{z}); \quad (3.13)$$

$$z = \xi_1 + i\xi_2; \quad (3.14)$$

Geometrically, this is a projection from $\mathbb{R}^3 \otimes \mathbb{R}^4$ to \mathbb{C}^4 . The boundary conditions for the Hodge-dual surface become a conventional boundary condition for the Dirichlet problem

$$2 \text{Re } f_\mu(e^{i\theta}) = C_\mu(\theta) \quad (3.15)$$

So, we have a line in four dimensional complex space $f \in \mathbb{C}^4$. Our surface area (3.1) reduces to the induced metric in this space

$$\Sigma_{\mu\nu} = 2(F_{\mu\nu} + \chi * F_{\mu\nu}); \quad (3.16)$$

$$F_{\mu\nu} = i(f'_\mu \bar{f}'_\nu - \bar{f}'_\mu f'_\nu); \quad (3.17)$$

$$\sqrt{\Sigma_{\mu\nu}^2}/2 = 2\sqrt{2} \sqrt{-\det g}; \quad (3.18)$$

$$g_{ab} = \partial_{z_a} Y_\mu \partial_{z_b} Y_\mu; \quad z_a, z_b = (z, \bar{z}) \quad (3.19)$$

This area element is Hodge-dual

$$*\Sigma_{\mu\nu} = \chi \Sigma_{\mu\nu} \quad (3.20)$$

for arbitrary functions $f_\mu(z)$.

This duality condition, as argued above, together with the above boundary conditions, provides the self-duality of the area derivative of the minimal area. The self-duality of the area derivative follows from the general formula for variation of the surface $X_\mu^a(\xi)$ with area (3.1), projected on the holomorphic Ansatz.

3.3. The Virasoro Constraint and Uniformization

We further impose a Virasoro constraint on the holomorphic maps derivatives

$$f'_\mu(z)^2 = 0 \quad (3.21)$$

The imposition of the null constraint $(f')^2 = 0$ is not an approximation but a rigorous gauge fixing procedure rooted in the geometric symmetries of the problem.

The physical starting point is the geometric Area functional, $S = \int \sqrt{-\det g} d^2z$, which possesses full reparametrization invariance under general diffeomorphisms $z \rightarrow w(z, \bar{z})$. This infinite symmetry group allows us to choose a specific coordinate system on the world-sheet without altering physical results.

We choose to work in **isothermal (conformal) coordinates**, where the induced metric is diagonal:

$$ds^2 = \rho(z, \bar{z}) dz d\bar{z} \implies g_{zz} = \partial_z Y \cdot \partial_z Y = 0 \quad (3.22)$$

For our specific ansatz (3.12), the metric component g_{zz} is explicitly proportional to the square of the holomorphic derivative:

$$g_{zz} = (f'_\mu)^2 = 0 \quad (3.23)$$

Thus, the geometric condition of conformal gauge fixing $g_{zz} = 0$ is algebraically equivalent to the null constraint $(f')^2 = 0$.

The existence of such a coordinate system for any surface topology is guaranteed by the **Uniformization Theorem** [9]. This theorem ensures that we are always free to set $(f')^2 = 0$ by a suitable diffeomorphism. In this gauge, the non-linear geometric area density simplifies exactly to the quadratic Lagrangian:

$$\mathcal{L} = \sqrt{-\det g} = \sqrt{(g_{z\bar{z}})^2 - |g_{zz}|^2} \xrightarrow{(f')^2=0} g_{z\bar{z}} \propto |f'|^2 \quad (3.24)$$

This reduction allows us to describe the Minimal Surface using the linear Laplace equation for f_μ , subject to the Virasoro constraint. To summarize, we have found that

$$S_\chi[C] = 2\sqrt{2} \int_D |f'(z)|^2 d^2z; \quad (3.25)$$

$$\frac{\delta S_\chi[C]}{\delta \sigma_{\mu\nu}} = -2 \frac{\Sigma_{\mu\nu}}{\sqrt{\Sigma_{\mu\nu}^2}} \quad (3.26)$$

The solution of the linear boundary problem (3.15) for a holomorphic vector function is given by the Hilbert transform

$$f_\mu = \frac{1}{2}(1 + i\mathcal{H})C_\mu; \quad (3.27)$$

$$H[u](\theta) = \frac{1}{2\pi} \text{P.V.} \int_0^{2\pi} d\theta' \cot\left(\frac{\theta - \theta'}{2}\right) u(\theta') \quad (3.28)$$

$$\int_D |f'(z)|^2 d^2z = \int_0^{2\pi} d\theta C'_\mu(\theta) H[C_\mu](\theta); \quad (3.29)$$

In terms of the Taylor coefficients

$$f_\mu(z) = \sum_{n>0} z^n C_{\mu,n}; \quad (3.30)$$

$$C_\mu(\theta) = \sum_{n=-\infty}^{\infty} e^{in\theta} C'_{\mu,n} \quad (3.31)$$

In the presence of the Virasoro constraint (3.21), the problem becomes a challenging one and has been investigated over the last two centuries by great mathematicians, starting with Riemann and Hilbert. We give a brief summary of modern state of this theory in Appendix Appendix B.

In Part I [1], we compared the ordinary minimal surface in four dimensions with the Hodge-dual one. This comparison reveals some hidden variables present in the area derivatives of the Hodge dual surface, but not in the extremal value of this

area. This minimal value up to a normalization factor $2\sqrt{2}$ equals that of the so called Goldschmidt solution [10, 12, 13] for the Plateau problem. This additive solution represents a local minimum of the Dirichlet functional, with the simplest topology (collection of disks one for each closed part of C).

The area derivatives for the Goldschmidt minimal area and Hodge dual minimal area are different (the second one being SD or ASD component of the first). The apparent paradox is resolved by the obvious fact that the area derivative of a functional equals the skew-symmetric part of its *second* functional derivative, but only the extremal value and its first derivative ($= 0$) coincide for the functional and its minimal value.

Also, the Hodge-dual surface is not parity-symmetric, but its minimal value (minimal area) is. The chirality χ manifests itself in the *external* geometry of this minimal surface $X_\mu^i \in \mathbb{R}^3 \otimes \mathbb{R}^4$, including its area derivative, but its *internal* geometry is determined by the induced metric (3.22),(3.23), which is the only local function related to surface embedding. Moreover, this metric in the holomorphic map that minimizes the area depends only on the bounding loop C , through the holomorphic vector function $f_\mu(z)$, which solves the Riemann-Hilbert problem (9.4), (3.30). This dependence is *identical* for the Hodge-dual surface and the Goldschmidt solution for the Plateau problem in 4D, bounded by C .

The last property (the identity of the internal geometry in the Hodge-dual surface in relation to that of the 4D Euclidean problem) will play an important role in proving the MM equation for the fermionic determinant. The only remnants of the Hodge-duality are the overall negative sign and the χ -term in the area derivative (3.26) projecting it on the Hodge-dual sector of skew-symmetric tensors in 4D.

4. The Elfin theory on a flat surface

In this section, we deal with the Elfin theory by itself, without any reference to the gauge theory. The equivalence of these theories will be established in the next sections.

Let us consider the flat surface bounded by some contour C . Later, we generalize this to the Hodge-dual minimal surface. All the functionals on the surface will depend on the conformal factor in the mass term

$$e = \partial_+ X_\mu^i \partial_- X_\mu^i. \quad (4.1)$$

On the minimal surface, we have a conformal map (3.12), reducing the conformal metric to $e = 2\sqrt{2}|f'_\mu|^2$. This reduction is not needed for the general theory of fermions on the minimal surface, but it will be used in the forthcoming sections

when we establish a relation between the fermionic determinants and the MM loop equation.

Remark 4.1 (Holes, poles, and global signs). *Multiply connected worldsheets (holes/handles) may require multivalued primitives $f_\mu(z) = \int^z f'_\mu(\zeta) d\zeta$ (logarithms/periods), even when the tangents f'_μ are single-valued meromorphic. In the applications to the QCD spectrum, we allow such meromorphic f'_μ with poles in the unit disk; the induced conformal factor $e(z, \bar{z}) \propto |f'_\mu(z)|^2$ is single-valued but may diverge at these poles.*

This does not invalidate the analysis of the Elfin determinant in the flat gauge: closed fermion paths are weighted by $\exp(-m \int_\Gamma \sqrt{e} |dz|) = \exp(-m \ell_\Gamma)$, hence any path approaching a pole (where $\sqrt{e} \sim |z-w|^{-1}$ for a simple pole of f') has $\ell_\Gamma \rightarrow \infty$ and is exponentially suppressed. Since ℓ_Γ is a local additive functional, the length weights of the locally paired configurations (touching vs. intersecting) coincide, while their mod-2 intersection signs are opposite, yielding the same cancelation mechanism.

Finally, while handles do not affect the local turning-angle contribution to the loop sign, they can affect global signs of the fermion propagator/determinant (spin-structure/holonomy) and complicate the topological analysis of the corresponding minimal-surface embeddings.

Let us now return to the flat surface and introduce the Elfin field as a bispinor

$$\psi = \psi_\lambda^\alpha(\xi), \quad \alpha = 1, 2, \quad \lambda = \pm 1. \quad (4.2)$$

There are various equivalent forms of the action. The simplest form reads

$$A_0 = \int d^2\xi (\bar{\psi}_\lambda \sigma^k \partial_k \psi_\lambda + \bar{\psi}_\lambda \psi_\lambda m \sqrt{e}), \quad (4.3)$$

where σ_1, σ_2 are the Pauli matrices. We shall also use the complex components

$$\sigma_\pm = \frac{1}{2}(\sigma_1 \pm i\sigma_2); \quad (4.4)$$

$$\partial_\pm = \partial_1 \pm i\partial_2; \quad (4.5)$$

$$\psi_\lambda^\pm = \frac{1}{2}(1 \pm \sigma_3)\psi_\lambda. \quad (4.6)$$

$$\bar{\psi}_\lambda^\pm = \psi_\lambda^\dagger \frac{1}{2}(1 \pm \sigma_3). \quad (4.7)$$

This action is covariant with respect to conformal transformations

$$e(\xi_+, \xi_-) \rightarrow f'_+(\xi_+) f'_-(\xi_-) e(f_+, f_-), \quad (4.8)$$

$$\psi_\lambda^\pm(\xi) \rightarrow \sqrt{F'_\pm} \psi_\lambda^\pm(f), \quad (4.9)$$

$$\bar{\psi}_\lambda^\pm(\xi) \rightarrow \sqrt{F'_\mp} \bar{\psi}_\lambda^\pm(f); \quad (4.10)$$

At the boundary $\dot{\Sigma}$, we require that the spin σ_3 takes definite values, namely:

$$\sigma_3 \psi_\lambda = \lambda \psi_\lambda, \quad \text{at } \partial\Sigma, \quad (4.11)$$

$$\bar{\psi}_\lambda \sigma_3 = \lambda \bar{\psi}_\lambda, \quad \text{at } \partial\Sigma. \quad (4.12)$$

In other words, at the boundary

$$\psi_+^- = \psi_-^+ = \bar{\psi}_+^- = \bar{\psi}_-^+ = 0. \quad (4.13)$$

Such "chiral bag" boundary conditions were studied in the mathematical literature [14] in the context of the Atiyah-Singer Index Theorem. For our purposes, it is sufficient to note that these boundary conditions are consistent with the topology of the Dirac path integral below.

The remaining half of the components is not restricted at the boundary. In the Schrödinger picture in Minkowski space this implies that the states with $\sigma_3 = \pm 1$ at both ends of the string are occupied. Such peculiar boundary conditions are necessary to obtain the closed loop equations (see below). Note that these boundary conditions are conformally invariant and do not depend on the form of the boundary.

At the "time" reflection

$$\xi_2 \rightarrow -\xi_2 \quad \text{or} \quad \xi_+ \leftrightarrow \xi_- \quad (4.14)$$

the spin σ_3 changes the sign. According to our boundary conditions, this should be accompanied by a change of sign of λ :

$$\psi_\lambda \rightarrow \psi_{-\lambda} \sigma_3. \quad (4.15)$$

One may introduce the oriented states

$$\psi_\lambda^{R,L} = \psi_\lambda^{\pm\lambda}, \quad (4.16)$$

$$\bar{\psi}_\lambda^{R,L} = \bar{\psi}_\lambda^{\mp\lambda}. \quad (4.17)$$

The left-hand states are occupied at the boundary. As we shall see, the orientation $\lambda\sigma_3$ is related to the orientation of the loop C . The right-hand and left-hand states interchange when the loop is reoriented.

The action can be rewritten in the Left-Right (chiral) form. Based on the transformation properties in equations (4.16) and (4.17), and using the identity $\sigma^k \partial_k = \sigma_+ \partial_+ + \sigma_- \partial_-$, the action becomes:

$$A_0 = \int d^2\xi [\bar{\psi}^R \partial_+ \psi^L + \bar{\psi}^L \partial_- \psi^R + m \sqrt{e} (\bar{\psi}^R \psi^R + \bar{\psi}^L \psi^L)]. \quad (4.18)$$

In this form, the conformal properties are manifest. Under the transformations $\xi_+ \rightarrow f_+(\xi_+)$ and $\xi_- \rightarrow f_-(\xi_-)$ the kinetic term transforms as:

$$\begin{aligned} & \left(\sqrt{f'_-} \bar{\psi}^R \right) (f'_+ \partial_+) \left(\sqrt{f'_-} \psi^L \right) \\ &= f'_- f'_+ (\bar{\psi}^R \partial_+ \psi^L); \end{aligned} \quad (4.19)$$

$$\begin{aligned} & \left(\sqrt{f'_+} \bar{\psi}^L \right) (f'_- \partial_-) \left(\sqrt{f'_+} \psi^R \right) \\ &= f'_- f'_+ (\bar{\psi}^L \partial_- \psi^R). \end{aligned} \quad (4.20)$$

The mass term transforms as:

$$\begin{aligned}
& (\sqrt{f'_+ f'_-} \sqrt{e}) \left(\sqrt{f'_-} \bar{\psi}^R \right) \left(\sqrt{f'_+} \psi^R \right) \\
&= (f'_+ f'_-) \sqrt{e} \bar{\psi}^R \psi^R; \\
& (\sqrt{f'_+ f'_-} \sqrt{e}) \left(\sqrt{f'_+} \bar{\psi}^L \right) \left(\sqrt{f'_-} \psi^L \right) \\
&= (f'_+ f'_-) \sqrt{e} \bar{\psi}^L \psi^L. \tag{4.21}
\end{aligned}$$

This factor of $(f'_+ f'_-)$ exactly cancels the Jacobian from the measure $d^2\xi$, making the kinetic energy as well as the mass term conformally invariant.

Note that the Lagrangian density is invariant with respect to internal $U(1) \times SU(2)$ transformations:

$$\psi_\lambda \rightarrow S_{\lambda\lambda'} \psi_{\lambda'} e^{i\alpha}, \tag{4.22}$$

$$\bar{\psi}_\lambda \rightarrow \bar{\psi}_{\lambda'} (S^{-1})_{\lambda'\lambda} e^{-i\alpha}. \tag{4.23}$$

However, the boundary conditions lower this symmetry down to $U_+(1) \times U_-(1)$:

$$\psi^\pm \rightarrow \psi^\pm e^{i\alpha^\pm}, \tag{4.24}$$

$$\bar{\psi}^\pm \rightarrow \bar{\psi}^\pm e^{-i\alpha^\pm}. \tag{4.25}$$

Both $U(1)$ currents vanish at the boundary:

$$j_k = \bar{\psi}^\pm \sigma_k \psi^\pm = 0 \quad \text{at } \dot{\Sigma}; \quad k = 1, 2. \tag{4.26}$$

So, there is no flow outside. The derivative ∂_k in (2.11) can be replaced by D_k , since the boundary terms vanish.

At vanishing mass m the theory possesses chiral σ_3 invariance, which is not violated by any anomaly.

Let us now discuss the symmetry of the physical x -space. As usual in string theory, the transformations of the internal coordinates ξ have nothing to do with the physical rotations in x -space. From the viewpoint of two-dimensional field theory in ξ -space, the rotations in x -space represent internal $O(4)$ symmetry transformations of the C_μ field,

$$\delta C_\mu = \omega_{\mu\nu} C_\nu. \tag{4.27}$$

The Elf does not transform:

$$\delta \psi_\lambda = \delta \bar{\psi}_\lambda = 0. \tag{4.28}$$

This follows from the boundary conditions. The full target surface field X_μ^i transforms as one of the $SO(3)_\pm$ subgroups of $SO(4)$

$$X_\mu^i \Rightarrow \Omega_{ij}^\pm X_\nu^j W_{\nu\mu}; \quad \Omega^\pm \in SO(3), \quad W \in SO(4) \tag{4.29}$$

Consider now local variations of the loop C . The area derivative of e can be found from the known variation of the scalar area

$$|S| = \int_S d^2\xi e = \int_S d\sigma_{\mu\nu}(\xi_1) d\sigma_{\mu\nu}(\xi_2) \delta_{inv}(\xi_1 - \xi_2); \tag{4.30}$$

$$\begin{aligned}
\frac{\delta|S|}{\delta\sigma_{\mu\nu}(\xi_1)} &= \int d^2\xi_2 \frac{\delta e}{\delta\sigma_{\mu\nu}(\xi_2)} \\
&= 2 \int_S t_{\mu\nu}(\xi_2) d^2\xi_2 \delta(\xi_1 - \xi_2) \tag{4.31}
\end{aligned}$$

Using the exact area derivatives of the Hodge-dual minimal area established in the previous section, we find for the area derivative of

$$\frac{\delta e(\xi)}{\delta\sigma_{\mu\nu}(\xi_0)} = -2T_{\mu\nu} \delta^2(\xi - \xi_0); \tag{4.32}$$

$$T = \frac{F + \chi * F}{\sqrt{2F^2}} \tag{4.33}$$

$$\frac{\delta \langle \exp(A_0) \rangle}{\delta\sigma_{\mu\nu}} = -2m \left\langle \frac{T_{\mu\nu} \bar{\psi} \psi}{\sqrt{e}} \right\rangle_{\partial\Sigma} \tag{4.34}$$

where F is given by (3.26). According to our boundary conditions, only the right-hand components are present in (4.34):

$$\bar{\psi} \psi = \bar{\psi}^R \psi^R \quad \text{at } \dot{\Sigma}. \tag{4.35}$$

5. Conformal metric as a local gauge parameter

We begin by defining the effective action for the elf (Majorana fermion) field on a two-dimensional surface S with metric

$$g_{ab} = \exp(2\rho) \delta_{ab},$$

including the mass term and the dependence on the conformal factor ρ . We are reproducing here the construction in Eqs. (2.57)–(2.63) of [8].

The action of the general theory is given by

$$\begin{aligned}
A_\rho &= \int d^2\xi \\
&\left(e^{2\rho} \bar{\psi}_\lambda \sigma^k e^{-\rho} \nabla_k \psi_\lambda + m \sqrt{e} e^\rho \bar{\psi}_\lambda \psi_\lambda - \frac{\partial_+ \rho \partial_- \rho}{3\pi} \right); \tag{5.1}
\end{aligned}$$

with the spinor connection ω_k :

$$\nabla_k = \partial_k + \frac{i}{2} \omega_k \sigma^3, \tag{5.2}$$

vierbein

$$E_k^a = \delta_k^a e^\rho, \tag{5.3}$$

and curvature

$$\hat{R}_{kl} = [\nabla_k, \nabla_l] = i\sigma_3 e_{kl} R \det E; \tag{5.4}$$

$$R = -8e^{-2\rho} \partial_+ \partial_- \rho. \tag{5.5}$$

At $\rho = 0$ this is the old action A_0 , whereas at $\rho = \ln \sqrt{e}$ this is the action of the Dirac particle with constant mass at the surface S with the induced metric g_{ab} .

Theorem 5.1 (Conformal Invariance of the Elf Determinant). *The functional integral*

$$Z[S|e, \rho] = \int \mathcal{D}\bar{\psi} \mathcal{D}\psi \exp(A_\rho) \tag{5.6}$$

is invariant under local variations of the conformal metric field ρ . That is, the theory depends only on the conformal class (moduli) of the surface, and the induced metric $e(\xi)$ but not on the local gauge parameter $\rho(\xi)$.

Proof. The main point here is the covariant regularization of the Dirac theory at the surface. We have to define the divergent trace in the vacuum amplitude

$$\int \mathcal{D}\bar{\psi}\mathcal{D}\psi \exp(A_\rho) = \exp\left(-\int d^2\xi \frac{(\partial\rho)^2}{3\pi}\right) + \text{tr}_+ \log(i\hat{D}_\rho + m\sqrt{e}e^{-\rho}) + \text{tr} \log(i\hat{D}_\rho + m\sqrt{e}e^{-\rho}). \quad (5.7)$$

Here

$$\hat{D}_\rho = \sigma^k e^{-\rho} (-i\partial_k \omega_k), \quad (5.8)$$

is the covariant Dirac operator, and the subscript + conditions $\sigma^3 = +1$.

We employ the Pauli-Villars regularization in the following form:

$$\begin{aligned} & \text{tr} \ln(i\hat{D}_\rho + m\sqrt{e}e^{-\rho})_{\text{reg}} \\ &= \text{tr} \left[\ln(i\hat{D}_\rho + m\sqrt{e}e^{-\rho}) - \frac{1}{2} \sum_i c_i \ln(\hat{D}_\rho^2 + M_i^2) \right], \\ & \sum_i c_i = 1. \end{aligned} \quad (5.9)$$

The shift of the ρ field

$$\rho \rightarrow \rho + \delta\rho \quad (5.10)$$

results in the multiplicative transformation of the Dirac operator

$$\hat{D}_\rho \Rightarrow e^{-\frac{3}{2}\delta\rho} \hat{D}_\rho e^{-\frac{1}{2}\delta\rho}. \quad (5.11)$$

Therefore, the variation of the regularized determinant reads

$$\begin{aligned} & \text{tr} \left[-\delta\rho + 2 \sum_i c_i \left(\delta\rho \frac{M_i^2}{M_i^2 + \hat{D}_\rho^2} \right) \right] \\ &= -\text{tr} \left(\delta\rho \sum_i c_i \frac{M_i^2}{M_i^2 + \hat{D}_\rho^2} \right). \end{aligned} \quad (5.12)$$

The WKB calculations of [8] (reproduced here in the Appendix) yield

$$\int d^2\xi e^{2\rho} \delta\rho \frac{R}{24\pi} = \delta \int d^2\xi \frac{\partial_+ \rho \partial_- \rho}{6\pi}. \quad (5.13)$$

Therefore, the variations of terms in the exponential cancel each other, as claimed. \square

Corollary 5.1. *As a consequence of this theorem, the theory of massive Majorana fermions on a minimal surface with induced metric $g_{ab} = \delta_{ab}e(\xi)$, and extra conformal term $-\frac{(\partial\rho)^2}{3\pi}$ in Lagrangian is equivalent to the theory of Majorana fermions on a flat surface with variable mass $m\sqrt{e(\xi)}$. The first theory corresponds to taking $\rho = \log \sqrt{e}$ in A_ρ , and the second theory corresponds to taking $\rho = 0$. By the proven gauge invariance these theories are equivalent.*

Remark 5.1 (Moduli and Topology). *The theorem establishes local independence from $\rho(\xi)$. For a disk, all metrics are conformally equivalent to the flat metric, so the determinant is a unique functional of external loop via the conformal metric $e = |f'_\mu|^2$. For surfaces with handles or holes, the metric can be written as*

$$g_{ab} = \exp(2\rho) \hat{g}_{ab}(\tau),$$

where τ are the Teichmüller parameters (moduli). The determinant then depends on τ , i.e., $Z_{\text{elf}}[C] = Z[C|\tau]$. In the present geometric theory, the minimal surface is rigid: the boundary loop C uniquely determines the solution to the Plateau problem and thus fixes the moduli $\tau = \tau[C]$. Therefore, the Dirac determinant is a well-defined functional of C , encoding the "gluon cloud" effects for the specific minimal surface spanned by C . In the degeneration limit (e.g., infinitesimal bridges), the moduli approach a boundary value, but the locality of the loop equation is preserved.

6. The fermion determinants and the planar topology

Let us consider the vacuum functional Z of the Elfin theory with the boundary conditions discussed in the previous sections. By virtue of conformal invariance, we can choose the local gauge $\rho(\xi) = \log \sqrt{e(\xi)}$ or $\rho(\xi) = 0$. The following analysis of the vacuum loops in this theory simplifies in the gauge $\rho = 0$, where it is similar to the topological solution of the 2D Ising model.

As a functional of the loop C , the vacuum functional satisfies a certain non-linear path integral equation. This equation will be derived in this section and investigated in the following sections.

6.1. Mathematical justification of the signed sum over loops

The path integral representation of the Dirac determinant on a finite surface with boundary conditions, as employed in this work, is rigorously justified by several mathematical results and earlier physical constructions. In particular, Ichinose [15] and Gaveau [16] provide theorems establishing the equivalence between the determinant of the Dirac operator and path integrals over spinor-valued paths with appropriate boundary conditions on finite domains. These constructions carefully incorporate the spinor connection and holonomies of spin rotations along geodesic segments, ensuring the correct treatment of spinor phases and curvature effects.

Our representation of the determinant as a sum over oriented closed loops weighted by factors of

the form $\prod \exp(-m dl + \frac{i\sigma_3 \delta\theta}{2})$, where dl is an infinitesimal geodesic step and $\delta\theta$ the corresponding trajectory rotation angle, follows directly from these rigorous path integral formulations. This approach generalizes the combinatorial and topological methods pioneered by Vdovichenko [17] in the exact solution of the 2D Ising model, where the fermionic nature and spinor holonomies enforce cancelations of non-planar intersections, leaving only planar loop configurations that contribute to the determinant.

Furthermore, the Gauss-Bonnet theorem relates the total tangent rotation angle around a loop to its self-intersection number, providing a topological invariant that governs the sign factors in the loop expansion. This ensures that the fermionic statistics and boundary conditions are correctly encoded in the loop amplitudes.

Thus, the path integral representation employed here is not only physically intuitive but also mathematically sound, grounded in well-established results in spin geometry, spectral theory of Dirac operators, and rigorous path integral constructions on manifolds with boundary. This justifies its use as the foundation for deriving loop equations and analyzing the planar topology of the fermion determinants in the Elfin theory.

6.2. Random loops at the surface

The form of the surface S is fixed as a Hodge-dual minimal surface in a conformal metric. Let us perform the functional integration over the Elfin fields ψ . We use the gauge $\rho = 0$, where the induced metric is simply $e = |f'|^2$, the internal curvature R_{ab} and spinor connection ω_k are absent, making the theory locally equivalent to a spinor on a flat surface.

This produces two determinants of the Dirac operators with the boundary conditions $\lambda\sigma_3 = \pm 1$:

$$I[S] = \int \mathcal{D}\psi e^{A_0} = \Delta_+ \Delta_-; \quad (6.1)$$

$$\Delta_{\pm} = \det(D + m\sqrt{e})_{\pm} \quad (6.2)$$

On an infinite flat surface, such a determinant would be calculable using the trace of the logarithm of a resolvent in Fourier representation. On a finite surface S bounded by an arbitrary curve C , there are nontrivial boundary conditions for a Dirac resolvent, complicating the analytic computation.

Instead, we can represent the Dirac determinant as a sum over vacuum loops at the surface. The similar representation in the context of the 2D Ising model was discussed in my earlier work [18], inspired by studies of the Ising model by Vdovichenko [17]. That pioneering paper laid a framework for a topological solution of the Ising model in terms of self-avoiding paths. The next step of our paper [18] was to generalize this method to a continuum

Dirac operator on a Riemann surface using the Gauss-Bonnet theorem to relate the rotation angle to the intersection index. There are also some theorems in the mathematical literature [15, 16] establishing the Dirac and Heat kernel path integral representations in a finite domain. In this paper, we follow the technology described in [8], with proper adjustments from a random surface to a Hodge-dual minimal surface.

We base our study on the superposition principle. The vacuum amplitude for the Dirac particle represents the sum over all configurations of the loop $\Gamma \in S$ of the corresponding amplitude for the given loop. The amplitude of the given loop represents the product of the amplitudes of individual events. The individual events can be regarded as a sequence of classical propagations along little geodesic steps alternating with instant rotations.

Technically, we use the logarithm of a Dirac determinant and represent it as a trace of a resolvent integrated over proper time

$$\Delta_{\pm} = \exp\left(\kappa |S[C]| - \int_{\epsilon}^{\infty} \frac{dT}{T} \exp(-T(D + m\sqrt{e}))\right); \quad (6.3)$$

$$\kappa \propto \log \epsilon; \quad (6.4)$$

The logarithmically divergent term $\log \epsilon$ in the exponential is proportional to the area of the surface by virtue of the locality of this divergent contribution to the trace. The terms in the exponential, proportional to the area of the additive Hodge-dual surface, pass through the loop equation, as we already established. The role of these terms is to regularize the effective string tension (or vacuum energy density) of the Fermi model on the surface.

The path integral representation emerges when this exponential is replaced by a limit of a product (see [19])

$$\exp(-T(D + m\sqrt{e})) \rightarrow \prod \exp(-dT(D + m\sqrt{e})); \quad (6.5)$$

$$dT = dl/\sqrt{e} \quad (6.6)$$

The mathematical literature replaces this product with a stochastic process that is equivalent to Feynman's sum over paths, with the path amplitude being a product of WKB amplitudes for these propagations/rotations [16].

The amplitude for the rotation is given by the rotation matrix

$$A(\Delta\theta) = \exp(i\sigma_3 \Delta\theta/2). \quad (6.7)$$

The WKB amplitude for the geodesic step reads

$$A(step) = \exp(-mdl) \quad (6.8)$$

6.3. The Gauss-Bonnet theorem and self-intersections

The total product of the factors (3.5) and (3.6) along the loop can be calculated by means of the Gauss-Bonnet formula which in our notation reads

$$\sum \Delta\theta = 2\pi(1 - \nu) \pmod{2\pi}. \quad (6.9)$$

Here ν is the algebraic number of self-intersections of the loop Γ at the surface. The Gauss-Bonnet theorem ensures that the relation is topologically invariant.

Remark 6.1. Mathematical theorems. For an oriented regular simple closed curve $\gamma \subset \mathbb{R}^2$, the rotation (turning) index satisfies $\text{rot}(\gamma) = \frac{1}{2\pi} \int_{\gamma} \kappa ds \in \mathbb{Z}$ and equals +1 for the positively oriented boundary of a disk [20]. In the planar case, this is exactly the Gauss-Bonnet theorem for the enclosed region (since $K \equiv 0$), yielding $\int_{\gamma} \kappa ds = 2\pi \chi = 2\pi$ (hence equality modulo 2π is automatic) [21]. Moreover, since $\text{rot}(\gamma)$ is the degree of the unit-tangent map $T : S^1 \rightarrow S^1$, it depends only on the immersed curve itself and therefore is unchanged if the ambient plane is replaced by a disk with finitely many holes (and the same mod-2 intersection sign $(-1)^\nu$ follows from Whitney's regular-homotopy classification of immersed plane curves) [20].

The amplitude for the loop reads:

$$A[\Gamma] = (-1)^\nu \exp(-ml_\Gamma); \quad l_\Gamma = \int_{\Gamma} \sqrt{e}|dz| \quad (6.10)$$

The extra negative sign comes from Fermi statistics. This amplitude is a scalar, independent of the quantum numbers, so we should multiply it by the number of allowed states. Each two-component Dirac particle has only one allowed state which is projected by the operator

$$P = \frac{1}{2}(1 + \sigma_a v_a) \quad (6.11)$$

where v_a is the normalized 2-velocity of the rest frame. In the rest frame, there should be only one component (in 4 dimensions, there were two components).

So we are left with the factor of 2 from the sum over the orientations $\sigma_3 = \pm 1$. Yet it will be convenient to distinguish the terms with two orientations, i.e. to sum over oriented loops Γ . We mark the loop by an (anti)clockwise arrow for (left) right orientation $\sigma_3 = -1, +1$.

The point is that the loops that touch the external boundary at least once are oriented in the right direction according to our boundary conditions.

The reflection amplitude

$$R = \frac{1}{2}(1 + \lambda\sigma_3) \quad (6.12)$$

corresponds to the repulsion of the left-hand side components from the wall (see the previous section). As discussed above, one may occupy the wall with the left-hand side states so that this repulsion would come about automatically due to the Pauli principle.

So, the sum over loops involves the sum over orientations only for the inner loops.

6.4. From exponential of free elfin loops to sum over multiple crossing paths

Consider a given oriented loop consisting of N equal geodesic steps dl . The degrees of freedom are given by the angles $\Delta\theta$ and by the number N of steps. The phase volume can be written in a covariant form

$$\mathcal{D}\Gamma = N^{-1} \prod d(\Delta\theta) = dl Dx(l) \delta(x^2 - 1) e^{-m_0 l} \quad (6.13)$$

The δ -functions remove the integrations over the lengths $|dx_i|$ of the geodesic steps, leaving us with the normalized 2-velocities as physical variables. The mass renormalization term m_0 is a matter of convention.

The factor $N^{-1} = 1/l$ in (6.13) accounts for N equivalent choices for the origin of the parametrization of the loop. These factors will cancel the combinatorial factors that arise at the intersections (see below).

We write the integral over loops with the above prescription at the reflections as follows:

$$\begin{aligned} \Delta &= \Delta_+ \Delta_- \\ &\propto \exp\left(\sum \int \mathcal{D}\Gamma (-1)^\nu \exp(-ml_\Gamma)\right). \end{aligned} \quad (6.14)$$

We ignore the (singular) normalization factor in the fermionic determinant. This factor on a finite surface amounts to an exponential of the area $\exp(-\text{const} |S|)$, which we include in the confining factor that is already present in our solution for the Wilson loop, according to the previous section.

The \int denotes the lack of a sum over orientation for the loop touching the boundary due to our boundary conditions. Note that both determinants contain loops that touch the boundary. These loops enter with a weight of $1/2$ in each determinant Δ_{\pm} , or, equivalently, they count as oriented loops, unlike the remaining loops, which involve a sum of two orientations.

In what follows, it will be convenient to consider the product Δ rather than the separate factors Δ_{\pm} .

Let us expand (6.14) in a series of multiple integrals over loops:

$$\begin{aligned} \Delta &= \sum \frac{1}{n!} \\ &\int \mathcal{D}\Gamma_1 \dots \int \mathcal{D}\Gamma_n (-1)^{\sum \nu_i} \exp\left(-m \sum l_i\right). \end{aligned} \quad (6.15)$$

These loops are independent by construction, but we are going to rearrange the sum in such a way that they will start to repel. This miraculous transformation, first conjectured in [18] is possible due to the following topological and combinatorial observations.

6.5. Cancellation of intersections: step towards planar graphs

This section reproduces (with some simplifications and improvements) the most important results of our ‘81 paper: the topological and geometrical analysis of the path integrals of the Dirac particle on a disk-like surface.

The arguments of this section were inspired by a geometric solution of the 2D Ising model by Natasha Vdovichenko [17]. The crucial observation made in that pioneering work was that the sum of planar loops splitting the plane into domains of up and down spin in the Ising model is equivalent to the sum over freely intersecting independent loops, with phase factors reflecting the rotation of a spin 1/2 particle. The signs arising for intersecting paths lead to cancelation between such paths, leaving only planar loops. The computation in that paper relied on the geometry of the paths on a square lattice and other specifics of the Ising model. Below, the same topological observations will be stripped of the lattice artifacts and applied to a two-fermion system with oriented loops on a Hodge-dual minimal surface.

Consider the given configuration of loops at the surface as a graph consisting of several disconnected parts. Connected subgraphs contain intersecting and touching lines. The total length in exponential factors $\exp(-ml)$ can be redistributed among the lines of the graph:

$$l_{tot} = \sum l_{loops} = \sum l_{lines}. \quad (6.16)$$

This statement is not as trivial as it seems. The length of the line is not just a geometric length of this line drawn on a planar disk; rather, it is an integral

$$l_{line} = \int |dz(t)| \sqrt{e(z(t), \bar{z}(t))} \quad (6.17)$$

However, the metric $e(z, \bar{z})$ in this integral being *local*, this length is additive across the pieces made by intersections of these lines on a planar domain. The factorization also applies the sign factor since the number of mutual intersections is always even in the absence of handles at the surface.

$$\nu_{tot} = \sum \nu_{loops} = \sum \nu_{graph} \pmod{2}. \quad (6.18)$$

The phase volume of the connected subgraph G can also be rearranged in such a way that the old

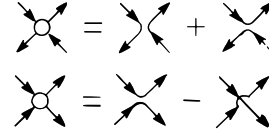


Figure 3: Types of line collision: two planar (upper drawing) and one planar, another non-planar (lower drawing)

loops lose their individuality:

$$DG = \prod_{line} dW(step), \quad (6.19)$$

$$dW(step) = dlDx(l)\delta(x^2 - 1). \quad (6.20)$$

The factors $1/l$ in front of the old loops are compensated by the same factors that arise from the sums over the numbers of geodesic steps between the intersections of lines.

It is important that there are no other factors in front of the loop. Were there, say, k internal degrees of freedom, the corresponding factor

$$\prod_{loops} k \quad (6.21)$$

could not possibly be distributed among the lines of the graph. In the case of $k = 1$ one could return to the non-oriented lines, then the phase volume would be distributed again. This is the case of the Ising model, which was considered in the preliminary version [18] of the Elfin theory. This possibility is ruled out by the boundary conditions. As we shall see soon, the peculiar boundary conditions play a central role in the construction of the loop equations.

Let us proceed with the sum over graphs. Each internal line of our graph can be oriented in both directions, but orientation is conserved in the vertices. We neglect multiple collisions as a violation of the Pauli Principle (Grassmann algebra $(\bar{\psi}^R \psi^R)^n = 0, (\bar{\psi}^L \psi^L)^n = 0$ for $n > 1$, so we deal with the two pairs of vertices depicted at Fig. 3: Naturally, one could treat these two vertices as a single vertex depending on the angles between the lines; however, in this case, there will be step functions of the angles. When the lines cross each other in coordinate space, the term in the vertex changes sign.

The non-planar vertex (the second one on the lower drawing in Fig. 3) cancels the first one, so this configuration of lines drops from the sum. This is the heart of the matter. The lines may touch each other with opposite orientations according to Fig. 3, but the terms with intersecting lines are always canceled by those with parallel touching lines in the graph with the same configuration of lines.

Note that in the general case, this is a cancelation of terms with a different number of loops, so there

is no room for extra degrees of freedom. This is the Pauli principle reformulated in terms of the path integrals.

We may now return to our old loops but disregard all the non-planar configurations. We obtain a hierarchy of trapped loops that move in the free space left by the others. With one-component fermions, we would obtain the sum over all decompositions of the whole surface into two different phases, which is equivalent to an Ising model.

The above representation of the Majorana determinant would amount to the Onsager solution of the Ising model in terms of free Majorana fermions. In our case, we have twice the number of components, providing for the oriented planar loops instead of just boundaries of the spin domains.

The time slice ($\xi_2 = \text{const}$) of this picture describes a string with particles moving between neighbors. Pairs of ψ and $\bar{\psi}$ particles can be created or annihilated. Only $\psi\bar{\psi}$ neighbors can touch each other. The touching of $\psi\psi$ or $\bar{\psi}\bar{\psi}$ neighbors is forbidden by the Pauli principle. One $\psi, \bar{\psi}$ pair is placed at the two ends of the string.²

This resembles the 't Hooft string model for planar graphs [22]. Our string has the same topology but takes into account the gauge invariance of the planar graph expansion. This will be demonstrated in the next sections.

6.6. Loop equation for fermion determinants

Let us now find the variation of Δ with respect to the boundary value of e .

The basic relation reads

$$\frac{\delta e^{-m\Gamma}}{\delta e(x_0)} = -m \int_{\Gamma} \frac{dl}{2e} \delta^2(\xi - \xi_0) e^{-m\Gamma},$$

$$dl = |d\xi| \sqrt{e} \quad (6.22)$$

The invariant δ -function

$$e^{-1} \delta^2(\xi - \xi_0) = \delta_{inv}(x, x_0), \quad x, x_0 \in S, \quad (6.23)$$

removes one of the d^2x_{\parallel} integrations in the sum over loops. The additional dl integration that arises is required by our rules since a new line at the graph is created.

The variation selects the graph that touches the boundary at x_0 . The touching line is oriented to the right according to our boundary conditions.

The amplitude of touching equals $-m$; the remaining factors contribute to the phase volume of the graph.

²This interpretation of the time slice dynamics can be used for a rigorous proof of the equivalence of the free Dirac vacuum loops and the planar loops made of non-intersecting closed paths on a surface. Such a proof would use the Hamiltonian representation of a Fermionic system with conventional creation/annihilation operators and chiral boundary conditions.

Let us follow the loop that touches the boundary. This is the correct loop; therefore, each loop that touches it from the outside is also correct. We observe that the outside domain S_{out} between this loop Γ and the external boundary C is completely equivalent to the original surface S . The loops trapped in this domain reflect from Γ in the same way as they do from the external boundary (this is why we need the special boundary conditions).

The sum over configurations and orientations of the loops in S_{out} produces precisely the same Dirac determinant.

$$\Delta_{out} = \Delta_{+}^{out} \Delta_{-}^{out} \quad (6.24)$$

The loops that are trapped inside Γ reflect from inside, so they are oriented to the left at the boundary Γ^{-1} . The sum over configurations and orientations of these loops produces the Dirac determinant for the internal domain,

$$\Delta_{in} = \Delta_{+}^{in} \Delta_{-}^{in}, \quad (6.25)$$

with the opposite boundary conditions,

$$\psi^R = \bar{\psi}^R = 0, \quad \text{at } \Gamma^{-1}. \quad (6.26)$$

The numerical value of this determinant is the same as that for the old boundary conditions.

We see, however, that the orientation $\lambda\sigma_3$ is related to the orientation of the boundary in space. This will be important in higher order $1/N$ expansion of QCD where the multiloop propagators depend upon the relative orientation of loops.

Note that the loop Γ may touch itself as well as the external loop C (at the surface). In this case, one or both of the domains S_{in}, S_{out} reduce to a set of windows touching at the corners. The corresponding functional should be understood as

$$\Delta = \prod \Delta(\text{windows}). \quad (6.27)$$

This is clear from the original representation of Δ as an exponential of the sum over configurations of independent loops. This planar hierarchical set of loops is shown in Fig. 4.

7. The Minimal Surface and the Loop Equation

In the 1981 theory, the next step was to integrate over all embeddings $X_{\mu}(\xi)$. This led to the Liouville instability. In the present theory, we replace this integration with the *Rigid Hodge-Dual Surface* $S_{min}[C]$ defined in [1] and described in the section 3 of this paper.

This surface is the unique additive solution to the minimal area problem with the constraint that the area derivative is self-dual. It is fixed by the boundary loop C . Therefore, we do not integrate over embeddings. The functional $Z[C]$ is simply the fermion determinant on this specific manifold:

$$Z[C] \equiv Z[S_{\chi}[C]]. \quad (7.1)$$

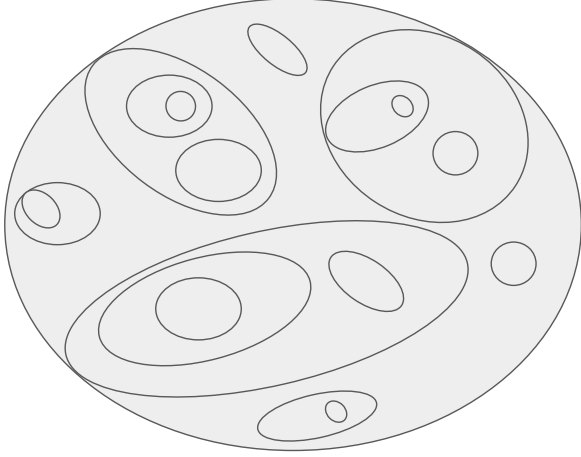


Figure 4: The hierarchical set of loops, some touching, but never intersecting each other nor self-intersecting

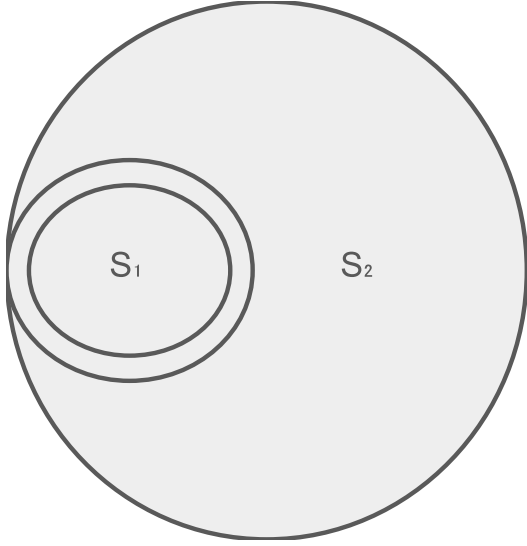


Figure 5: The first area derivative of Dirac determinant. There is one internal path Γ which cut the surface S into two pieces $S_{in} = S_1, S_{out} = S_2$

For the time being, we fix the Hodge duality χ of this surface; later, we will discuss the restoration of parity symmetry in the loop equation.

7.1. Loop equations

We now demonstrate that this $Z[C]$ satisfies the loop equation of the same structure as (2.10).

Using the above planar loop equations for Dirac determinants and area derivatives of the HD minimal surface, we may write the following loop equation for the functional $Z[S]$:

$$\delta Z[S]/\delta\sigma_{\mu\nu}(x_1) = -m \int \mathcal{D}\Gamma_{11} \delta_{I,0} T_{\mu\nu}(1) Z[S_{in}] Z[S_{out}] e^{-m l_{11}}. \quad (7.2)$$

This equation is illustrated in Fig. 5 Here, the tensor T was defined in (10.8). The loop Γ_{11} touches

C_{11} at x_1 . The integer index factor

$$I = \int_{\Gamma} dl_1 \int_{\Gamma} dl_2 \theta(l_1 - l_2) e_{ab} \dot{\xi}_a(l_1) \dot{\xi}_b(l_2) \delta^2(\xi(l_1) - \xi(l_2)) \quad (7.3)$$

is the absolute number of self-intersections of the loop Γ_{11} at the surface. The Kronecker delta $\delta_{I,0}$ in the integral in (7.2) enforces the self-avoiding loop Γ_{11} . In the following, we denote path integrals over self-avoiding loops as $\int_{\simeq} \mathcal{D}\Gamma$

The measure of the open path is defined as follows:

$$\int \mathcal{D}\Gamma_{11} = \int dl \int_{x(0)=x_1}^{x(l)=x_1} Dx(l) \delta(\dot{x}^2 - 1). \quad (7.4)$$

Eq. (7.2) was postulated in the first version of the Fermi String theory [18] from heuristic arguments. At that time, it seemed that the equation applied to the Ising model at the surface, i.e., for the 2-component spinors. However, as we see now, one should introduce two spinors with special boundary conditions in order to obtain this equation for the propagator of the Fermi string.

Note that our theory is constructed in such a way that it is equivalent to the flat theory with a variable fermion mass. In the next section, we shall use the second area derivative of $Z[C]$, which reads

$$\frac{\delta^2 Z}{\delta\sigma_{\mu\nu}(l) \delta\sigma_{\alpha\beta}(r)} = A_{\mu\nu\alpha\beta} + B_{\mu\nu\alpha\beta}; \quad (7.5)$$

$$A_{\mu\nu\alpha\beta} = (m/2)^2 T_{\mu\nu}(l) T_{\alpha\beta}(r) \int \int_{\simeq} \mathcal{D}\Gamma_l \mathcal{D}\Gamma_r Z[S_l] Z[S_{mid}] Z[S_r] \exp(-m(l_l + l_r)); \quad (7.6)$$

$$B_{\mu\nu\alpha\beta} = (m/2)^2 T_{\mu\nu}(l) T_{\alpha\beta}(r) \int \int_{\simeq} \mathcal{D}\Gamma_{up} \mathcal{D}\Gamma_{dn} \times Z[S_{up}] Z[S_{mid}] Z[S_{dn}] \exp(-m(l_{up} + l_{dn})). \quad (7.7)$$

This equation is illustrated in Fig. 6,7. The first term arose due to the variation of the last factor in (7.2). The second term arose due to the variation of the factor $\exp(-ml)$ as has been discussed above. In this case, there are two paths Γ_{up}, Γ_{dn} which cut the surface S into three pieces $S_{up}, S_{mid}, S_{down}$ with the boundaries

$$\partial S_{up} = \Gamma_{up} C_{rl}, \quad (7.8)$$

$$\partial S_{mid} = \Gamma_{dn}^{-1} \Gamma_{up}^{-1}, \quad (7.9)$$

$$\partial S_{dn} = \Gamma_{dn} C_{lr}. \quad (7.10)$$

The variation of the factor $Z[S_{in}]$ in (7.2) would require one of the internal loops inside S_{in} to touch the external boundary C . This implies that Γ touches C at the same point, so this is the triple collision that we rule out as a violation of the Pauli Principle (and Grassmann algebra) $(\bar{\psi}^R \psi^R)^3 = (\bar{\psi}^L \psi^L)^3 = 0$. As for the remaining factors in (7.2) they do not depend upon e .

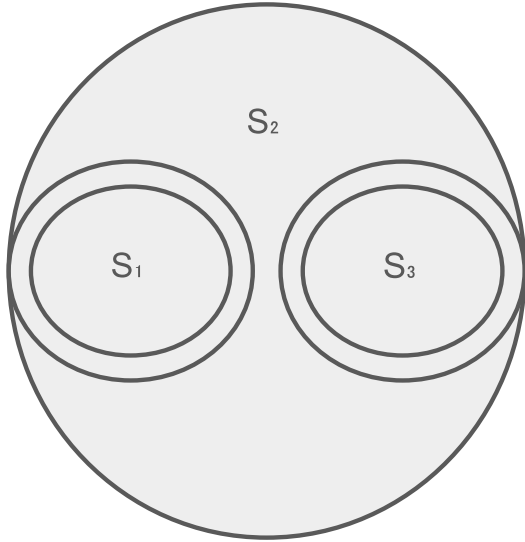


Figure 6: The first term in the second area derivative of Dirac determinant. There are two closed loops Γ_l, Γ_r which cut the surface S into three pieces $S_1 = S_l, S_2 = S_{mid}, S_3 = S_r$.

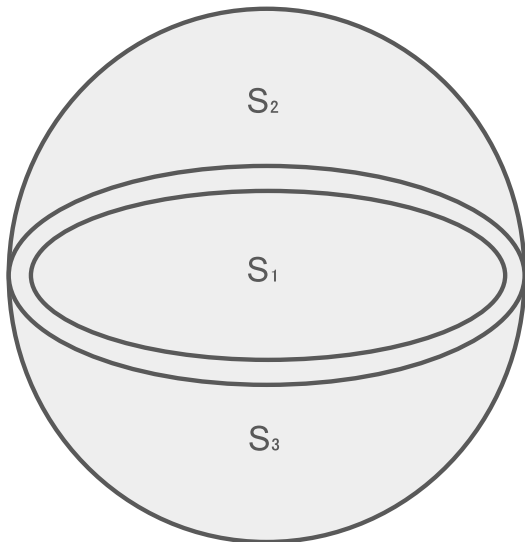


Figure 7: The second term in the second area derivative of Dirac determinant. There is one closed loop $\Gamma = \Gamma_{up}\Gamma_{dn}$, touching the loop C at the left and the right points and cutting the surface S into three pieces $S_1 = S_{mid}, S_2 = S_{up}, S_3 = S_{dn}$.

The operator \mathcal{L}_ν involves the gradient of the first area derivative. Using the translation invariance identity [5]

$$\partial_\mu F[C_{xx}] = - \int_{C_{xx}} dy_\alpha \frac{\delta F[C_{xx}]}{\delta \sigma_{\alpha\mu}(y)} \quad (7.11)$$

we can rewrite $\mathcal{L}_\nu(Z[C])$ as a similar double integral with the second area derivative

$$\mathcal{L}_\nu(l)Z[C] = - \int_{C_{ll}} dx_r^\alpha \frac{\delta^2 Z[C]}{\delta \sigma_{\mu\nu}(l) \delta \sigma_{\alpha\mu}(r)} \quad (7.12)$$

Substituting the loop equation (7.5) for $Z[C]$ here, we find two terms corresponding to the two drawings in Fig. 6 and 7.

7.2. Large fermion mass and induced QCD

We assume that the fermion mass m is much larger than the physical scale Λ_{QCD} , along the lines of the induced QCD scenario [23]. As we shall see, in this limit, the mass of the fermion m serves as a UV cutoff, and the A -term reduces to the same loop operator applied to the area of the Hodge-dual minimal surface. This term vanishes by the Bianchi identity, as we have established in our previous work and summarized in the beginning of this paper. The second term reduces, in this limit, to the right side of the MM equation multiplied by a coefficient determined by the local properties of the Dirac determinant on a flat minimal surface in the vicinity of the self-intersection of the loop.

These conclusions will be based on a well-known property of geodesic paths on Riemann surfaces, which we formulate as a Lemma.

Lemma 7.1 (Geodesic Inequality). *For any minimal surface embedded in Euclidean space, the geodesic distance $L_{geo}(x, y)$ is strictly bounded by the Euclidean distance:*

$$L_{geo}(x, y) \geq |x - y|_{\mathbb{R}^4}. \quad (7.13)$$

Proof. The geodesic distance between two points x, y along the surface embedded in Euclidean space is a constrained minimum of the length of paths connecting these points in Euclidean space. The constraint is that every point of this path belongs to the surface. The set of such paths is a subset of all Euclidean paths, and the line element $dl = |d\xi| \sqrt{e}$ in the induced metric $e = |f'|^2$ coincides with the Euclidean line element $ds = \sqrt{|df|^2}$; therefore, the minimal length of the subset path is greater or equal to the target space distance $\int ds = |x - y|_{\mathbb{R}^4}$. \square

Remark 7.1. *Note that we used the induced metric $e = |f'|^2$, the same as for the Euclidean minimal surface (Goldschmidt solution to the Plateau problem), rather than the full induced metric on a general surface in $\mathbb{R}^3 \otimes \mathbb{R}^4$. The metrics coincide on a holomorphic minimizer, but for the area derivatives, we need the full external geometry in the 12*

dimensional space $\mathbb{R}^3 \otimes \mathbb{R}^4$. Once the area derivatives are taken (as they are in our loop equations, resulting in Hodge-dual tensors $T_{\mu\nu}$) we could use a holomorphic minimizer for the induced metric in path integrals.

We are going to use this theorem for the terms arising in the loop equation for the Dirac determinants.

7.3. The A -term

The first term (see Fig. 6) in the limit of large fermion mass (much larger than the external curvature $Q_{ab} = \text{diag}\{-\rho, \rho\}$ of the minimal surface at its boundary C) effectively involves infinitesimal flat loops Γ_l, Γ_r . The factor $Z[S_{mid}]$ reduces to the constant $Z[S[C]]$, which we take out of the path integrals $\int_{\approx} \mathcal{D}\Gamma_l \mathcal{D}\Gamma_r$. These integrals can be computed on an infinite flat semiplane, and they reduce to constants independent of the points x_l, x_r . We find

$$A_{\mu\nu\alpha\beta} \rightarrow T_{\mu\nu}(l)T_{\alpha\beta}(r)Z[C]a^2; \quad (7.14)$$

$$a = m/2 \int_{\approx} \mathcal{D}\Gamma Z[\Gamma] \exp(-m\Gamma); \quad (7.15)$$

Now, we recall that the area derivative of the minimal surface is also proportional to the tangent tensor $T_{\mu\nu}$, and let us factor out of $Z[C]$ the vacuum energy factor (with $S[C]$ being the Hodge-dual minimal area)

$$Z[C] = G[C]Z_1[C]; \quad (7.16)$$

$$G[C] = \exp(-\kappa S[C]) \quad (7.17)$$

We can rewrite the factor TT as a second area derivative

$$A_{\mu\nu\alpha\beta} \rightarrow \frac{-a^2 Z_1[C]}{4\kappa^2} \frac{\delta^2 G[C]}{\delta\sigma_{\mu\nu}(l)\delta\sigma_{\alpha\beta}(r)}; \quad (7.18)$$

which is valid for arbitrary κ and $x(l) \neq x(r)$. Now, we use the translational identity (7.11) backwards

$$\begin{aligned} & \int_{C_{ll}} dx_r^\alpha A_{\mu\nu\alpha\mu} = \\ & \frac{-a^2 Z_1[C]}{4\kappa^2} \int_{C_{ll}} dx_r^\alpha \frac{\delta^2 G[C]}{\delta\sigma_{\mu\nu}(l)\delta\sigma_{\alpha\mu}(r)} = \\ & \frac{a^2 Z_1[C]}{4\kappa^2} \partial_\mu \frac{\delta G[C]}{\delta\sigma_{\mu\nu}(l)} \end{aligned} \quad (7.19)$$

The last integral, as we already established, vanishes for the Hodge dual minimal surface by the Bianchi identity. Thus, the (unwanted) A -term in the loop equation vanishes in the local limit.

7.4. The B -term

The B -term in the Dirac determinant loop equation has a completely different structure, and it is singular in the local limit.

$$\begin{aligned} B_{\mu\nu\alpha\beta} &= (m/2)^2 T_{\mu\nu}(l)T_{\alpha\beta}(r) \iint_{\approx} \mathcal{D}\Gamma_{up} \mathcal{D}\Gamma_{dn} \\ &\times Z[S_{up}]Z[S_{mid}]Z[S_{dn}] \exp(-m(l_{up} + l_{dn})). \end{aligned} \quad (7.20)$$

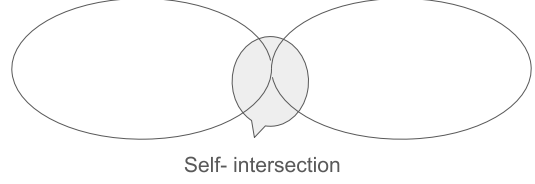


Figure 8: Self-intersecting loop.

The B -term in the loop equation

$$\int_{C_{ll}} dx_r^\alpha B_{\mu\nu\alpha\mu} \quad (7.21)$$

involves the matrix product of two T tensors

$$TT_{\alpha\nu} = T_{\alpha\mu}(r)T_{\mu\nu}(l) \quad (7.22)$$

which can be reduced further using the algebra of the η tensors (valid for both Hodge-chiralities $\chi = \pm 1$)

$$\eta_{\alpha\mu}^{i,\chi} \eta_{\mu\nu}^{j,\chi} = -\delta_{ij} \delta_{\alpha\nu} - e_{ijk} \eta_{\alpha\nu}^{k,\chi} \quad (7.23)$$

Both tensors T , being Hodge-dual, can be represented as

$$T_{\mu\nu}(x) = \frac{1}{2} \vec{\tau}(x) \cdot \vec{\eta}_{\mu\nu}^\chi \quad (7.24)$$

with some unit vector $\vec{\tau}(x)^2 = 1$, depending on the point $x \in C$. This tangent tensor was defined as a limit of the normalized area element $\Sigma_{\mu\nu}$ on the surface when a point $x \in S[C]$ approaches the boundary C .

Afterward, the matrix product becomes

$$TT_{\alpha\nu} = \frac{-1}{4} ((\vec{\tau}(r) \cdot \vec{\tau}(l)) \delta_{\alpha\nu} + (\vec{\tau}(r) \times \vec{\tau}(l)) \cdot \vec{\eta}_{\alpha\nu}^\chi) \quad (7.25)$$

Now, we explore the consequences of the geodesic inequality. In the local limit, the points l, r belong to the self-intersection of the loop C . The Goldschmidt minimal surface (additive in the limit when $C = C_{lr} \cdot C_{rl}$) breaks into two surfaces covering closed loops connected at the self-intersection point, as shown in Fig 8. The zoom into the vicinity of the self-intersection is shown in three dimensions in Fig. 9. The minimal surface is, in general, curved, though the arithmetic mean curvature vanishes everywhere. In the vicinity of the self-intersection, for our Goldschmidt solution, there is an infinitesimal narrow bridge connecting two parts bounded by loops C_{lr}, C_{rl} . This is proven in White's bridge theorem [24]. This property places the tensors $T(l), T(r)$ in the infinitesimal vicinity of each other on this bridge. In the local limit, we have $\vec{\tau}(l) \rightarrow \vec{\tau}(r)$, so that the matrix product

$$T_{\alpha\mu}(r)T_{\mu\nu}(l) \rightarrow \frac{-1}{4} \delta_{\alpha\nu} \quad (7.26)$$

As for the rest of the factors, the sum over the short paths Γ_{up}, Γ_{dn} is dominated by the geodesic distance, which is bounded by the Euclidean distance. This precise alignment relies on the isotropic scaling

White's Bridge / Self-Intersection Vicinity

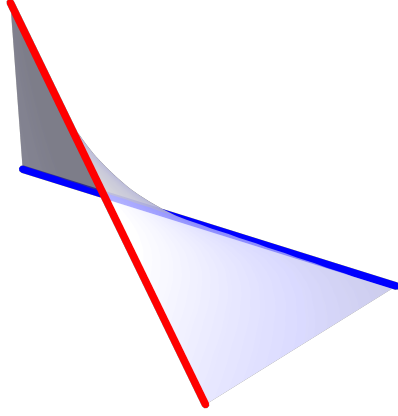


Figure 9: The additive minimal surface in the vicinity of the self-intersection. There is a narrow twisted strip (White's bridge) connecting the minimal surfaces bounded by two parts of the self-intersecting loop.

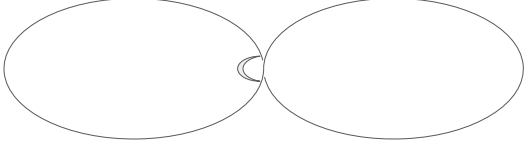


Figure 10: Two arcs Γ_l, Γ_r connecting self-intersection points, bounding the crescent-shaped area S_{mid} .

of White's bridge in the varifold limit $\epsilon \rightarrow 0$. In the strict limit of the topology change, the continuity of the area Hessian demands that the tangent planes perfectly align, yielding the required Fierz-like identity for the MM loop equation without generating anomalous contact terms. A rigorous geometric measure-theory proof of the Hessian's continuity across this topology change is left for future mathematical study, but is physically mandated by the $O(4)$ symmetry of the local loop diffusion. We find:

$$B_{\mu\nu\alpha\mu} \rightarrow -b\delta_{\alpha\nu}Z[C_{lr}]Z[C_{rl}]\delta^4(C(l) - C(r)); \quad (7.27)$$

$$b\delta_m^4(C(l) - C(r)) =$$

$$\frac{m^2}{16} \iint_{\asymp} \mathcal{D}\Gamma_l \mathcal{D}\Gamma_r Z[S_{mid}] \exp(-m(l_l + l_r)). \quad (7.28)$$

This path integral over small surface paths Γ_l, Γ_r is illustrated in fig.10, where these paths are two arcs bounding the crescent-shaped S_{mid} . We use an approximation of the delta-function

$$\delta_m^4(x - y) = 4m^4 \exp(-2m|x - y|) \quad (7.29)$$

Putting the pieces together, we find the loop equation (2.10) with

$$W[C] = \frac{Z[C]}{Z[\mathbb{1}]}; \quad (7.30)$$

$$\lambda\delta_m^4(C(l) - C(r)) = \frac{m^2 Z[\mathbb{1}]^2}{16}$$

$$\iint_{\asymp} \mathcal{D}\Gamma_{up} \mathcal{D}\Gamma_{dn} \exp(-m(l_{up} + l_{dn})) W[C_{up} \cdot C_{dn}]. \quad (7.31)$$

The chirality of the Hodge dual minimal surface dropped from this equation, as it dropped from the whole internal geometry, including the minimal area and the Dirac determinant. Therefore, there is no necessity to symmetrize our solution over Hodge chirality to restore the parity of QCD: the parity is preserved by the Dirac determinant on a Hodge-dual minimal surface.

The sign is positive, as it should be for QCD with a positive 't Hooft coupling constant λ . As for the value of this coupling constant, it is determined by normalization $Z[\mathbb{1}]$. The string tension normalization factor $G[C] = \exp(-\kappa S[C])$ cancels on both sides of the loop equation, so it does not influence λ , but the normalization factor $Z[\mathbb{1}]$ at vanishing loop multiplies this constant twice.

The asymptotically free QCD we are looking for corresponds to the limit when this factor goes to zero. In that limit, the standard RG computations based on planar graphs would produce the QCD mass scale

$$\Lambda_{QCD} = m\lambda^{-\frac{51}{121}} \exp\left(-\frac{24\pi^2}{11\lambda}\right); \quad (7.32)$$

Therefore, all we need is the limit of the Elfin theory such that this factor vanishes

$$\lambda \propto Z[\mathbb{1}]^2 \rightarrow 0; \quad (7.33)$$

The rest of perturbative QCD will follow from the loop equation by iterations in λ starting with $W[\mathbb{1}] = 1$. Let us now outline this perturbative QCD derivation.

8. Asymptotically free planar QCD from the loop equation

The Elfin theory induces QCD in the limit of large fermion mass, serving as a short-distance cut-off. There are no singularities at finite mass, which eliminates the messy discussion about cusp and perimeter singularities of the Wilson loop. The Wilson loop is defined in the Elfin theory as a regularized solution of the loop equation, with the delta function smeared by a finite fermion mass. This definition of the loop equation makes mathematical sense, in our opinion: regularize this equation by smearing the delta function on the right side while preserving the gauge invariance by keeping all loops closed. The Elfin theory falls into the category of regularized solutions of the loop equation.

As it satisfies the MM equation together with the initial condition $Z[\mathbb{1}] = const$, it reproduces all the planar graphs of asymptotically free QCD. All we know about cusp singularities, perimeter corrections, and the dimensional transmutation of

the QCD mass scale comes from that perturbation expansion. Furthermore, the Elfin theory offers a globally regularized definition of planar QCD as a system of free fermions living on a minimal surface: a well defined and solvable two-dimensional model.

This model will be discussed in detail in the next section; in the rest of this section, we shall derive the planar graph from the loop equation in the context of Elfin theory.

8.1. Bootstrap equation and planar graphs with glassed windows

The planar graphs in Feynman gauge, including the ghost loops, were reproduced from the loop equation in the original MM paper [7] using the so-called Bootstrap equation (section 6 in that paper). This equation was based on the inversion of the point derivative operator ∂_μ in the equations of motion, using the Bianchi identity. The area derivative was split into linear B_α and quadratic $B_{\mu\nu}$ terms

$$\frac{\delta W[C]}{\delta \sigma_{\mu\nu}(x)} = (\partial_\nu^x \delta_{\mu\alpha} - \partial_\mu^x \delta_{\nu\alpha}) B_\alpha[C_{xx}] + B_{\mu\nu}[C_{xx}]; \quad (8.1)$$

The linear terms were related to the quadratic terms and the source term $J_\nu[C_{xx}]$ on the right side of the MM equation

$$B_\nu = (-\partial^2 \delta + [\partial, \partial])^{-1} (J_\lambda - \partial_\mu B_{\mu\lambda}); \quad (8.2)$$

$$J_\nu[C_{xx}] = \lambda \int dy_\nu \delta^4(x-y) W[C_{xy}] W[C_{yx}] \quad (8.3)$$

The next step was to expand the inversion operator in powers of the commutator

$$\begin{aligned} (-\partial^2 \mathbb{1} + [\partial, \partial])^{-1} &= -\partial^{-2} \mathbb{1} \\ -\partial^{-2} [\partial, \partial] \partial^{-2} - \partial^{-2} [\partial, \partial] \partial^{-2} [\partial, \partial] \partial^{-2} + \dots \end{aligned} \quad (8.4)$$

and use the identity

$$[\partial_\alpha, \partial_\beta] F[C_{xx}] = \frac{\delta F[C_{xx}]}{\delta \sigma_{\alpha\beta}(y)} \Big|_{y=x+0}^{y=x-0} \quad (8.5)$$

The last step was to represent the inversion of the point derivative operator ∂^{-2} as a sum over the Brownian path Γ in 4D space of the functional $J[C_{xx}]$ transported along this path by adding "wires" to the loop

$$\begin{aligned} -\partial^{-2} J_\nu[C_{xx}] &= \lambda \int d^4 z \int \mathcal{D}\Gamma_{xz} \\ &\oint_{\Gamma_{zx} \cdot C_{xy} \cdot C_{yx} \cdot \Gamma_{xz}} dy_\nu \delta^4(z-y) W[\Gamma_{zx} \cdot C_{xy}] W[C_{yx} \cdot \Gamma_{xz}] \end{aligned} \quad (8.6)$$

The important property of this bootstrap equation is that it involves the path integral over Brownian paths Γ_{xz} in Euclidean 4D space, which is the basis for the further reconstruction of the gluon propagators. This integral representation is depicted on Fig.11.

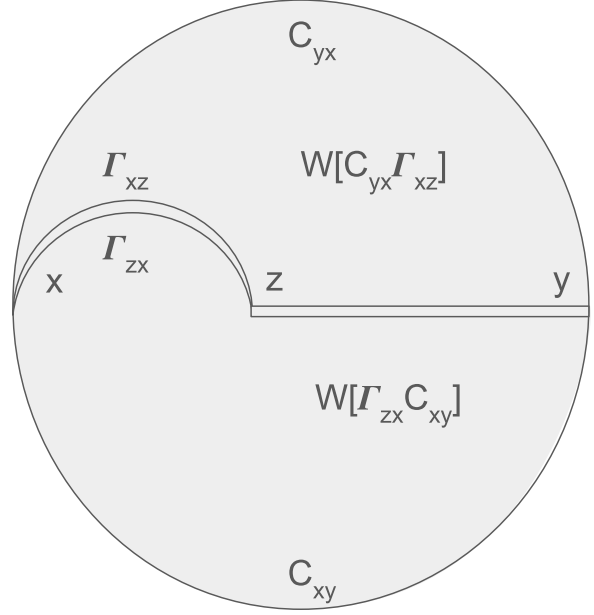


Figure 11: The path integral in (8.6) with delta function represented by a straight double line, and Brownian paths Γ_{xz}, Γ_{zx} by a crescent.

8.2. Gluon graphs by iterations of Bootstrap equation

In the old MM papers [7, 25], the bootstrap equation was iterated in the coupling constant λ , starting with $W[\mathbb{1}] = 1$.

The derivation was rather tedious, but it faithfully reproduced conventional planar graphs, including Faddeev-Popov ghost loops. The first order planar graph follows immediately from the (8.6), as shown on Fig. 11, by replacing W by 1 in the path integral, after which this path integral yields the gluon propagator $1/(x-y)^2$. The second order graphs are already nontrivial (see [7], Appendix B). This is where the Faddeev-Popov ghost loops emerge directly from iterations of the bootstrap loop equation; this is also where the beta function appears, leading to asymptotic freedom with its running coupling constant. Perturbative QCD is reproduced by the bootstrap equation to all orders, as it was further investigated in [25].

Let us summarize this section as follows.

- The planar MM equation (2.10) can be transformed into an equivalent path integral equation by inverting the non-commutative operator ∂ . The new equation expresses the area variation as a non-linear functional of $W[C]$, which can be represented as a series of frame diagrams, like the one in Fig. 11.
- Frame diagrams can be constructed by means of a certain operator technique. The frame diagram of an arbitrary order looks like a planar

tree with windows glassed with W functionals. Integration over internal paths is implied.

- Perturbatively, when $W[C_{ab}] \Rightarrow 1$ in a framed graph, the sums over Brownian paths produce the gluon propagators, and the commutators $[\partial, \bar{\partial}]$ generate proper tensor numerators in the gluon graphs.
- The analytical expression for the frame diagram is manifestly gauge invariant. It contains only gauge-invariant (and parametric-invariant) quantities: W functionals of closed loops and line elements, $d\theta \dot{C}_\mu(\theta)$. The loop integration goes along the external loop, C_{xx} , as well as along internal paths (with appropriate coefficients).
- The bootstrap equation is equivalent to the system including the Bianchi identity and the planar equation accompanied by euclidean boundary conditions. For this reason, iterative solution of the bootstrap equation recovers uniquely Faddeev-Popov perturbation theory (see appendices of [7] and [25]).
- Various parts of the loop integral correspond to various graphs of ordinary perturbation theory including ghost loops. Being gauge variant separately, these graphs combine into a manifestly gauge-invariant diagram in the loop space.

9. Effective action, its geometry and its singularities

The formal proof that the Elfin determinant $Z[C]$ in the limit of large Elf mass and vanishing normalization $Z[1]$ satisfies the MM loop equation with an asymptotically free coupling constant $\lambda \rightarrow 0$ raises many questions. The loop equation is local, due to the delta function on the right side. However, as we all know, the perturbative expansion of $W[C]$ in powers of the 't Hooft coupling constant λ produces the planar graphs inside the loop C , which are nonlocal functionals of the loop because of the massless gluon propagator $\delta_{\mu\nu}/(x-y)^2$ in coordinate space. We get a sequence of logarithmically divergent integrals like

$$\oint_C dx_\mu \oint_{C_{xx}} dy_\mu / (x-y)^2,$$

leading to logarithmic singularities at the cusps of the loop C .

Where is this non-locality hiding in the Elfin theory, and how will these logarithms emerge? In this section, we dig deeper into the formal solution we have found, searching for the perturbative singularities of planar QCD.

9.1. Local expansion of the heavy fermion determinant

The physical interpretation of our confining factor arises from the effective action of a heavy Dirac fermion propagating on the minimal surface Σ . In the limit of large mass m , the fermion determinant $W_{\text{eff}} = -\log \det(\not{D} + m)$ admits a local heat-kernel expansion, as we have found in previous sections:

$$W_{\text{eff}}[C] \approx \int_{\Sigma} d^2z \sigma e^{2\rho} + \frac{|\partial_z \rho|^2}{3\pi} + O(m^{-2}); \quad (9.1)$$

$$\rho(z, \bar{z}) = \frac{\log(\bar{\lambda}(\bar{z})\lambda(z)) + \log(\bar{\mu}(\bar{z})\mu(z))}{2}; \quad (9.2)$$

The leading term is the Area Law, where the tension $\sigma \sim m^2$ provides the confining potential. The subleading term is the conformal anomaly (Liouville action). There is always another zero mode confining factor $G[C] = \exp(-\delta\sigma S[C])$, renormalizing the string tension σ , as we found in the previous work [1]. Equivalently, the area term generated in the heavy-mass expansion of the determinant provides an additive renormalization of the vacuum-energy/string tension sector, already parametrized by the zero-mode dressing $\exp((\cdot) - \kappa S[C])$; only the sum defines the single physical string tension $\sigma_{\text{phys}} = 2\sqrt{2}\kappa_{\text{phys}}$ in the continuum theory, while M acts strictly as a regulator scale removed in the local limit.

In our framework, we do not integrate over fluctuating metrics (which would lead to the Polyakov-Liouville anomaly). Instead, the surface Σ is the rigid solution to the Plateau problem bounded by the loop C . Consequently, the anomaly term becomes a functional of the boundary loop itself:

$$S_{\text{shape}}[C] = \frac{1}{12\pi} \int_D |\partial_z (\log \bar{\lambda} \lambda + \log \bar{\mu} \mu)|^2 d^2z \quad (9.3)$$

This functional is non-local with respect to the loop coordinates $C_\mu(\theta)$, as it requires solving the bulk Laplace equation to determine $\lambda(z), \mu(z)$. It represents the "Loewner Energy" [26] of the loop, acting as a geometric stiffness that penalizes deviations of the flux tube cross-section from circularity.

9.2. Cusp singularities and the Hilbert transform

The analytic structure of the minimal surface provides a natural regularization of the ultraviolet divergences associated with the Wilson loop, while correctly reproducing the universal singularities of Gauge Theory. The holomorphic tangent vector is reconstructed from the boundary loop velocity \dot{C}_μ via the Hilbert transform H :

$$2ie^{i\theta} f'_\mu(e^{i\theta}) = \dot{C}_\mu(\theta) + iH[\dot{C}_\mu](\theta), \quad (9.4)$$

$$H[u](\theta) = \frac{1}{2\pi} \text{P.V.} \int d\theta' \cot\left(\frac{\theta - \theta'}{2}\right) u(\theta') \quad (9.5)$$

For smooth loops (such as the circle or helicoid), $H[\dot{C}]$ is smooth, and the area density is finite everywhere. However, for polygonal loops used in

scattering amplitudes, the tangent vector \dot{C}_μ has discontinuities (cusps).

At a cusp, the Hilbert transform of the step function generates a logarithmic singularity:

$$H[\dot{C}_\mu](\theta) \sim \log|\theta - \theta_{cusp}| \quad (9.6)$$

This propagates into the area tensor $F_{\mu\nu} = \text{Re } f'_{[\mu} \text{Im } f'_{\nu]}$, causing the area derivatives of the minimal surface to diverge logarithmically at the corners of a polygonal loop. This divergence is the geometric origin of the Cusp Anomalous Dimension ($\Gamma_{cusp} \log \Lambda_{UV}$) and the Sudakov double logarithms found in perturbative QCD. Thus, the Hodge-dual minimal surface captures (or at least imitates) the collinear singularities of the gauge theory through the poles of the Hilbert kernel.

9.3. New view at the cusp singularity

The logarithmic singularity at the cusps, derived in perturbative QCD by Korchemsky and Radyushkin [27], finds a natural interpretation in our framework. In standard perturbation theory, the Wilson loop with a cusp of angle γ (in Euclidean space) exhibits a divergence:

$$\begin{aligned} \log W &\sim -\Gamma_{cusp}(\gamma) \log(\Lambda_{UV} L) \\ &\sim -\frac{\lambda}{8\pi^2} (\gamma \cot \gamma - 1) \log(\Lambda_{UV} L) \end{aligned} \quad (9.7)$$

In the standard renormalization group approach, this divergence is absorbed into a multiplicative renormalization constant. However, in our geometric framework, the logarithmic divergence arises physically from the energy density of the minimal surface near the corner, generated by the pole in the Hilbert transform.

Rather than removing this term, we observe that the theory possesses an intrinsic ultraviolet cutoff Λ determined by the mass scale of the heavy Elf particles, which is equivalent to the regularization of the fermion determinant. In the continuum limit $\Lambda \rightarrow \infty$, the bare 't Hooft coupling $\lambda(\Lambda)$ must vanish according to the law of asymptotic freedom:

$$\lambda(\Lambda) \approx \frac{24\pi^2}{11 \log(\Lambda/\Lambda_{QCD})} \quad (9.8)$$

Consequently, the "divergent" cusp energy becomes the product of a vanishing coupling and a diverging geometric factor. This product tends to a finite, universal limit:

$$\begin{aligned} E_{cusp} &\sim \lim_{\Lambda \rightarrow \infty} \lambda(\Lambda) \log(\Lambda L) \times (\text{Geometric Factor}) \\ &= \text{finite} \end{aligned} \quad (9.9)$$

Specifically, using the one-loop beta function coefficient, the cusp contribution to the effective action becomes a scale-invariant geometric potential:

$$S_{cusp} = \frac{3}{11} (\gamma \cot \gamma - 1) \quad (9.10)$$

This mechanism is strictly analogous to the continuum limit in Lattice Gauge Theory, where the bare coupling $g_0 \rightarrow 0$ as the lattice spacing $a \rightarrow 0$ to keep physical masses finite. In our induced QCD, the cutoff has a physical and mathematical origin in the regularization of the minimal surface, so the limit $m \rightarrow \infty$ (where $\lambda \rightarrow 1/(\beta_0 \log m)$) has a precise mathematical meaning, replacing the formal subtraction of infinities with a finite limiting process.

9.4. Spinor factorization and the geometry of Gauss maps

The twistor factorization [28] of the null tangent vector $f'_{ab} = \lambda_a \mu_b$ leads to a factorization of the induced metric on the worldsheet, as summarized in our Appendix B. Using the isomorphism $SO(4) \cong SL(2)_L \times SL(2)_R$, the metric density factorizes into the product of invariant norms of the left and right spinors:

$$e(z, \bar{z}) = 2\sqrt{2} f'_\mu \bar{f}'_\mu = \sqrt{2} \bar{\lambda} \lambda \bar{\mu} \mu \quad (9.11)$$

The area derivative (3.8) in the spinor representation simplifies as follows

$$\frac{\delta S_\pm}{\delta \sigma_{\alpha\beta}} = -n_i^\pm \eta_{\alpha\beta}^{i\pm}, \quad (9.12)$$

$$n_i^\pm = \left\{ \frac{\bar{\lambda} \sigma_i \lambda}{\bar{\lambda} \lambda}, \frac{\bar{\mu} \sigma_i \mu}{\bar{\mu} \mu} \right\} \quad (9.13)$$

The Liouville field $\rho = \frac{1}{2} \log(f'_\mu \bar{f}'_\mu)$ splits into a sum of potentials:

$$\begin{aligned} \rho(z, \bar{z}) &= \Phi_L(z, \bar{z}) + \Phi_R(z, \bar{z}), \\ \text{where } \Phi_{L,R} &= \left\{ \frac{1}{2} \log \bar{\lambda} \lambda, \frac{1}{2} \log \bar{\mu} \mu \right\}; \end{aligned} \quad (9.14)$$

Geometrically, Φ_L and Φ_R are the Kähler potentials for the maps from the worldsheet to the projective spinor spaces \mathbb{CP}_L^1 and \mathbb{CP}_R^1 . These maps n_i^\pm are identified with the Left and Right Gauss maps of the minimal surface [29]. In our particular case of the Hodge-dual minimal surface S_χ , the area element reduces to a single Gauss map for a given Hodge chirality $\chi = \pm 1$.

$$\Sigma_{\mu\nu} \propto n_i^\pm \eta_{\alpha\beta}^{i\pm} H^\mp(z, \bar{z}); \quad (9.15)$$

$$H^\pm(z, \bar{z}) = \{ \bar{\lambda} \lambda, \bar{\mu} \mu \}; \quad (9.16)$$

The area element still depends on both left and right spinors, but it transforms under $SO(4)$ as a single Gauss map, corresponding to its chirality. The anomalous part of the effective action, $I \propto \int (\nabla \rho)^2$, therefore expands into:

$$I = I_L[\lambda] + I_R[\mu] + 2 \int_D \nabla \Phi_L \cdot \nabla \Phi_R d^2 z \quad (9.17)$$

The first two terms are the actions for the Sigma models on \mathbb{CP}^1 , which are topological invariants (proportional to the winding numbers of the Gauss

map). The third term represents a non-trivial interaction between the left and right sectors. Unlike the metric, the action does not decouple; this interaction term measures the integrated correlation between the curvatures of the left and right spinor bundles. It represents the geometric energy cost of the relative orientation of the left and right Gauss maps required to satisfy the boundary conditions.

10. Momentum loops and continuum limit

10.1. Regularization, renormalizability, and the microscopic definition of Planar QCD

Since the inception of QCD half a century ago, the understanding of its regularization and renormalizability has evolved significantly. Currently, Lattice QCD serves as the standard microscopic definition of the theory. In this framework, renormalizability reduces to the mathematical statement that, in the limit of a vanishing bare coupling constant, the physical mass scale Λ_{QCD} (measured in units of inverse lattice spacing) exponentially approaches zero. Consequently, the lattice spacing vanishes when measured in observable physical units such as the proton radius.

However, the lattice definition comes at a cost: it explicitly breaks the continuous symmetries of four-dimensional Euclidean space, from the rotation group $O(4)$ to subtle topological structures like the Hodge duality of the area tensor. For instance, exact instanton solutions or Hodge-dual minimal surfaces do not exist on a discrete grid; they only emerge in the continuum limit.

These disadvantages are compensated by the universality of the Renormalization Group (RG) flow. It is well-established (though unproven) that asymptotically free theories reach a universal fixed point at large scales, regardless of the specific microscopic regularization, provided the symmetries are restored in the infrared. This universality allows for various microscopic definitions of QCD, provided they land in the correct phase (the basin of attraction of the asymptotically free fixed point).

History offers cautionary tales. The large- N reduced Eguchi-Kawai model, for example, encountered unphysical fixed points. Similarly, the original Induced QCD proposal [23]—which attempted to induce gauge dynamics via heavy free fermions with vanishing color currents on a lattice—failed because the theory collapsed into the wrong phase rather than asymptotically free QCD. Our Elfin theory is a variation on this theme: heavy free fermions inducing QCD. However, the critical distinction is that our fermions live on a *rigid minimal surface* rather than a four-dimensional lattice. This geometric constraint keeps the theory non-trivial in the local limit, making it a viable regulator for Planar QCD.

A central question arises regarding the *renormalization* of the Wilson loop itself. Standard perturbation theory dictates that $W[C]$ requires multiplicative renormalization to remove divergences associated with cusps and self-intersections. Are we obliged to redefine the loop equation to make the coordinate-space Wilson loop finite in the local limit?

We argue that this is a misguided requirement that obscures the underlying dynamics. Physical renormalizability demands only the existence of a universal mass scale Λ_{QCD} and the finiteness of *observable scattering amplitudes*. The Wilson loop $W[C]$ is an intermediate, off-shell quantity. Physical observables involve path integrals over quark trajectories, which are governed by a Brownian measure. A Brownian trajectory is nowhere differentiable; it consists of an infinite density of cusps. Attempting to renormalize the Wilson loop for a smooth contour C is physically artificial because the dominant contributions to the path integral come from fractal paths where the concept of a "cusp angle" is ill-defined.

Therefore, instead of forcing the non-renormalizable coordinate Wilson loop to be finite, we adopt a radically different strategy:

1. We keep the theory regularized at the level of the Wilson loop $W[C]$ by the finite Elf mass m (which acts as the UV cutoff).
2. We perform the summation over quark paths to construct the momentum loop amplitude $W[P]$.
3. Only *after* transitioning to Momentum Loop Space do we take the local limit ($m \rightarrow \infty$).

As demonstrated in this paper, the transition to momentum space integrates out the geometric singularities. The momentum amplitude $W[P]$ remains finite and satisfies an algebraic-differential equation. By taking the bare coupling to zero as $m \rightarrow \infty$ in accordance with the RG beta function, we recover the finite, universal observables of Planar QCD without ever needing to define a "renormalized" Wilson loop in coordinate space.

10.2. Momentum loop path integral

As we discussed in the previous section, the ordinary Wilson loop is not directly observable, and its notorious singularities are merely intermediate results that will eventually disappear (cancel or integrate out) in observables.

Unlike the standard Feynman-Schwinger world-line representation in coordinate space, which is inherently plagued by the UV cusp singularities of $W[C]$, we utilize the phase-space path integral representation introduced by the author in [30]. In this formulation, the exact planar quark amplitude factorizes strictly into a universal kinematic Dirac

phase-space trace $\mathcal{K}[P]$ and the dynamical gluonic momentum-loop functional $W[P + Q]$.

The amplitude for the propagation of a free Dirac particle in the phase-space loop (the Dirac loop) is:

$$\mathcal{K}[P] = \text{tr} \hat{P} \exp \left(- \int_0^\infty d\tau (i\gamma_\mu P_\mu(\tau) + m_q) \right); \quad (10.1)$$

The full amplitude for the quark loop in the Planar QCD vacuum, with some external momenta q_1, \dots, q_n injected into these amplitudes, is a product of the Dirac loop and Wilson loop times the vertex factor for the injection of external momenta:

$$A[q_1 \dots q_n] \propto \int \prod_{\text{ordered } \tau_k} d\tau_k \int \mathcal{D}P W[P + Q] \mathcal{K}[P]$$

$$Q_\mu(\tau) = \sum_k q_k \Theta(\tau - \tau_k); \quad \sum_k q_k = 0 \quad (10.2)$$

$$W[P] = \lambda \int \mathcal{D}C W[C] \exp \left(i \int d\tau P_\mu(\tau) \dot{C}_\mu(\tau) \right) \quad (10.3)$$

For these amplitudes, the fundamental domain D for the minimal surface is used as the upper semi-plane $\text{Im} z > 0$, with the loop $C(x)$ corresponding to the real axis $x = \text{Re} z$. This formula for the quark current amplitude in Planar QCD is illustrated in Figure 12.

The momentum loop amplitude $W[P]$ was introduced in our papers [31, 30, 32] and was recently used in the solution of the Navier-Stokes turbulence problem [33, 3]. The advantage of the momentum loop space is that the loop equation for $W[P]$ is purely algebraic/differential. There are no delta functions; just polynomial functionals of the local momentum $P(\tau)$ and some non-singular functional derivatives of $W[P]$. The coordinate delta function, which leads to all perturbative singularities such as logarithmic divergences at the cusps, disappears in momentum space in the same way that it disappears from the Klein-Gordon equation

$$(-\partial^2 + M^2)G = \delta(x - x_0) \Rightarrow (p^2 + M^2)\tilde{G} = 1$$

10.3. The Momentum loop equation

The MM equation (2.10), when transformed into the momentum loop equation (MLE) by functional Fourier transform, also has a simple algebraic structure (expanded in so-called Magnus invariant forms [34])

$$W[P] = \sum_n \mathcal{W}_{\alpha_1, \dots, \alpha_n}^{(n)} \Omega_{\alpha_1, \dots, \alpha_n}^n [P]; \quad (10.4)$$

$$\Omega_{\alpha_1, \dots, \alpha_n}^n [P] = \hat{T} \int \prod d\theta_k P'_{\alpha_k}(\theta_k) \quad (10.5)$$

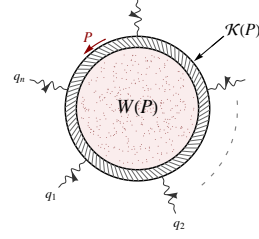


Figure 12: The momentum loop amplitude, $A(q_1, \dots, q_n)$ with the inside part of the wheel corresponding to Momentum loop $W[P]$, and the outer rim corresponding to Dirac path amplitude $\mathcal{K}[P]$. The paths $P(t)$ are random, interacting with inner geometry of the string surface represented by amplitude $W[P]$.

where $\hat{T} \int$ stands for the ordering of the integration angles on the circle. The MLE becomes an algebraic differential equation in terms of Magnus forms (a.k.a iterated path integrals):

$$Q_\nu [P] W[P] = \int_0^{2\pi} d\theta \frac{\delta}{\delta P_\nu(\theta)} (W[P_{\theta, \theta}] W[P_{\theta, 2\pi}]); \quad (10.6)$$

$$Q_\nu [P] = T^{\alpha\beta\gamma} \nu \Omega_{\alpha\beta\gamma}^3 [P]; \quad (10.7)$$

$$T^{\alpha\beta\gamma} \nu = \delta_{\alpha\beta} \delta_{\gamma\nu} + \delta_{\gamma\beta} \delta_{\alpha\nu} - 2\delta_{\alpha\gamma} \delta_{\beta\nu}; \quad (10.8)$$

The algebraic expression on the left side emerged as a Fourier transformation $\frac{\delta}{\delta C} \Rightarrow iP$ of the operator

$$\hat{L}_\nu(0) = \partial_\mu \frac{\delta}{\delta \sigma_{\mu\nu}(0)}$$

$$= T^{\alpha\beta\gamma} \nu \frac{\delta^3}{\delta \dot{C}_\alpha(\theta - 0) \delta \dot{C}_\beta(\theta) \delta \dot{C}_\gamma(\theta + 0)} \quad (10.9)$$

The notorious delta function on the right (which caused all the perturbative singularities in $W[C]$) disappeared in the Fourier integral (see original papers [31, 30, 32] for details).

Here is how this happens in our new framework, with the closed loop described by the position field $C_\nu(\theta)$ subject to the closure constraint $C(2\pi) = C(0)$. The linear functional measure in loop space can be written in one of two equivalent forms (with $v(\theta) = C'(\theta)$)

$$\mathcal{D}C \propto \delta^4(C(2\pi) - C(0)) \prod_{\theta=0}^{2\pi} d^4 C(\theta)$$

$$\propto \delta^4 \left(\oint v(\theta) d\theta \right) \prod_{\theta=0}^{2\pi} d^4 v(\theta) \quad (10.10)$$

It is factorizable at self-intersections, which leads to the factorization in the momentum loop equa-

tion, with the delta function absorbed by a measure

$$\begin{aligned}
& \delta^4(C(2\pi) - C(0)) \delta^4(C(\theta_1) - C(\theta_2)) \prod_{\theta=0}^{2\pi} d^4 C(\theta) \\
&= \delta^4(C(\theta_1) - C(\theta_2)) \prod_{\theta'=\theta_1}^{\theta_2} d^4 C(\theta') \\
& \delta^4(C(\theta_2) - C(\theta_1 + 2\pi)) \prod_{\theta''=\theta_2}^{\theta_1+2\pi} d^4 C(\theta'') \\
&\implies DC \delta^4(C(\theta_2) - C(\theta_1)) = DC_{12} DC_{21} \\
&\implies \int DC \hat{L}_\nu(\theta_1) W[C] \exp\left(i \oint P \cdot C'\right) = \\
& \int DC_{12} \int d\theta_2 \overset{\leftarrow}{C}'_\nu(\theta_2) \exp\left(i \int_{\theta_1}^{\theta_2} P \cdot C'\right) W[C_{12}] \\
& \int DC_{21} \exp\left(i \int_{\theta_2}^{\theta_1+2\pi} P \cdot C'\right) W[C_{21}] \\
&\implies L_\nu W[P_{11}] = \int d\theta_2 \overset{\leftarrow}{\delta}_{\delta P_\nu(\theta_2)} W[P_{12}] W[P_{21}]
\end{aligned} \tag{10.11}$$

Here

$$\overset{\leftarrow}{f}(x) = \frac{f(x+0) + f(x-0)}{2}$$

After conformal transformation mapping the unit disk to the upper semiplane, we map the circle origin $\theta = \pm\pi$ by $x = \tan(\theta/2)$ to $x = \pm\infty$.

For our final local solution, however, we shall use a different gauge condition for diffeomorphisms, which is more adequate for string theory. The gauge ambiguity of the parametrization of the linear measure (10.10) leads to the overcounting of every loop by an infinite volume of the gauge orbit. This volume must be factored out of the measure to avoid overcounting. This refactoring seems incompatible with the above factorization of the loop measure over the self-intersecting loops, but upon closer inspection, the paradox disappears. The measure must be factored by the total volume of its isometries, which, in the case of a simple loop, reduces to the volume of diffeomorphisms of a unit circle $\text{Vol}(\text{Diff}(S^1))$; however, in the case of a self-intersecting loop, there are two periodic parts; therefore, such a loop *maps twice* the unit circle to \mathbb{R}^4 . The volume of these isometries is $(\text{Vol}(\text{Diff}(S^1)))^2$, which matches the product of linear measures on the right side of the factorization identity. So, the physical measure, with single counting of each loop, factorizes in the MM equation in momentum loop space.

10.4. Equivalence of loop diffusion operator to the third Magnus form

In momentum loop space, the loop diffusion operator L_ν from (10.9) is recast as a trilinear product

of the momentum field $P(\theta)$:

$$T^{\alpha\beta\gamma} i^3 P_\alpha(\theta_1) P_\beta(\theta_2) P_\gamma(\theta_3); \tag{10.12}$$

$$\theta_1 = 2\pi - \epsilon, \theta_2 = 0, \theta_3 = +\epsilon; \quad \epsilon \rightarrow +0; \tag{10.13}$$

By utilizing the integral representation

$$P(\theta) = \oint d\tau P'(\tau) \Theta(\theta - \tau) \tag{10.14}$$

where $\Theta(\theta - \tau)$ denotes the periodic theta function on the circle, the trilinear product is transformed into a general triple integral of the momentum derivative P' . The rigorous mathematical foundation for expanding loop functionals in such iterated integrals is provided by Chen's theorem [35]. Chen established that the algebra of iterated path integrals separates points in loop space, meaning that the infinite hierarchy of these integrals forms a strictly complete functional basis. This guaranties that our formal expansion in terms of Magnus forms is exhaustive.

Through direct tensor contraction, the kinematic tensor $T^{\alpha\beta\gamma}_\nu$ implements the exact Dynkin projector [36] onto the nested double commutator $[\hat{D}_\alpha, [\hat{D}_\alpha, \hat{D}_\nu]]$. Here, $\hat{D} = \partial + A$ represents the covariant derivative operator within the gauge field representation of the Wilson loop. This mapping identifies the associative word structure of the integrated momentum field with its unique Lie algebra representation.

Consequently, by Ree's Theorem [37] for Free Lie Algebras [38], this operator identically annihilates the symmetric shuffle ideal associated with the triple integral. As the point-split coordinates θ_i collapse to the origin, the periodic step-functions define a strictly cyclically ordered simplex. This unique parametric-invariant Lie projection ensures that the functional converges exactly to the third-order Magnus form $\Omega^{(3)}$. Direct evaluation of this triple integral, mediated by the T projector, confirms this algebraic correspondence and yields the canonical normalization coefficient $1/6$.

10.5. Algebraic recurrence for the Momentum Loop Equation

The Momentum Loop Equation (MLE) exhibits a profound simplification when the momentum functional is represented as a Magnus-ordered exponential:

$$W[P] = \text{tr} \left\{ \hat{\mathcal{T}} \exp \left(\int d\theta \hat{X}_\mu P'_\mu(\theta) \right) \right\} \tag{10.15}$$

where \hat{X}_μ represents the operator position of the string endpoint in spacetime. Expanding this trace in Magnus forms Ω^n , we obtain universal tensor coefficients $\mathcal{W}_{\alpha_1 \dots \alpha_n}^{(n)} = \text{tr} \{ \hat{X}_{\alpha_1} \dots \hat{X}_{\alpha_n} \}$. The functional derivative acts algebraically on this structure,

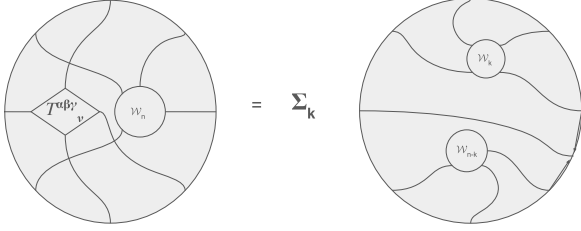


Figure 13: The recurrent equation for the coefficient tensor parameters \mathcal{W}^n in the Magnus expansion (10.4). The external circle represents the unit circle where the angular parameter belong. The inner round blobs with wavy legs landing on a unit circle represent the \mathcal{W}^n tensors, the rhombus with four wavy legs represents the 4-tensor T in (10.8). Two arrows on the right side correspond to functional derivatives $\frac{\delta}{\delta P_\nu}$ bringing commutators by momentum area derivatives (10.16). These equations relate the higher \mathcal{W}^n tensors to the lower ones, which allows the solution depending on some gauge parameters, undetermined by the recurrent relations.

bringing down exact commutator insertions:

$$\frac{\delta}{\delta P_\mu(\theta)} \text{tr} \left\{ \hat{T} \exp \left(\int d\theta' \hat{X}_\alpha P'_\alpha \right) \right\} = P'_\nu(\theta) \text{tr} \left\{ [\hat{X}_\mu, \hat{X}_\nu] \hat{T} \exp \left(\int_\theta^{\theta+2\pi} \hat{X}_\alpha P'_\alpha \right) \right\} \quad (10.16)$$

By applying this exact derivative formula, the Makeenko–Migdal loop equation sheds its coordinate-space singularities and collapses into a finite, recursive combinatorial algebra. On the left-hand side, the kinematic operator Q_ν acts via a shuffle product between the 3-index $T_\nu^{\alpha\beta\gamma}$ tensor and the lower-order $\mathcal{W}^{(n-3)}$ coefficients. On the right-hand side, the integration over θ seamlessly sews the split traces back together, yielding an algebraic sum over commutator insertions without requiring cyclic sums or residual functional calculus. These relations are depicted in Fig.13 Because the physical momentum loop is closed ($\oint P' d\theta = 0$), the first-order form identically vanishes: $\Omega_\alpha^1 = 0$. This topological constraint generates a formal “shuffle ideal” that relates higher-order Magnus forms. We must therefore equate the left and right sides of the MLE modulo this ideal. The null space of this ideal natively gives rise to symmetric gauge ambiguities that dynamically decouple from physical observables.

10.6. Exact solution up to $\mathcal{O}(P'^7)$ and non-analyticity of the Taylor expansion

To construct the exact solution to the Momentum Loop Equation (MLE) in the perturbative regime of small loop momenta, we employ the functional Taylor–Magnus expansion of $\mathcal{W}[P]$. Because the MLE evaluates the functional derivative on closed loops, the geometric ansatz must natively reflect this exact topological closure.

When the functional area derivative acts, it splits the integration domain into two subloops on the right-hand side of the equation. To analytically enforce the closure of these subloops within the continuous path integral, we introduce a modified momentum derivative containing a boundary Dirac delta function:

$$P'_{\text{closed}}(\theta') = P'(\theta') + \Delta P \delta(\theta' - \theta_0) \quad (10.17)$$

where $\Delta P = \int P' d\theta$ is the boundary gap of the subloop, and θ_0 is the position of the gap ($\theta_0 = \theta$ and 2π for the respective right-hand side subloops).

When substituted into the iterated integrals of the Magnus expansion, the δ -function explicitly inserts the macroscopic gap vector $\Delta P_\mu \equiv \Omega_\mu^{(1)}$ precisely at the boundaries of the integration domain. Because ΔP corresponds to the first-order Magnus form, this topological closure modifies the n -th order form by subtracting the product $\Omega^{(1)}\Omega^{(n-1)}$. By the integration-by-parts identity of the Magnus expansion (the shuffle relations), this product translates exactly to the sum of all interleaved operator positions. The loop-closing transformation thus yields the modified Magnus form:

$$\tilde{\Omega}^{(n)} = \Omega^{(n)} - \sum_{k=1}^{n-1} \Omega^{(n)}(\text{interleaved}) \quad (10.18)$$

This subtraction mathematically enforces the closed-loop Shuffle Ideal, identically restoring the cyclic symmetry of the invariant tensors $\mathcal{W}^{(n)}$. Operating in the pure closed-loop vacuum, all odd-parity traces identically vanish ($\mathcal{W}^{(2k-1)} = 0$). The functional $\mathcal{W}[P]$ is therefore expanded in a basis of cyclic symmetric, invariant tensor polynomials constructed entirely from the Kronecker metric $\delta_{\mu\nu}$.

Substituting this closed-loop basis into the MLE, we dynamically equate the left-hand side kinematic shuffle products against the right-hand side discrete commutator series. Starting from the perturbative vacuum $\mathcal{W}^{(0)} = 1$, the algebraic system successfully yields finite, exact solutions for the lowest-order tensors. The fundamental string tension enters at $\mathcal{W}^{(2)}$, and the kinematic stress generated by the loop derivative exactly constrains the cyclic symmetric pairings of $\mathcal{W}^{(4)}$ and $\mathcal{W}^{(6)}$. (The explicit analytic formulas for these invariant tensors are provided in Appendix C for small n . Crucially, Appendix C also contains the exact finite-dimensional linear algebra diagnostics (Table C.1) and the explicit Fredholm inconsistency proof demonstrating the absolute lack of solutions at $\mathcal{W}^{(8)}$. The general algorithmic implementation is provided in [39].)

10.7. The Reasons for the Failure of the Magnus Expansion for $\mathcal{W}[P]$

The general reason for the breakdown of the expansion at this order is that the linear space of $\mathcal{W}^{(8)}$ invariant tensors—which is strictly constrained by

the Shuffle Ideal and cyclic symmetry—possesses a significantly smaller matrix rank than the highly specific multilinear stress generated by the crossing Kronecker deltas of $\mathcal{W}^{(4)} \times \mathcal{W}^{(4)}$.

This is not a heuristic observation, but a rigorously quantified algebraic contradiction. As detailed in [Appendix C](#) (and summarized in [Table C.1](#)), extracting the exact linear system at the 8th order yields 379 geometric constraints but only 212 available parameters (which exhaustively includes the full $\mathcal{W}^{(8)}$ basis, all residual lower-order free parameters, and all gauge/ideal freedoms). The resulting system explicitly violates the Fredholm alternative condition, yielding a strictly positive rank deficiency ($\Delta\text{rank} = 1$) and a non-zero projection of the inhomogeneous stress onto the left-null space of the kinematic matrix.

Consequently, it is mathematically impossible for any choice of linear coefficients, or the remaining lower-order terms, to absorb and cancel this rigid cross-term stress. This yields an irreducible algebraic contradiction in the tensor matching.

The physical meaning of this failing Taylor–Magnus expansion is of paramount importance. It demonstrates that the MLE is finite, free of UV divergences, and expandable in a functional Taylor series up to $\mathcal{O}(P^6)$. However, the geometric contradiction at the 8th order rigorously proves that the exact solution $W[P]$ is **not an analytic functional** of the bounding loop $P(\theta)$. It cannot be indefinitely expanded in a continuous Taylor–Magnus series.

Remark 10.1 (The Vector vs. Scalar Dimensionality Mismatch). *The fundamental root of this non-analyticity is that the loop equation is inherently a vector equation,*

$$\hat{L}_\nu W = \int \frac{\delta}{\delta P_\nu} (W \times W), \quad (10.19)$$

governing a scalar functional $W[P]$. The number of independent tensor structures available for a scalar functional grows strictly slower than those required for a free-index vector equation (growing approximately four times slower in $d = 4$). This is why, at some critical level of the Magnus expansion, there will inevitably be more vector equations than available scalar parameters.

This is a foundational feature of the loop equation: it descends directly from the vector Yang–Mills equations of motion, which dictate that a local vector loop equation (evaluated at a fixed point on the contour) must be satisfied. Resolving this overdetermined system demands a deep mathematical “conspiracy” among the internal degrees of freedom within $W[P]$. The generic Taylor–Magnus expansion simply lacks the internal geometric structure to orchestrate this conspiracy.

(Interestingly, this exact same vector-versus-

scalar mismatch is fatal to all naive bosonic string theories of QCD: the loop equations are strictly vector equations, but the Nambu–Goto string Laplace operator is a scalar, meaning a scalar area-derivative constraint fundamentally cannot capture the full vector loop equation without an anomaly.)

However, **our theory natively provides this required conspiracy!** In the previous sections, we derived exact **vector** equations for the Elfin determinant on the Hodge-dual minimal surface, and these vector equations are satisfied across all vector components. This mathematical miracle is made possible by Hodge duality and the planar factorization of the Majorana determinant on this Hodge dual surface.

The profound physical reasons for this non-analyticity will become fully apparent in later sections, when we construct the continuum solution and reduce it to the exact twistor string path integral. In that formulation, the formal Taylor expansion in $P(\theta)$ corresponds to the perturbative expansion of the exact exponential phase factor:

$$\exp \left(2i \int d\theta P_\alpha(\theta) \text{Im}(z\lambda\sigma_\alpha\mu) \Big|_{z=e^{i\theta}} \right). \quad (10.20)$$

For such a functional Taylor series to converge, the boundary twistors $\lambda(z)$ and $\mu(z)$ would need to be strictly bounded. The algebraic contradiction at the 8th order rigorously proves this is not the case; the path integral is not convergent in a perturbative Taylor expansion.

As we will discuss in detail when deriving the twistor string path integral, the integration over the momentum loops is not dominated by smooth, small P variations at all. When integrated alongside the Dirac target-space product $\text{tr} \hat{\mathcal{T}} \exp(-i \int d\theta \gamma_\mu P_\mu(\theta) + m_0)$, we encounter strictly ultra-local integrals. At every angle θ , we integrate out the local value $P(\theta)$. Because there are no worldline kinetic derivatives $\partial_\theta P$ in the action, the path integral completely factorizes point-by-point. As a result, the dominant trajectories are neither continuous nor dominated by small P variations. We therefore conclude that the MLE is completely finite and anomaly-free, but its true continuum solution is inherently non-perturbative and cannot be Taylor-expanded beyond the 6th order.

10.8. The General Master Field \hat{X} and the Word Space

To fully grasp the physical and mathematical implications of the geometric breakdown at $\mathcal{W}^{(8)}$, it is instructive to re-examine the loop expansion through the lens of the Master Field construction.

A natural mathematical objection arises when considering the breakdown of the Taylor–Magnus

expansion: Does the representation of the momentum loop functional as the trace of a path-ordered exponential,

$$W[P] = \text{tr} \left\{ \hat{T} \exp \left(i \int dP_\mu \hat{X}_\mu \right) \right\} \quad (10.21)$$

restrict the generality of the solution? If \hat{X}_μ were assumed to be finite $N \times N$ matrices, the Cayley-Hamilton theorem and finite polynomial trace identities would artificially constrain the higher-order Magnus tensors $\mathcal{W}^{(n)}$, destroying the generality of the expansion.

However, in the planar limit ($N_c \rightarrow \infty$), the Master Field operates in a strictly infinite-dimensional Hilbert space. As established by the *Master Field Theorem* proven by the author in 1994 [30, 32], any generic parametric-invariant loop functional expandable in iterated path integrals (guaranteed to be topologically complete by Chen’s theorem [35]) can be mapped exactly onto the non-commutative moment space of Free Probability and represented exactly as a Magnus-ordered exponential path integral over a non-commutative word space.

The true non-perturbative Fock space of the string endpoint is the discrete space of “words” generated by $d = 4$ Cuntz algebra operators:

$$a_\mu a_\nu^\dagger = \delta_{\mu\nu}, \quad a_\mu |0\rangle = 0 \quad (10.22)$$

In this space, the position operator \hat{X}_μ is uniquely constructed as an infinite, cascading sum of creation operators (the Voiculescu expansion [40]):

$$\hat{X}_\mu = a_\mu + \sum_{k=1}^{\infty} Q_{\mu, \mu_1 \dots \mu_k} a_{\mu_1}^\dagger \dots a_{\mu_k}^\dagger \quad (10.23)$$

By the Free Moment-Cumulant Theorem [41], this single, order-independent operator contains an infinite tower of algebraically unconstrained parameters (the free planar cumulants Q). Because the free Cuntz algebra contains no finite trace identities, our Master Field Theorem guaranties that the trace of the path-ordered exponential is mathematically unrestricted. It exhaustively spans the continuous functional space of any closed loop without truncation.

These Q tensors are related to the invariant \mathcal{W} tensors by a free cumulant expansion, uniquely solvable term by term for $Q(\mathcal{W})$, assuming the \mathcal{W} tensors are finite. Therefore, the breakdown at the eighth order is definitively not an artifact of a restrictive algebraic ansatz. Rather, this lack of a solution for $\mathcal{W}^{(8)}$ rigorously implies that the assumption of an analytic functional $W[P]$ is violated beyond the sixth order of the Magnus expansion. The physical resolution is that the true solution must be a singular functional possessing a non-local dependence on the momentum loop P .

The theory of minimal surfaces provides a precise geometric precedent for this behavior: the

Douglas functional for the area of a minimal surface bounded by a loop C [12]. As established by Douglas, the area becomes a singular functional of the loop only after it is minimized over all possible boundary parametrizations.

Before this minimization, the area is simply a quadratic Dirichlet-Hilbert functional 3.28 governed by the singular principal-value kernel \mathcal{H} . However, the strict minimization over parametrizations transforms it into a fundamentally singular functional because the optimal (isothermal) parametrization becomes implicitly and non-locally tied to the geometric shape of the loop. Any local change to the shape of the loop (for instance, tracking the normalized momentum $\hat{P}' = P' / \int |P'| d\theta$) forces a global readjustment of this parametrization. This continuous global geometric shift modifies the analytic structure (though not the position) of the pole at $\theta = \theta'$ of the Hilbert kernel on the unit circle. Such shape-dependent, non-local singularities are fundamentally incompatible with a continuous, analytic Taylor-Magnus expansion in terms of iterated path integrals.

Our exact continuum solution—the fermion determinant evaluated on the rigid Hodge-dual minimal surface—belongs precisely to this class of singular geometric functionals. The required reparametrization invariance is dynamically enforced by the null-twistor (Virasoro) constraint, which acts as the exact algebraic mechanism implementing the Douglas minimization over parametrizations. The algebraic catastrophe at $\mathcal{W}^{(8)}$ is thus the mathematical signature of the string geometry asserting its non-local rigidity and justifying the transition from a 1D algebraic Master Field to the 4D continuous geometry of the rigid twistor string.

11. The twistor parametrization of the loop space measure

The construction of the momentum loop path integral (10.3) in planar QCD begins with a linear measure (10.10) over the space of closed loops. However, after gauge fixing the reparametrization symmetry ($\text{Diff}(S^1)$) via the Virasoro constraint, the correct measure on the reduced phase space becomes nonlinear. In this section, we derive the Jacobian $J = \sqrt{\det Q}$ arising from the twistor parametrization of the metric in loop space. In addition to this determinant, there is a Faddeev-Popov Jacobian arising from the gauge condition that fixes the residual local rescaling invariance of the twistor parametrization.

11.1. Gauge Symmetry and the Need for Gauge Fixing

The linear integration measure $\mathcal{D}C$ (10.10) is redundant due to the reparametrization invariance of

the Wilson loop $W[C]$. To define the path integral rigorously, we must fix this gauge freedom and factor the measure by the volume of diffeomorphisms of the unit circle.

For the computation of the momentum loop $W[P]$, we choose the **conformal gauge**, where the loop parametrization is identified with the boundary value of a holomorphic null curve $f_\mu(z)$ in the bulk. The tangent vector of this complex curve factorizes into spinors (referred to as twistors in this context):

$$f'_\mu(z)\sigma_\mu = \lambda(z) \otimes \mu(z) \quad (11.1)$$

The physical loop $C_\mu(\theta)$ is recovered as the real part of the boundary value of $2f_\mu(e^{i\theta})$. The Virasoro constraint $(f')^2 = 0$ imposed by this ansatz does not restrict the *shape* of the loop in \mathbb{R}^4 ; rather, it fixes the parametrization to be isothermal (where $|\dot{C}| = |H[\dot{C}]|$).

The original measure $\mathcal{D}C$ is invariant under the infinite-dimensional diffeomorphism group $\text{Diff}(S^1)$. Physically, this is a redundancy: different parametrizations describe the same geometric loop. To obtain a well-defined path integral, we must factor out this gauge volume:

$$\mathcal{D}C = \mathcal{D}C_{\text{phys}} \text{Vol}(\text{Diff}(S^1)) \quad (11.2)$$

where $\mathcal{D}C_{\text{phys}}$ is the measure on the space of unparametrized loops. Imposing the Virasoro constraint is equivalent to choosing a specific gauge slice. In the twistor language, the physical degrees of freedom are encoded in the fields $(\lambda(z), \mu(z))$, modulo residual gauge symmetries.

Remark 11.1. *The scalar products between tilde spinors and spinors are defined as*

$$\tilde{\lambda}\lambda = \tilde{\lambda}_1\lambda_1 + \tilde{\lambda}_2\lambda_2; \quad (11.3)$$

$$\tilde{\mu}\mu = \tilde{\mu}_1\mu_1 + \tilde{\mu}_2\mu_2; \quad (11.4)$$

These products are $O(4)$ -invariant, unlike products

$$v_\alpha = \lambda\sigma_\alpha\mu = \sum_{a,b} \lambda_a\sigma_\alpha^{ab}\mu_b \quad (11.5)$$

which are normal matrix-spinor products and transform as four-vectors. By design, these are null-vectors

$$(v_\alpha)^2 = 0 \quad (11.6)$$

11.2. The residual $U(1)$ gauge symmetry and normalized twistors

A residual symmetry remains in the general twistor parametrization of the solution to the Virasoro constraint. The parametrization (11.1) is invariant under the gauge transformation with a complex function $u(z)$:

$$\delta\lambda(z) = u(z)\lambda(z); \quad \delta\mu(z) = -u(z)\mu(z) \quad (11.7)$$

This transformation leaves the product $\lambda \otimes \mu$ (and thus the velocity v) invariant. To fix this redundancy, we impose the normalization constraint **at the boundary**:

$$(\bar{\lambda}\lambda - \bar{\mu}\mu)_{|z|=1} = 0 \quad (11.8)$$

This constraint fixes the real part of the local rescaling (where $u(z)$ is real). Considering a variation $\delta r(z)$ corresponding to this real scaling:

$$\delta\lambda(z) = \delta r(z)\lambda(z); \quad \delta\mu(z) = -\delta r(z)\mu(z); \quad (11.9)$$

$$\delta(\bar{\lambda}\lambda - \bar{\mu}\mu) = 2\delta r(z)(\bar{\lambda}\lambda + \bar{\mu}\mu) \quad (11.10)$$

This gauge constraint requires a Faddeev-Popov Jacobian. Since the transformation is local, the Jacobian is diagonal in the position basis, leading to an extra local factor in the measure:

$$\begin{aligned} d\Omega_{FP}(\lambda, \mu) &= \mathcal{D}\lambda\mathcal{D}\mu \delta(\bar{\lambda}\lambda - \bar{\mu}\mu) \det\{(\bar{\lambda}\lambda + \bar{\mu}\mu)\} \\ &= \prod_{|z|=1} d\lambda d\mu \delta(\bar{\lambda}\lambda - \bar{\mu}\mu) (\bar{\lambda}\lambda + \bar{\mu}\mu) \end{aligned} \quad (11.11)$$

Remark 11.2. *It is important to distinguish between the bulk variables on the disk and their boundary values. Our holomorphic twistor fields $\lambda(z), \mu(z)$ are defined on the whole disk, depending on complex variable z , $|z| \leq 1$. The conjugate twistors $\bar{\lambda}(z), \bar{\mu}(z)$ depend on \bar{z} . The loop velocity $v = C'$ is the boundary value $v = 2\text{Re}\partial_\theta f(e^{i\theta})$. Thus, the integration measure covers the boundary data of the twistors, which locally parametrize the loop velocity. The bulk values are reconstructed via analyticity (Hilbert transform), so the path integral is defined strictly over the boundary measure.*

11.3. Twistor-induced metric in loop space

We treat the linear measure in loop space (10.10) as a measure in the space of velocities $v_\mu = C'_\mu$, subject to the periodicity constraint:

$$\mathcal{D}C = \delta^4\left(\oint d\theta v(\theta)\right) \prod_{\theta=0}^{2\pi} d^4v(\theta) \quad (11.12)$$

The boundary condition provides a local relation between the loop velocity and twistor boundary values

$$v_\alpha(\theta) = 2\text{Re}(iz\lambda(z)\sigma_\alpha\mu(z))_{z=e^{i\theta}} \quad (11.13)$$

This projection induces a metric on the tangent space of the twistors. The norm of a variation in loop space is:

$$\begin{aligned} \|\delta v\|^2 &= \oint d\theta (\delta v_\alpha)^2 \propto \\ &\oint d\theta |z\delta\lambda\sigma_\alpha\mu + z\lambda\sigma_\alpha\delta\mu - \text{c.c.}|^2 \end{aligned} \quad (11.14)$$

Expanding the square and using Fierz identities, this norm can be written in a quadratic form acting on the spinor variations $\delta\Lambda = (\delta\lambda, \delta\mu)^T$:

$$\|\delta v\|^2 \propto \oint d\theta \delta\Lambda^\dagger \cdot \hat{Q} \cdot \delta\Lambda \quad (11.15)$$

The kernel is the 4×4 block matrix (in spinor indices):

$$\hat{Q} = \begin{pmatrix} (\bar{\mu}\mu)\mathbb{1}_2 & \lambda\bar{\mu} \\ \mu\bar{\lambda} & (\bar{\lambda}\lambda)\mathbb{1}_2 \end{pmatrix} \quad (11.16)$$

where $\lambda\bar{\mu}$ denotes the dyadic product (rank-1 matrix). To determine the measure, we analyze the eigenvalues of \hat{Q} . Let $\Lambda = \bar{\lambda}\lambda = \bar{\mu}\mu$ on the constraint surface. The eigenvalues are:

1. $\omega_1 = 0$: The **zero mode**, corresponding to the gauge symmetry $\delta\lambda = \lambda, \delta\mu = -\mu$.
2. $\omega_2 = 2\Lambda$: The dilatation mode $\delta\lambda = \lambda, \delta\mu = \mu$.
3. $\omega_{3,4} = \Lambda$: Rotation modes orthogonal to the spinors.

The determinant of \hat{Q} vanishes due to the zero mode, which reflects the redundancy fixed by the constraint (11.8). Following the Faddeev-Popov procedure, the correct Jacobian is the square root of the determinant restricted to the physical subspace (orthogonal to the gauge orbit). This is given by the product of the non-zero eigenvalues:

$$\mathcal{D}v = \sqrt{\det\{\}'Q} d\Omega_{FP}(\lambda, \mu) \quad (11.17)$$

Evaluating the determinant on the physical subspace yields the factor:

$$\sqrt{\det\{\}'Q} = \sqrt{2\Lambda^3} \quad (11.18)$$

11.4. Normalization of the Zero Mode and the Full Measure

The Jacobian computed in (11.18), $\sqrt{\det\{\}'Q} = \sqrt{2\Lambda^3/2}$, represents the volume element of the physical configuration space (the subspace orthogonal to the gauge orbits). To obtain the correct measure for the full spinor space before dividing by the gauge volume, we must include the normalization of the zero mode itself.

The zero mode corresponds to the generator of the real rescaling symmetry. The variation along this gauge orbit is given by:

$$\delta\lambda = \delta r\lambda, \quad \delta\mu = -\delta r\mu \quad (11.19)$$

where δr is the infinitesimal parameter of the transformation. The norm of this tangent vector in the flat spinor space is:

$$\begin{aligned} \|\delta_{\text{gauge}}\|^2 &= |\delta\lambda|^2 + |\delta\mu|^2 \\ &= (\delta r)^2 \bar{\lambda}\lambda + (\delta r)^2 \bar{\mu}\mu \end{aligned} \quad (11.20)$$

Imposing the constraint $\bar{\lambda}\lambda = \bar{\mu}\mu = \Lambda$, this simplifies to:

$$\|\delta_{\text{gauge}}\|^2 = 2\Lambda(\delta r)^2 \quad (11.21)$$

Thus, the metric factor (or "length") associated with the gauge direction is:

$$\sqrt{\det G_{\parallel}} = \sqrt{2\Lambda} \quad (11.22)$$

The total measure on the spinor space is the product of the measure on the physical subspace and the measure along the gauge orbit. Combining the physical Jacobian (11.18) with the gauge normalization (11.22), we recover the full scaling factor:

$$\begin{aligned} J_{\text{total}} &= \sqrt{\det\{\}'Q} \times \sqrt{\det G_{\parallel}} \\ &= (\sqrt{2\Lambda^3/2}) \times (\sqrt{2\Lambda}) = 2\Lambda^2 \end{aligned} \quad (11.23)$$

This confirms that the effective measure element on the twistor space, prior to the Faddeev-Popov division of the gauge group volume, scales as $2\Lambda^2$. This factor will later cancel with another local scale factor coming from the momentum loop measure.

11.5. Summary and Physical Interpretation

To summarize:

- The original linear measure $\mathcal{D}C$ is overparameterized due to reparameterization invariance.
- Gauge fixing via the Virasoro constraint and twistor parametrization reduces the integration to the physical moduli space.
- The physically correct path integral measure is defined by the Faddeev-Popov Jacobian for the null twistor constraint (11.8). This ensures a unique counting of twistor states.
- Additionally, the change of variables from velocity $C'(x)$ to twistors introduces the Jacobian (11.23), representing the volume of the physical tangent space.
- While this measure covers the moduli space uniformly, there remains a local $U(1)$ gauge invariance: $(\lambda, \mu) \Rightarrow (e^{i\phi}\lambda, e^{-i\phi}\mu)$. The corresponding volume $|U(1)| = 2\pi$ will be simply factored out of the measure for the normalized spinors $\xi, \eta, \xi\xi = \bar{\eta}\eta = 1$. These spinors vary on $S^3 \times S^3$, therefore, the space becomes $S^3 \times S^3/S^1$ after this final factorization.

11.6. Local limit of $W[P]$ using effective action of *Elfin* theory

With the non-singular functional $W[P]$, we can utilize the local limit of our continuum solution. Parametrizing the loop C by twistors λ, μ , we compute the Fourier integral for $W[\hat{P}]$ (with $\hat{P} = P_\alpha \sigma_\alpha^\dagger$):

$$\begin{aligned} W[P] &= \int \mathcal{D}\lambda \mathcal{D}\mu 2\Lambda^3 \delta(\bar{\lambda}\lambda - \bar{\mu}\mu) \exp\left(-\int d^2z L(z, \bar{z})\right) \\ &\times \int d^4k \exp\left(-2i \oint d\theta \text{Im}(z\lambda(\hat{P} + \hat{k})\mu)\right)_{z=e^{i\theta}} \end{aligned} \quad (11.24)$$

where the combined measure factor $2\Lambda^2 \cdot \Lambda \sim \Lambda^3$ (depending on normalization conventions) is absorbed into the effective Lagrangian:

$$L(z, \bar{z}) = \frac{\sigma}{2} \Lambda^2 + \frac{1}{12\pi} |\partial_z (\log \Lambda)|^2 \quad (11.25)$$

The extra integration over the "zero mode" k_μ reproduces the delta function $\delta(\oint v d\theta)$ for the periodicity of the loop ($C(\infty) = C(-\infty)$ in the upper plane map). This results in a nonlinear theory involving spinor fields $\lambda(z), \mu(z)$ holomorphic inside the unit circle.

12. From null twistor to Liouville coupled to $S^1 \mapsto (S^3 \otimes S^3)$ sigma model

12.1. Polar Coordinate Parametrization of the Null Twistor Measure

Consider the twistor variables $(\lambda_\alpha, \mu^{\dot{\alpha}})$ on a unit circle $|z| = 1$, subject to the null constraint:

$$\bar{\lambda}^\alpha \lambda_\alpha = \bar{\mu}_{\dot{\alpha}} \mu^{\dot{\alpha}} \quad (12.1)$$

We parametrize the spinors in polar coordinates as:

$$\begin{aligned} \lambda_\alpha &= u \xi_\alpha, \\ \mu^{\dot{\alpha}} &= v \eta^{\dot{\alpha}} \end{aligned} \quad (12.2)$$

where $u, v \in \mathbb{R}_+$ are positive real scales, and ξ, η are normalized spinors:

$$\bar{\xi}^\alpha \xi_\alpha = \bar{\eta}_{\dot{\alpha}} \eta^{\dot{\alpha}} = 1 \quad (12.3)$$

The constraint implies $u = v$. The measure on the null twistor space in these coordinates transforms as:

$$\mathcal{D}\lambda \mathcal{D}\mu \delta(\bar{\lambda}\lambda - \bar{\mu}\mu) \propto u^5 du d\Omega_\xi d\Omega_\eta \quad (12.4)$$

where $d\Omega_\xi$ and $d\Omega_\eta$ are the Haar measures on S^3 .

There is one subtle issue left to settle. The local gauge $U(1)$ transformation (11.7) leaves the physical variables invariant. This $U(1)$ subgroup acts diagonally on the spinors and should be factored out, defining the angular manifold as the coset space:

$$\xi, \eta \in \frac{S^3 \times S^3}{U(1)}; \quad (12.5)$$

$$d\Omega_{\xi\eta} = \frac{d\Omega_\xi d\Omega_\eta}{2\pi} \quad (12.6)$$

12.2. Reduction to u, ξ, η Variables

The path integral over null twistors reduces to:

$$\begin{aligned} & \int \mathcal{D}\lambda \mathcal{D}\mu \delta(\bar{\lambda}\lambda - \bar{\mu}\mu) F(\lambda, \mu) \\ &= \int_0^\infty u^5 du \int_{(S^3 \times S^3)/U(1)} d\Omega_{\xi\eta} F(u\xi, u\eta) \end{aligned} \quad (12.7)$$

This makes explicit the separation between the radial scale u and the angular geometry.

12.3. Transformation to Liouville Field

We define the Liouville field ρ by the logarithmic map:

$$\rho = 2 \log u \quad \Rightarrow \quad u = e^{\rho/2} \quad (12.8)$$

The radial measure transforms as:

$$u^5 du = e^{5\rho/2} (e^{\rho/2} d\rho) = e^{3\rho} d\rho \quad (12.9)$$

Consequently, the path integral measure becomes:

$$\int \mathcal{D}\lambda \mathcal{D}\mu \cdots = \int_{-\infty}^{\infty} d\rho e^{3\rho} \int d\Omega_{\xi\eta} \dots \quad (12.10)$$

12.4. Phase space path integral for quark loop amplitudes

The physical amplitudes in (10.2) require one final functional integration: the path integral over the momentum field $P_\mu(\theta)$ (defined on the boundary).

The parametric invariance $\theta \rightarrow \phi\theta$ applies to the complete phase space integral. This invariance is broken only by the trace of the ordered path exponential of the Dirac operator. To restore it fully in the effective theory, we introduce an einbein $e(\theta) > 0$ multiplying the Dirac operator:

$$\begin{aligned} & \mathcal{D}e \mathcal{D}P \operatorname{tr} \mathcal{T} \exp \left(- \oint d\theta e(\theta) (i\gamma_\mu P_\mu(\theta) + m_q) \right) \\ &= \int \prod_\theta d^4 P(\theta) d e(\theta) \exp \left(- \oint d\theta e(\theta) (i\gamma P(\theta) + m_q) \right) \end{aligned} \quad (12.11)$$

While the conventional gauge choice is $e(\theta) = \text{const}$, we have already fixed the reparametrization gauge via the Virasoro constraint on the holomorphic vector $f_\mu(z)$. Since the reparametrization acts simultaneously on P and C , and we have factored out the volume of $\text{Diff}(S^1)$, there are no more gauge fixing to be done. We are left with integration over the arbitrary positive local einbein field $e(\theta)$.

This integration yields the inverse matrix structure.

$$\int_0^\infty de \exp(-ed\theta(i\gamma_\mu P_\mu + m_q)) \propto \frac{1}{(i\gamma_\mu P_\mu(\theta) + m_q)} \quad (12.12)$$

Taking the limit of zero quark mass and focusing on the local factor dependent on P , we compute the integral over the local momentum variable $q_\mu(\theta) = P_\mu(\theta)d\theta$:

$$I(\tau) = \int d^4 q \frac{\exp(iq_\alpha \tau_\alpha)}{i\gamma \cdot q} \quad (12.13)$$

where the source term is given by the twistor bilinear:

$$\tau_\alpha = \operatorname{Re}(iz\xi\sigma_\alpha\eta) e^\rho \quad (12.14)$$

This Fourier integral is calculable. Up to normalization, we obtain:

$$I(\tau) \propto \frac{i\gamma_\mu \tau_\mu}{(\tau^2)^2} \quad (12.15)$$

Using the normalization of the spinors ξ, η , and the Fiertz identity, the square of the source vector simplifies:

$$\begin{aligned} \tau^2 &= (\text{Re}(iz\xi\sigma_\alpha\eta))^2 e^{2\rho} \\ &= \frac{-1}{4} (z\xi\sigma\eta - \bar{z}\bar{\xi}\bar{\sigma}\bar{\eta})^2 e^{2\rho} = \frac{1}{4}(4)e^{2\rho} = e^{2\rho} \end{aligned} \quad (12.16)$$

Substituting this back into the result:

$$I(\tau) \propto \frac{i\gamma_\alpha \text{Re}(\xi\sigma_\alpha\eta) e^\rho}{(e^{2\rho})^2} = \exp(-3\rho) [i\gamma_\alpha \text{Im}(z\xi\sigma_\alpha\eta)] \quad (12.17)$$

Remarkably, the factor $e^{-3\rho}$ from the momentum integration exactly cancels the measure factor $e^{3\rho}$ derived from the twistor transformation, rendering the effective local volume element scale-invariant.

Remark 12.1 (Scale Invariance of the Phase Space Measure). *The exact cancelation of the Liouville factors, $e^{3\rho} \cdot e^{-3\rho} = 1$, is a necessary consequence of the symplectic geometry of the loop phase space. The canonical path integral measure $\mathcal{D}PDC$ is invariant under canonical transformations, including the scaling dilatation $C_\mu \rightarrow sC_\mu$ and $P_\mu \rightarrow s^{-1}P_\mu$. In our construction, the twistor transformation introduces a specific scaling of the coordinate velocity $v \sim e^\rho$. The Jacobian of this transformation ($e^{3\rho}$) represents the compression of the coordinate measure. However, the integration over the conjugate momentum P_μ acts as an inverse scaling operator (a Fourier transform), generating the counter-factor $e^{-3\rho}$. The resulting scale invariance of the effective volume element ensures that the theory remains conformal at the classical level, consistent with the dimensionless nature of the phase space volume element $dP \wedge dC \sim \hbar$.*

12.5. The Holographic Liouville Theory

The effective action now reduces to a Liouville-type term for the field ρ :

$$S_{\text{Liouville}} = \int d^2z \left(\frac{1}{3\pi} |\partial_z \rho|^2 + \sigma e^{2\rho} \right); \quad (12.18)$$

$$\rho(z, \bar{z}) = \frac{\log(\bar{\lambda}(\bar{z})\lambda(z)) + \log(\bar{\mu}(\bar{z})\mu(z))}{2}; \quad (12.19)$$

and the amplitude is proportional to

$$\mathcal{D}\Omega_{FP}[\lambda, \mu] \exp(-S_{\text{Liouville}}) \exp\left(-2i \sum_k q_k^\alpha \text{Im} \oint d\theta \hat{Q}_k(\theta) z \lambda \sigma_\alpha \mu\right); \quad (12.20)$$

$$Q_k(\theta) = (\Theta(\theta - \alpha_k) - \Theta(\theta - \alpha_{k+1})) \quad (12.21)$$

The closure of the loop: $\oint d\theta v_\mu = 0$ is satisfied identically in our parametrization

$$\oint d\theta z \lambda \sigma_\alpha \mu = \text{Im} \oint dz \lambda \sigma_\alpha \mu = 0 \quad (12.22)$$

This contour integral over a unit circle of a holomorphic function vanishes by the Cauchy theorem (no singularities inside the circle).

It is important to distinguish this construction from the conventional Liouville field theory encountered in 2D quantum gravity. Here, the Liouville field $\rho(z, \bar{z})$ in the bulk is not an independent fluctuating quantum field; rather, it is rigidly determined by the boundary data via the analytic continuation of the underlying holomorphic twistors $\lambda(z), \mu(z)$. Thus, this is **not** the standard dynamical Liouville theory. Instead, it represents a hidden one-dimensional theory of twistors on the boundary, disguised as a 2D Liouville theory—a simpler, albeit less familiar, mathematical object.

In our framework, the path integral measure over loop space is rigorously constructed through a systematic procedure: we begin with a linear measure, impose the Virasoro constraint via twistor parametrization, and fix the residual local scaling symmetry. The resulting measure is manifestly real and positive. Crucially, this measure does not contain an exponential of the KKS symplectic form—a hallmark of conventional string quantization and Conformal Field Theory (CFT). We emphasize that our approach does *not* involve quantizing a fundamental string in the Nambu-Goto sense, but rather constitutes a faithful implementation of the solution to the Makeenko–Migdal loop equations in momentum loop space.

12.6. Block Matrix Structure and Diagonalization via Staggered Spinors

The effective action involves the path-ordered product of the matrix-valued velocity operator along the loop. The fundamental link variable is the matrix $\mathcal{M}(x) = i \not{v}(x) = i\gamma_\alpha v_\alpha(x)$. In the chiral (Weyl) representation, the Dirac matrices have the off-diagonal structure:

$$\gamma_\alpha = \begin{pmatrix} 0 & \sigma_\alpha \\ \bar{\sigma}_\alpha & 0 \end{pmatrix} \quad (12.23)$$

where $\sigma_\alpha = (1, \vec{\sigma})$ and $\bar{\sigma}_\alpha = (1, -\vec{\sigma})$ in Euclidean signature (or σ_α are the standard Pauli matrices). The velocity vector is given explicitly by the projection of the loop momentum onto the spinor dyadics:

$$v_\alpha = iz(\xi\sigma_\alpha\eta) - i\bar{z}(\eta^\dagger\sigma_\alpha\xi) \quad (12.24)$$

Substituting this into the link matrix \mathcal{M} and using the Fierz completeness relation $(\psi^\dagger\sigma_\alpha\chi)\sigma^\alpha = 2\chi\psi^\dagger$, the operator takes the specific block form:

$$\mathcal{M} = i \begin{pmatrix} 0 & \mathcal{P} \\ \mathcal{P} & 0 \end{pmatrix} \quad (12.25)$$

where \mathcal{P} is the Hermitian operator on the 2-component spinor space, explicitly dependent on the loop coordinate $z = e^{i\theta}$:

$$\mathcal{P}(\theta) = 2i [z\eta\xi^\dagger - \bar{z}\xi\eta^\dagger]_{z=e^{i\theta}} \quad (12.26)$$

This off-diagonal structure implies a ‘‘chirality hopping’’ mechanism: the operator maps a left-handed spinor at point θ to a right-handed spinor at $\theta + d\theta$, and vice versa. To compute the trace of the ordered product efficiently, we employ a staggered spinor transformation (analogous to the Kawamoto-Smit transformation in lattice gauge theory).

We discretize the loop into $2N$ points and define a transformed spinor basis Ψ'_n related to the original basis Ψ_n by a site-dependent rotation Ω_n :

$$\Psi_n = \Omega_n \Psi'_n, \quad \Omega_n = \begin{cases} \mathbb{1}_4 & \text{for even } n \\ \gamma_0 & \text{for odd } n \end{cases} \quad (12.27)$$

where $\gamma_0 = \begin{pmatrix} 0 & \mathbb{1}_2 \\ \mathbb{1}_2 & 0 \end{pmatrix}$ is the chirality-flipping matrix. The effective link matrix between sites n and $n+1$ transforms as $\tilde{\mathcal{M}}_n = \Omega_{n+1}^\dagger \mathcal{M}_n \Omega_n$.

Due to the bipartite nature of the 1D loop, there are two alternating cases:

1. **Even to Odd** ($n \rightarrow n+1$):

$$\tilde{\mathcal{M}} = \gamma_0^\dagger (i \not{\mathcal{P}}) \mathbb{1} = \begin{pmatrix} 0 & \mathbb{1} \\ \mathbb{1} & 0 \end{pmatrix} i \begin{pmatrix} 0 & \mathcal{P} \\ \mathcal{P} & 0 \end{pmatrix} = i \begin{pmatrix} \mathcal{P} & 0 \\ 0 & \mathcal{P} \end{pmatrix} \quad (12.28)$$

2. **Odd to Even** ($n \rightarrow n+1$):

$$\tilde{\mathcal{M}} = \mathbb{1}^\dagger (i \not{\mathcal{P}}) \gamma_0 = i \begin{pmatrix} 0 & \mathcal{P} \\ \mathcal{P} & 0 \end{pmatrix} \begin{pmatrix} 0 & \mathbb{1} \\ \mathbb{1} & 0 \end{pmatrix} = i \begin{pmatrix} \mathcal{P} & 0 \\ 0 & \mathcal{P} \end{pmatrix} \quad (12.29)$$

The transformation completely diagonalizes the operator in the Dirac space, decoupling the 4-component spinor into two identical 2-component sectors.

The trace of the path-ordered product along the closed loop splits into two equal 2×2 traces:

$$T = \text{tr}_4 \prod_\theta (i \not{\mathcal{P}}(\theta)) = 2 \text{tr}_2 \prod_\theta (i \mathcal{P}(\theta)) \quad (12.30)$$

This reduction from 4×4 to 2×2 matrices significantly reduces the computational complexity for numerical evaluation. The trace of the remaining product of our projection operators is real (by the charge conjugation symmetry of Dirac traces), but it is not positive definite, and in general, it oscillates. Therefore, the Complex Langevin method [42] required to compute this path integral.

13. The Linear Regge trajectories in the WKB limit

13.1. The Helicoid Saddle Point

In the semiclassical limit (large momentum or large tension σ), the path integral is dominated

by the saddle point of the effective action. We look for a solution corresponding to a meson with large angular momentum J , which corresponds to a rotating momentum configuration.

Consider a momentum distribution rotating in the (1, 2) plane with frequency ω :

$$P_1(\tau) + iP_2(\tau) = P_0 e^{i\omega\tau}, \quad P_3 = P_4 = 0. \quad (13.1)$$

This source term in the action (11.24) drives the spinor fields. We search for a solution that respects this rotational symmetry. The natural ansatz corresponds to the **helicoid** minimal surface described in Appendix B.4.

In the spinor formalism, with rescaling $w(z) = z^{-1/2}$ the Helicoid is generated by:

$$\lambda(z) = e^{i\pi/4} \begin{pmatrix} z^{-1} \\ 1 \end{pmatrix}, \quad \mu(z) = e^{i\pi/4} \begin{pmatrix} 1 \\ -z \end{pmatrix} \quad (13.2)$$

Substituting this into the null vector definition $f'_\mu \sigma_\mu = \lambda \otimes \mu$, we find:

$$f'_1 + if'_2 \sim \frac{1}{z}, \quad f'_3 = f'_4 = 0. \quad (13.3)$$

Integrating this yields the logarithmic cut $f(z) \sim \log z$, which maps the complex plane to the infinite strip of the helicoid. The boundary value on the real axis $z = e^\tau$ gives a rotating coordinate vector, consistent with the rotating momentum source.

13.2. The Minkowski Helicoid

The Minkowski Helicoid is parameterized by time $\tau \in [0, T]$ and radius $r \in [-R, R]$, see [43]. The time T tends to infinity in the end.

$$X(\tau, r) = (r \cos \omega\tau, r \sin \omega\tau, 0, \tau) \quad (13.4)$$

The induced Minkowski metric is $g_{ab} = \text{diag}(1 - \omega^2 r^2, 1)$.

In Minkowski space we are not seeking to minimize the area in the geometric sense, as the area functional is not positive definite and the minimization problem is distinct. Instead, our criterion is algebraic: we require a solution to the Loop Equations for the Wilson loop. This demands the self-duality of the area derivative and the additivity of the area functional. We utilize the fact that the Euclidean Helicoid is a minimal surface for arbitrary angular velocity ω . We obtain the Minkowski Helicoid via a double Wick rotation:

$$x_4 \rightarrow it, \quad \omega_E \rightarrow -i\omega. \quad (13.5)$$

Under this transformation, the argument of the trigonometric functions in the coordinate parametrization becomes real ($\omega_E x_4 \rightarrow \omega t$), mapping the Euclidean Helicoid to a real surface in Minkowski space. Crucially, the condition that $S[C]$ is a zero mode of the Loop Equation depends on algebraic identities (self-duality of the area derivative and additivity). By the Identity

Theorem, these analytic relations, established for the Euclidean minimal surface, must hold for its analytic continuation into Minkowski space. Thus, the Minkowski Helicoid remains a valid solution to the QCD Loop Equation, bypassing the ill-posed variational problem of minimizing area in a space with an indefinite metric. Another important point

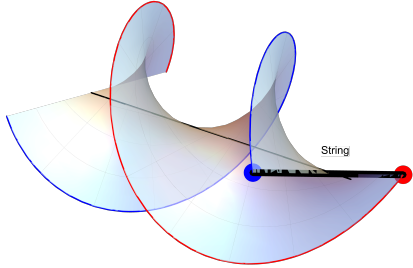


Figure 14: The helicoid spanned by rotating $\bar{q}q$ pair connected by a rigid stick (string). This minimal surface bounded by a double helix, was discovered by Meusnier in 1785.

is that the Helicoid boundary loop (double helix) is **infinitely smooth**, lacking any cusps or self-intersections. This means that no UV divergent renormalization factors could potentially affect our computation of the meson Regge trajectory.

13.3. Semiclassical Motivation: Twisted Boundary Conditions

Before solving the spectral equation, we justify the choice of the Helicoid geometry from the perspective of the semiclassical quark path integral.

Consider the Green's function for a meson composed of scalar quarks with mass m_q . In the quenched approximation, the effective Minkowski action involves a sum over quark trajectories C , weighted by the quark mass term and the area of the confining minimal surface Σ bounded by C , neglecting the perturbative factor³ This is relevant to our WKB approximation in the Wilson loop at large loops:

$$\mathcal{Z} \sim \int \mathcal{D}C \exp \left(-im_q \oint_C ds - i\sigma S_{\text{Mink}}[\Sigma_C] \right) \quad (13.6)$$

To extract the spectrum of states with angular momentum J , we impose *twisted boundary conditions*. We require the quark positions at time $t = T$ to be a rotation of their positions at $t = 0$ by an angle $\Theta = \omega T$ in the rotation plane xy :

$$(x + iy)(T) = e^{i\omega T} (x + iy)(0) \quad (13.7)$$

³the perimeter renormalization terms in that factor are included in the physical quark mass.

The angular momentum J arises as the thermodynamic conjugate to the twist frequency ω .

The ground state of this system is determined by the saddle point of the effective action. This requires the simultaneous minimization of the boundary length (quark term) and the surface area (gluon term).

- The minimization of the boundary length for a rotating particle yields a helical trajectory in Minkowski spacetime.
- The minimal surface spanning two twisted helical boundaries is the **helicoid**.

Thus, the Helicoid is not merely an ansatz; it is the unique geometric solution mandated by the kinematics of angular momentum in the semiclassical limit. The balance between the surface tension σ (pulling the quarks inward) and the centrifugal barrier (pushing the twisted trajectories outward) determines the physical radius of the meson.

13.4. Effective Lagrangean

We construct the effective Lagrangian L by combining the bulk contribution from the Helicoid area (coming from our confining factor) with the worldline terms for the massive quarks. The confining factor introduces an effective Minkowski area term. We interpret the phase factor for quark propagation as an effective action, adding the worldline terms $2m \int ds$. The total Lagrangian is:

$$L = L_{\text{helicoid}} + L_{\text{quarks}} \quad (13.8)$$

The Helicoid contribution, calculated as the area integral in Minkowski space for a ruled surface with angular velocity ω and radius $R = v/\omega$, is:

$$\begin{aligned} L_{\text{helicoid}} &= -\sigma \int_{-R}^R dr \sqrt{1 - \omega^2 r^2} \\ &= -\frac{\sigma}{\omega} \left(v \sqrt{1 - v^2} + \arcsin v \right) \end{aligned} \quad (13.9)$$

Here σ is the physical string tension, related to the parameter κ in the confining factor $\exp(-\kappa S[C])$ by the relation $\sigma = 2\sqrt{2}\kappa$, which accounts for the normalization of the Hodge-dual area functional. Adding the particle term $-2m\sqrt{1-v^2}$ as specified for the massive endpoints, the total effective Lagrangian becomes:

$$L(v, \omega) = -\frac{\sigma}{\omega} \left(v \sqrt{1 - v^2} + \arcsin v \right) - 2m_q \sqrt{1 - v^2} \quad (13.10)$$

It is worth noting that this mass term is proportional to the perimeter of the loop in Minkowski space. Therefore, the potential perturbative terms proportional to the loop perimeter are included in this physical quark mass m_q . We are assuming that this physical mass (the bare quark mass plus

perturbative corrections) adds up to a finite renormalized mass m_q , which, as the experiment tells us, is much smaller than the QCD mass scale, so that $m_q^2 \ll \kappa$.

We proceed to compute the conserved quantities via the Legendre transform. The angular momentum J is the conjugate momentum to the rotation frequency:

$$J = \frac{\partial L}{\partial \omega} \quad (13.11)$$

Taking into account that v depends on ω via the fixed radial extent ($v = \omega R$), the differentiation yields:

$$J = \frac{\sigma}{\omega^2} (\arcsin v - v \sqrt{1-v^2}) + \frac{2m_q v^2}{\omega \sqrt{1-v^2}} \quad (13.12)$$

The Energy E is defined by the Hamiltonian $E = \omega J - L$. Substituting the expressions for J and L and simplifying the algebra, we obtain:

$$E = \frac{2\sigma}{\omega} \arcsin v + \frac{2m_q}{\sqrt{1-v^2}} \quad (13.13)$$

13.5. Balance of quark forces and boundary condition

The relationship between the endpoint velocity v and the string length R is not arbitrary; it is determined by the balance of forces at the string endpoint, which depends on the quark mass m_q . We derive this boundary condition by minimizing the action with respect to the geometric radius R of the loop, keeping the angular velocity ω fixed.

Recall that the total Lagrangian L is composed of the bulk integral for the helicoid and the boundary terms for the quarks:

$$L = -2\sigma \int_0^R dr \sqrt{1 - \omega^2 r^2} - 2m_q \sqrt{1 - \omega^2 R^2} \quad (13.14)$$

The equation of motion for the endpoint radius R is given by the stationarity condition $\frac{\partial L}{\partial R} = 0$. Differentiating the integral using the Leibniz rule yields the tension force, while differentiating the boundary term yields the centrifugal force:

$$\frac{\partial L}{\partial R} = -2\sigma \sqrt{1 - \omega^2 R^2} - 2m_q \frac{d}{dR} \left(\sqrt{1 - \omega^2 R^2} \right) = 0 \quad (13.15)$$

Substituting $v = \omega R$ and computing the derivative of the mass term:

$$-2\sigma \sqrt{1 - v^2} - 2m_q \left(\frac{-\omega^2 R}{\sqrt{1 - \omega^2 R^2}} \right) = 0 \quad (13.16)$$

Simplifying the expression, we obtain the exact force balance equation for finite mass:

$$\sigma \sqrt{1 - v^2} = \frac{m_q v^2}{R \sqrt{1 - v^2}} \implies v^2 = \frac{\sigma R}{\sigma R + m_q} \quad (13.17)$$

This equation balances the confining string tension (LHS) against the relativistic centrifugal inertia of the quark (RHS).

We now consider the limit $m_q \rightarrow 0$, and we find the boundary condition

$$v^2 \rightarrow 1 \quad (13.18)$$

Thus, as the quark mass tends to zero, the endpoint velocity v must approach the speed of light ($v \rightarrow 1$).

These equations provide the exact parametric equation for the energy of the classical pair of particles with a given angular momentum and a given radius R . To recover the Regge trajectories, we consider the limit of massless quarks ($m_q \rightarrow 0$), where the endpoint velocity approaches the speed of light ($v \rightarrow 1$). In this limit, the mass terms vanish, and the system is governed purely by the confining geometry:

$$E \approx \frac{2\sigma}{\omega} \frac{\pi}{2}, \quad J \approx \frac{\sigma}{\omega^2} \frac{\pi}{2} \quad (13.19)$$

Eliminating ω between these two relations:

$$J = \frac{\sigma(\pi/2)}{(\pi\sigma/E)^2} \cdot \frac{\pi}{2} \implies J = \frac{E^2}{2\pi\sigma} \quad (13.20)$$

We thus recover the linear Regge trajectory:

$$E^2 = 2\pi\sigma J \quad (13.21)$$

This result confirms that the linear confinement arises directly from the kinematics of the Hodge-dual minimal surface in Minkowski space, without invoking independent string vibrations or ad-hoc constants.

14. Twistor Holography and the Rigid Twistor String

14.1. Twistor Holography (Gauge Holography)

In our framework, **twistor holography** refers to the geometric duality in which the solution to the Makeenko–Migdal loop equation is realized as a rigid, Hodge-dual minimal surface embedded in flat $\mathbb{R}^3 \times \mathbb{R}^4$ (or, more generally, a flat 12-dimensional space). This surface is uniquely determined by the boundary Wilson loop and does not fluctuate quantum mechanically. The holographic principle here projects the internal geometry of the 12D target space onto the observable boundary, with the physical Wilson loop acting as the gauge-invariant observable. Unlike AdS/CFT gravity holography, this construction is entirely geometric and does not involve a gravitational bulk or fluctuating world-sheet metrics.

14.2. Analytic Twistor String vs. Topological Twistor String

The use of spinor variables and null twistors in this framework is closely related to the Penrose

transform, which encodes solutions to spacetime field equations in terms of cohomological data on twistor space. By imposing the specific gauge condition on boundary values of twistor map: $\bar{\lambda}\lambda = \bar{\mu}\mu$, we reduce the theory to a Liouville field interacting with a one-dimensional sigma model on $S^3 \times S^3/S^1$ on the boundary. The bulk values of the Liouville field depend on the twistor map. This parametrization makes the structure transparent: the minimal surface in the bulk is entirely encoded by the holomorphic data (the twistors), while the physical observables are determined by the boundary curve.

A crucial distinction must be made regarding the nature of the resulting bulk action. In the context of **Witten's celebrated Twistor String theory** (and related formulations such as the Berkovits model), the extension of boundary fields into the bulk typically generates a Wess-Zumino-Witten (WZW) term. The WZW functional is topological: it measures a winding number and is invariant under smooth deformations of the extension inside the disk.

In contrast, our bulk functional is *not* topological. While it is determined by the boundary data, its value depends explicitly on the unique analytic continuation of the holomorphic twistors into the disk. In this sense, our framework is closer in spirit to Penrose's **Non-Linear Graviton** construction than to topological string theory. In the Non-Linear Graviton, the curved geometry of the bulk spacetime is encoded by the global complex structure of twistor space, which arises as the unique holomorphic extension compatible with boundary (patching) data. Similarly, our action represents the geometric energy (akin to a Kähler potential) of the specific holomorphic disk filling the boundary loop. This non-topological dependence is essential: it encodes the geometric rigidity of the minimal surface, leading to the emergence of the area law and confinement in the rigid twistor string.

The general issues of the discretization of our theory and its direct numerical simulation (DNS) are discussed in [Appendix D](#), where we present formulas and algorithms for the analytic extension of holomorphic twistor fields from a discrete set of boundary values. We attempted the direct numerical simulation of this path integral with oscillating weight using the Complex Langevin equation (CLE) on [Appendix E](#). The results are encouraging but not convincing; perhaps some additional numerical algorithms are needed to overcome the instabilities of the CLE and obtain reliable results.

15. Numerical Simulation of Confining String spectrum

The analytic twistor-string formulation of the previous sections reduces the meson spectroscopy problem to the analytic structure of the quark two-point amplitude $\Pi(E)$ (after analytic continuation to Minkowski energy E). Since the corresponding boundary-twistor path integral is *not* localized, the evaluation of the spectrum becomes primarily computational. In this section, we summarize the numerical strategy and present preliminary proof-of-concept results. Full implementation details, discretization formulas, drift terms, and numerical diagnostics are given in [Appendix E](#).

Spectral observables and mass extraction

The physical quark two-point amplitude $\Pi(E)$ is a meromorphic function of the energy, characterized by physical poles at the bound-state meson masses. However, directly searching for vertical asymptotes (poles) in a stochastic Monte Carlo simulation is a numerical trap: statistical variance near a singularity diverges uncontrollably, producing massive fat-tail excursions and destroying the Complex Langevin evolution.

To completely bypass this fatal instability, we apply an analytic transformation that converts the dangerous meromorphic observable into a perfectly bounded, smooth entire function. Rather than evaluating $\Pi(E)$ directly, we consider the logarithmic derivative

$$R(E) = \frac{\Pi'(E)}{\Pi(E)}, \quad (15.1)$$

and reconstruct the spectrum from the zero-crossings of its exact inverse, $1/R(E)$.

This inversion maps vertical asymptotes into well-behaved roots. Near a physical mass pole, $\Pi(E) \sim (E - m_n)^{-1}$, the inverse resolvent becomes $1/R(E) \sim m_n - E$. The singularity is mathematically flattened into a smooth zero-crossing with a strictly negative slope. Conversely, near an artifact zero of the vacuum polarization ($\Pi(E) \sim E - E_0$), one obtains $1/R(E) \sim E - E_0$, yielding a zero-crossing with a strictly positive slope.

Because $1/R(E)$ is an entire function with no singularities anywhere in the complex plane (as detailed in [Appendix D.7](#)), the Complex Langevin process can sample it safely. Therefore, the $\bar{q}q$ masses are unambiguously identified as the zero-crossings of $\text{Re}[1/R(E)]$ possessing a negative slope. Furthermore, because the true physical signal is bounded, we know *a priori* that any massive spikes in our simulation data are purely statistical fat-tail excursions, rigorously justifying aggressive outlier filtering (such as median pooling) without fear of clipping physical resonances.

Reweighted Complex Langevin strategy (summary)

The effective twistor-string functional integral has an oscillatory weight; at present, Complex Langevin evolution (CLE) provides a practical route to evaluating it. A key technical point is that pole-finding is numerically unstable in a stochastic computation. We convert the problem into a robust *zero-finding* problem by a reweighted formulation, summarized here and derived in Appendix D.

Let S_{eff} denote the effective action for the discretized boundary-twistor variables at fixed E , and define the energy-derivative observable

$$O \equiv \frac{\partial S_{\text{eff}}}{\partial E}. \quad (15.2)$$

Then one has the exact identity

$$\frac{1}{R(E)} = \frac{\Pi(E)}{\Pi'(E)} = \frac{\int \exp(S_{\text{eff}})}{\int O \exp(S_{\text{eff}})}. \quad (15.3)$$

Introducing the modified (reweighted) action

$$\tilde{S} = S_{\text{eff}} + \log O, \quad (15.4)$$

this becomes

$$\frac{1}{R(E)} = \left\langle \frac{1}{O} \right\rangle_{\tilde{S}}. \quad (15.5)$$

Thus, the numerical pipeline is: scan E , evolve CLE with drift derived from \tilde{S} , measure $\text{Re} \left\langle \frac{1}{O} \right\rangle_{\tilde{S}}$, and locate its zero-crossings, selecting those with negative slope. In practice, the same reweighting also improves the dynamical stability of the CLE evolution by adding a logarithmic drift term; the explicit drift equations and constraint implementation are given in [Appendix E](#).

Topological stabilization and non-compact excursions

There is a deep geometric reason for this stabilization, naturally understood through the lens of Picard-Lefschetz theory, introduced in QFT by Witten [44], and successfully used in recent QCD simulations [45, 46]. In the complexified phase space, the exact path integral is formally defined on a middle-dimensional integration contour composed of steepest descent manifolds (Lefschetz thimbles). While the deterministic drift of the Complex Langevin Equation naturally targets these thimbles, stochastic noise inevitably kicks the trajectory off these stable manifolds and into adjacent ‘‘Stokes wedges,’’ where the action diverges and the Markov chain suffers runaway excursions.

To counteract this, modern lattice simulations typically rely on computationally expensive algorithmic interventions. As detailed in the review [46], standard approaches involve explicitly deforming the integration contour via holomorphic gradient flow (which incurs a prohibitive $\mathcal{O}(V^3)$ Jacobian

cost), utilizing machine-learning-optimized manifolds, or applying ad-hoc dynamic stabilization and gauge cooling to actively force the system to remain near the thimbles.

Our logarithmic reweighting, however, achieves this stabilization natively for the observable. By shifting the effective action ($\tilde{S} = S_{\text{eff}} + \log \mathcal{O}$), we fundamentally alter the topology of the complexified phase space. The associated CLE drift force acquires essential meromorphic poles exactly at the zero-locus of the observable ($\mathcal{O} = 0$):

$$-\nabla \tilde{S} = -\nabla S_{\text{eff}} - \frac{\nabla \mathcal{O}}{\mathcal{O}} \quad (15.6)$$

Crucially, in the Picard-Lefschetz framework, steepest descent flows cannot cross meromorphic poles. By explicitly injecting these poles into the drift dynamics, we puncture the complex manifold. The singular repulsive force acts as an absolute topological obstacle that dynamically corrals the stochastic Markov chain. It safely traps the trajectory within the basin of the physical thimbles and mathematically forbids it from escaping into the runaway regions of the complex plane associated with the zeros of \mathcal{O} . This organically enforces dynamic stabilization without the need for computationally devastating Jacobian evaluations.

The intermittent excursions that do occur in our simulation are not numerical instabilities, but rather the exact analytic consequence of the complexified noise exploring the vicinity of this meromorphic pole. As shown in the smooth histogram of the micro-states (see [Figure E.18](#)), the probability density perfectly matches the analytically predicted $1/|u|^3$ power-law fat tails (derived in detail in [Appendix D](#)). This exact geometric matching confirms that the finite-sample Cauchy Principal Value is perfectly stable, and that the CLE is genuinely exploring the correct complexified geometry dictated by the topological barrier.

However, it is vital to recognize that this barrier only protects against excursions towards $\mathcal{O} = 0$. The complexified phase space possesses other potentially dangerous directions, most notably the non-compact flat directions corresponding to the large-volume limit of the minimal surface. Specifically, if the real part of the Liouville field grows large ($\text{Re} \rho \rightarrow \infty$), the induced worldsheet metric $e^{2\rho}$ diverges. In the complexified dynamics, the restoring force from the area term can acquire an imaginary phase, converting the confining potential into a runaway channel.

To prevent the system from exploring these unphysical infinite-volume regimes, we currently impose explicit numerical clipping (hard bounding walls) on the twistor variables. While this pragmatic regularization successfully bounds the metric, there is no *a priori* mathematical guaranty that the CLE trajectory will not systematically drift

outward and continuously collide with these artificial walls, which would artificially truncate the sampled distribution.

Remark 15.1. *It should be noted that the use of explicit numerical clipping (hard bounding walls) to tame the non-compact Liouville directions technically violates the strict holomorphy required for the formal proof of correctness of the Complex Langevin Equation, as it introduces non-analytic boundaries into the Fokker–Planck evolution. A theoretically cleaner approach would involve introducing a globally holomorphic confining potential to the effective action that generates a smooth restoring force. For example, one could augment the action to produce a holomorphic drift force such as $K_{wall} \propto -\tanh(c(\rho - \rho_{max}))$. Because the hyperbolic tangent is a meromorphic function of the complex variable ρ , this force smoothly pushes the trajectory back toward the physical region $\text{Re}(\rho) < \rho_{max}$ at large distances without breaking the analyticity of the Langevin evolution. Implementing such holomorphic barriers represents a natural analytical refinement for future high-precision simulations, safely taming the infinite-volume runaway channels while preserving the exact geometric justification of the CLE.*

To explicitly defend our simulation against accidental discrete jumps over the topological barriers, we replaced the naive Euler integration with a second-order Stochastic Heun (predictor-corrector) SDE solver. Furthermore, we implemented an adaptive time-step algorithm designed to dynamically brake the CLE evolution upon approaching singular regions. Together, these algorithmic safeguards yield highly stable trajectories that remain predominantly confined to the physical integration cycles (Lefschetz thimbles), consistently producing finite expectation values with rigorously controlled absolute errors.

Fortunately, we possess a direct empirical diagnostic to monitor whether fatal non-compact excursions occur. Because the boundary observable \mathcal{O} is composed of twistor bilinears ($\lambda \otimes \mu \sim e^\rho$), a runaway excursion towards infinite Liouville volume ($e^{2\rho} \rightarrow \infty$) would correspond to the twistor variables growing unbounded. This would drive $\mathcal{O} \rightarrow \infty$, and consequently force our measured inverse resolvent $\text{Re}[1/R(E)] = \text{Re}\langle 1/\mathcal{O} \rangle_{\bar{\xi}}$ to continuously plunge to zero. As illustrated in the raw CLE history (see Figure E.16), this catastrophic collapse explicitly does not happen. Following the initial thermalization (burn-in) phase, the trajectory does not plunge to zero, nor does it become permanently pinned against the artificial clipping boundaries. Instead, it exhibits stable, bounded macroscopic oscillations around a finite, non-zero physical mean. This empirical behavior strongly confirms that the

simulation has successfully converged to the basin of a stable Lefschetz thimble, guided by the physical gradients rather than being permanently pinned against the artificial walls. Fully taming these non-compact Liouville directions analytically—perhaps through exact coordinate transformations mapping the moduli to a compact domain—remains an important open challenge for future high-precision extensions of this framework.

Discretization and parallel ensemble

We discretize the boundary circle by a spectral grid (angular nodes) and evaluate the bulk (holomorphic) Liouville contribution by Gauss–Legendre radial quadrature, leading to a finite-dimensional holomorphic system for the complexified boundary variables evolved by CLE. To reduce sensitivity to non-Gaussian (fat-tailed) fluctuations and to monitor reproducibility, we run an ensemble of independent replicas on the Typhon cluster. In the current production setting, we use **64 nodes** (independent seeds) per energy value and pool the results across nodes using robust estimators (median central value and absolute-deviation-based error estimates). The precise implementation and diagnostics are documented in Appendix D.

16. Topological Decomposition of the Meson Spectrum via Information Clustering

16.1. Lefschetz Thimbles and Multiple Spectral Branches

In the planar limit, the exact solution of the Makeenko–Migdal loop equation involves evaluating a path integral over a highly complex configuration space. The effective action landscape of this theory is not dominated by a single, featureless ground state, but rather by a multitude of complex saddle points, or Lefschetz thimbles. Physically, these distinct topological sectors correspond to the multiple branches of the meson spectrum. In our numerical approach, we explore this landscape using stochastic Langevin dynamics. Because each independent simulation is initialized from a completely random configuration, the system naturally falls into the basin of attraction of one of these specific thimbles as it relaxes.

16.2. Topological Trapping and the Failure of Naive Pooling

Due to the presence of immense topological (or simply numerical) action barriers in the complexified space, a given simulation history generally remains confined to its respective thimble for the duration of the run. This dynamical trapping has profound implications for data analysis. If one were to follow standard numerical practice and naively

pool all independent stochastic histories at a given energy E to compute a global ensemble average, the procedure would physically mix distinct topological sectors. Consequently, this blind averaging does not yield a single, smooth resolvent curve for $1/\mathcal{R}(E)$; rather, it produces a chaotic, smeared superposition of states. The raw numerical data are actually a collection of distinct histories confined to various thimbles, each tracing out its own unbroken $1/\mathcal{R}(E)$ curve separated by topological barriers.

16.3. Phase-Information as a Topological Fingerprint

To extract the true physical spectrum, we must mathematically untangle these mixed histories and group them by the specific saddle point they occupy. As established in our analysis of the Complex Langevin dynamics in [Appendix E](#), the Cartesian observables $\text{Re}[1/\mathcal{O}]$ and $\text{Im}[1/\mathcal{O}]$ suffer from severe infinite-variance Cauchy tails ($1/|u|^3$), which generate massive radial excursions. Consequently, attempting to compare the Cartesian coordinates forces one to arbitrarily trim and shift the central moments to prevent the variance from dominating the signal.

We can completely bypass this pathological radial variance by projecting the data onto the complex phase angle $\alpha = \arg(\mathcal{O})$. This maps the entire complexified phase space onto a finite, compact support $[-\pi, \pi]$, safely absorbing infinite radial fluctuations without discarding a single data point. The probability density function of this phase angle is intrinsically scale-invariant and serves as an exact, bounded topological fingerprint of the underlying Lefschetz thimble. To compare these fingerprints, we compute the symmetric Kullback–Leibler (KL) divergence (the Jensen–Shannon distance) between their finite-support phase distributions. This strict information-theoretic metric allows us to rigorously identify pairs of histories with identical quantum geometries, entirely independent of their macroscopic radial drift.

16.4. Isolating True Mass Poles

This phase-matching provides a precise, unsupervised mechanism for identifying true meson masses. A physical mass corresponds to a strictly downward zero-crossing of the resolvent, where the sequence transitions from $\text{Re}[1/\mathcal{R}(E_i)] > 0$ to $\text{Re}[1/\mathcal{R}(E_{i+1})] < 0$. By examining pairs of runs at neighboring energy points that bracket the zero axis and demanding that they possess the absolute minimum symmetric KL distance between their phase distributions, we effectively filter out random topological jumps and numerical noise. This strict requirement of phase-geometry invariance unequivocally identifies the true crossing of the $1/\mathcal{R}(E)$ curve for a particular topological branch.

16.5. Reconstructing the Spectrum via Minimax Clustering

Having isolated a pool of high-confidence zero-crossings, we reconstruct the global spectrum of the different branches. To achieve this, we cluster the crossing events based on a strict minimax distance criterion. The topological distance between any two distinct crossing events—say, a pair (A, B) and a pair (C, D) —is defined as the maximum of all four cross-comparisons:

$$\Delta = \max(d_{JS}(A, C), d_{JS}(A, D), d_{JS}(B, C), d_{JS}(B, D)) \quad (16.1)$$

where d_{JS} is the symmetric Kullback–Leibler distance (Jensen–Shannon divergence) between the phase distributions. This mathematically merciless constraint guarantees that a pole is only clustered into a specific sequence if the quantum phase geometry, both before and after the crossing, is practically identical to the rest of the cluster.

16.6. First results of numerical solution of CLE

The CLE was coded into a *Mathematica*® package, tested on the laptop and desktop computers, and then run on the Typhon IAS cluster for 48 hours on 64 nodes in parallel, with 24 kernels working in parallel on each node. The code and the results are published on Wolfram cloud, and results are stored on the authors’ Google Drive with open access (see references in the Data section in the end of this paper). Using these *Mathematica*® files, one can verify and reproduce our results at a larger scale with higher precision.

Here is the summary of the results (all technical details are described in [Appendix E](#)).

This unsupervised information-clustering natively reconstructs the spectrum into distinct branches, mapping out different Regge trajectories. Crucially, these trajectories are strictly labeled by an internal quantum number inherent to the Twistor String path integral complex saddle points, serving as a replacement for the “daughter trajectories” of string models.

Remark 16.1. *Note that all the usual quantum numbers are identical for these two branches: this is a scalar $\bar{q}q$ channel, no spin, no flavor quantum numbers specified. In the future, more detailed simulations, spin, parity, and flavor $SU(3)$ representation will be specified, but this internal quantum number will exist on top of other quantum numbers, in the same way as internal excitations of the string (vibrational modes) lead to daughter trajectories after quantization.*

Applying this algorithm to our unvarnished stochastic phase data successfully isolated two continuous principal Regge trajectories spanning 14 and 15 consecutive negative crossings. The negative crossing of zero between two consecutive points

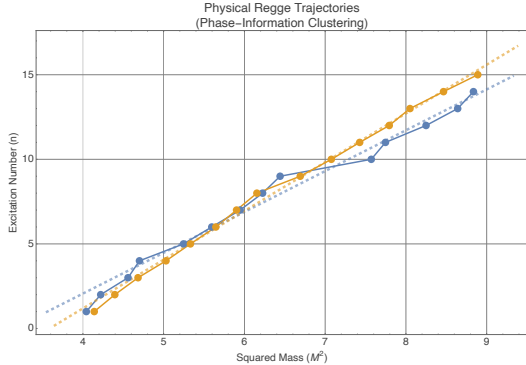


Figure 15: Plot of n vs m_n^2 (in units of the string tension σ) as a result of Complex Langevin Simulation of quark two point function in the Geometric QCD Theory. These two Regge trajectories were identified by information clustering of phase distributions of $1/O$ for 240 different energy points between 2. and 3. on 64 independent CLE simulations with different initial values. The optimal clustering identified a pair of Regge trajectories in this interval of m^2

of energy on a grid was identified with accuracy $\Delta E = \pm 1/480 \approx \pm 0.002$. Both branches exhibit non-linearity at low energies—reflecting the complex boundary dynamics and mass gaps of the true physical ground state—before transitioning into linear Regge trajectories at higher mass squared. By relying purely on the phase-information geometry, this topological extraction is designed to reveal the true spectrum of Planar QCD.

Figure 15 shows preliminary cluster-scale results for the extracted trajectory n vs. m_n^2 . These plots are intended as a proof of concept: the crossings of zero were selected by information clustering of the phase distributions we described above. The precision of higher excitations and the control of systematic effects (step size, resolution, and CLE correctness diagnostics) will be improved in larger-scale runs; the present computation establishes feasibility and provides a concrete computational pipeline for continuum planar-QCD spectroscopy in this framework.

17. The Catastrophe Theory and the Geometric Mass Spectrum

17.1. Geometric Quantization via Degenerate Lefschetz Thimbles

While the Complex Langevin Equation provides a robust numerical method to evaluate the twistor-string path integral, the holomorphic nature of the effective action reveals a profound mathematical pathway to compute the exact meson spectrum analytically, entirely bypassing stochastic simulation. This approach relies on the asymptotic evaluation of multiple complex integrals via Picard-Lefschetz theory and the singularity theory of differentiable maps.

Consider the original, un-reweighted path integral for the quark two-point amplitude $\Pi(E)$ as a function of the Minkowski energy parameter E :

$$\Pi(E) = \int_{\Gamma} \mathcal{D}\Phi_{|z|=1} \exp(E\mathcal{O}(\Phi) - S_{eff}(\Phi)) \quad (17.1)$$

where $\Phi_{|z|=1} = \{z_2, \{\rho, \xi, \eta, \bar{\xi}, \bar{\eta}, \gamma, \bar{\gamma}\}_k\}$ encompasses the boundary twistor variables extended analytically into the complexified phase space $\Phi = (\lambda(z), \mu(z))$, and Γ is the middle-dimensional integration cycle (the principal Lefschetz thimble) bounding the physical vacuum.

In the semiclassical (WKB) limit, this integral is dominated by the saddle points $\Phi_*(E)$ satisfying the classical boundary equations of motion:

$$\nabla S_{eff}(\Phi_*) - E\nabla\mathcal{O}(\Phi_*) = 0 \quad (17.2)$$

(which, as shown in Section 13, yields the rigid Helicoid geometry in the special case of twisted boundary conditions with large angular momentum J). The Gaussian fluctuations around this saddle point yield an amplitude proportional to the inverse square root of the complex Hessian determinant:

$$\Pi(E) \propto \frac{\exp(E\mathcal{O}(\Phi_*) - S_{eff}(\Phi_*))}{\sqrt{\det \mathcal{H}(E)}} \quad (17.3)$$

where the fluctuation operator is $\mathcal{H}(E) = \nabla^2 S_{eff}(\Phi_*) - E\nabla^2\mathcal{O}(\Phi_*)$.

As the continuous energy parameter E is varied, the saddle points drift through the complexified phase space. Physical bound states (mesons) correspond to macroscopic divergences in this amplitude. Mathematically, these occur at critical energies $E = E_n$ where the saddle point becomes strictly *shallow* or *degenerate* (a non-Morse critical point). At these bifurcation points, the classical stability matrix develops a null space, and the determinant of the Hessian exactly vanishes: $\det \mathcal{H}(E_n) = 0$. At this point, the WKB approximation becomes exact, as it dominates the divergent term in the path integral. According to the classification of singular integrals in Catastrophe Theory [47], the nature of the resulting divergence depends strictly on the *corank* of the singularity (the number of simultaneously vanishing eigenvalues). If only a single real eigenvalue vanishes (corank 1), the local action along the flat direction scales as ϵx^2 (with $\epsilon \propto E_n - E$). The integration over this 1D valley yields:

$$\int dx e^{-\epsilon x^2} \propto \frac{1}{\sqrt{\epsilon}} \propto \frac{1}{\sqrt{E_n - E}} \quad (17.4)$$

Physically, a square-root singularity corresponds to a branch cut, generating a multi-particle continuum threshold, not a bound state.

However, our twistor-string geometry orchestrates a remarkable mathematical conspiracy. Because the integration variables Φ are coupled *complex* holomorphic twistors, $\mathcal{H}(E)$ is a complex operator. The vanishing of a single complex eigenvalue

intrinsically mandates the simultaneous flattening of exactly *two* real directions on the Lefschetz thimble (a strict corank-2 degeneracy).

This alters the local topology of the steepest descent path. The Gaussian integral over this 2D flat valley yields:

$$\iint dx dy \exp(-\epsilon(x^2 + y^2)) \propto \frac{1}{\epsilon} \propto \frac{1}{E_n - E} \quad (17.5)$$

However, the *existence of a pole in $\Pi(E)$* requires more than $\det H(E_n) = 0$: the integration cycle must become non-compact (or be pinched) at $E = E_n$ so that the Gaussian valley is not capped by higher-order terms of $\text{Re } \mathcal{A}$. Equivalently, E_n must lie on a Stokes/Landau locus where the Lefschetz decomposition changes and the relevant thimble develops an infinitely long end. In our framework, this pinch/non-compactness is supplied dynamically by the Liouville zero-mode stretching of the worldsheet (cylinder degeneration), so that the corank-2 degeneracy is promoted to an actual simple pole of the physical amplitude.

Remark 17.1. Corank-2 from a single complex zero mode, and the pinch condition.

Let $\Phi \in \mathbb{C}^N$ denote the complexified boundary-twistor variables and $\mathcal{A}(\Phi; E) := S_{\text{eff}}(\Phi) - E \mathcal{O}(\Phi)$ the holomorphic phase. Near a critical point $\Phi_*(E)$ satisfying (17.2), the quadratic fluctuation form is governed by the complex symmetric Hessian $H(E) = \nabla^2 \mathcal{A}(\Phi; E)$. If a single complex eigenvalue $\lambda(E)$ of $H(E)$ vanishes at $E = E_n$, then locally the corresponding fluctuation coordinate is a complex mode $z = x + iy$ with $(x, y) \in \mathbb{R}^2$ on the real middle-dimensional thimble. On the steepest-descent cycle (constant $\text{Im } \mathcal{A}$), the quadratic form reduces, after an $SO(2)$ rotation in the (x, y) plane, to a positive Gaussian weight

$$\text{Re}(\delta^2 \mathcal{A}) \simeq \epsilon(x^2 + y^2) + \dots, \quad \epsilon \propto (E_n - E), \quad (17.6)$$

so that the vanishing of one complex eigenvalue generically flattens two real directions on the thimble (corank = 2) and produces the pole-like local scaling (17.5). In this sense, a “single complex zero mode” is already a corank-2 degeneracy of the real thimble geometry.

Thus, the complex holomorphic geometry natively upgrades the standard square-root branch cut into a strictly simple pole. This rigorously explains how the degenerate saddle points of the Twistor String path integral explicitly generate the discrete mass poles of the meson spectrum. (For this pole to manifest macroscopically without being capped by higher-order terms, the steepest descent contour must become infinitely long. In the framework of Landau pinch singularities [48], this infinite integration volume is provided dynamically by the Liouville zero-mode stretching the string worldsheet into an infinite cylinder).

Consequently, the extraction of the exact Planar QCD meson spectrum is formally reduced from a stochastic path integral to a deterministic Generalized Eigenvalue Problem (akin to the Gutzwiller trace formula [49] and the Dashen-Hasslacher-Neveu soliton quantization [50]). The physical masses E_n are precisely the discrete values for which the classical stability matrix develops a complex null space:

$$\det_{\mathbb{C}} \left[\nabla^2 S_{\text{eff}}(\Phi_*) - E_n \nabla^2 \mathcal{O}(\Phi_*) \right] = 0 \quad (17.7)$$

Solving this boundary-twistor Fredholm equation in general case provides a direct analytical roadmap for the exact, noise-free computation of the geometric spectrum in future work.

17.2. Catastrophes, flat valleys, and topological barriers

In the general theory of functional integration, hadronic resonances emerge when complex saddle points of the effective action become degenerate. A vanishing Hessian matrix indicates a local flat valley in the functional landscape, which is the hallmark of Catastrophe Theory. However, a local flat valley alone is fundamentally insufficient to produce a true S -matrix bound state pole. A generic Taylor expansion of the action around a degenerate saddle point will eventually be capped by higher-order terms (e.g., cubic or quartic corrections). These terms force the steepest descent contour to curve upwards, trapping the integral and yielding finite fractional powers or branch cuts rather than macroscopic divergences.

To dynamically generate an exact simple mass pole $\propto 1/(E_n - E)$, the steepest descent trajectory must correspond to a non-compact flat zero-mode that extends infinitely far in configuration space without ever curving upwards. All higher-order corrections along this specific trajectory must identically vanish, which is a known localization phenomenon in the WKB approximation for path integrals [11].

In our twistor string framework, this exact infinite flat valley is provided dynamically by the multi-valued monodromy of the holomorphic twistor fields. The zero-mode trajectory in functional space corresponds to the topological winding of the boundary parameter as it wraps around the enclosed twistor poles. Because each winding around the complex pole maps holographically to a uniform translation in target-space Minkowski time, the effective action accumulates strictly additively. The total action is exactly linear in the winding number N , which serves as the non-compact integration variable along the steepest descent path. Consequently, all higher-order nonlinear corrections for this particular field are strictly absent. The contour along this monodromy direction remains perfectly

flat as $N \rightarrow \infty$, allowing the integral to diverge into the exact geometric series that analytically generates the simple meson pole.

Furthermore, this geometric mechanism reveals that the number of twistor poles enclosed within the unit circle ($|z_k| < 1$) serves as a strict topological quantum number that classifies the resonance states.

The integrity of this integer quantum number is rigorously protected by an infinite topological action barrier. One might intuitively ask whether continuous fluctuations could cause twistor poles to smoothly drift across the unit circle boundary ($|z| = 1$), thereby changing the topological sector. However, the holomorphic boundary geometry explicitly forbids this. If a pole z_0 attempts to cross the unit circle from the inside ($|z_0| \rightarrow 1$), its conjugate mirror located at $1/\bar{z}_0$ must simultaneously approach the boundary from the outside. Exactly at the moment of crossing, these two singularities inevitably collide directly on the physical integration contour $|z| = 1$.

This collision creates a classic pinch singularity. The integration loop becomes trapped between the colliding poles z_0 and $1/\bar{z}_0$ and cannot be deformed to avoid them. Consequently, the action strictly diverges at the boundary, creating an impenetrable topological barrier. The twistor path integral is therefore dynamically locked into a fixed topological sector, mathematically guaranteeing that the number of enclosed poles is a rigorously conserved topological quantum number.

17.3. Poles inside the disk and the monodromies

We are looking for a saddle point with a single pole located at a complex coordinate z_0 strictly inside the unit disk ($|z_0| < 1$). Why inside? Because in this case, there is a non-trivial winding number. As the target space surface X winds up in the time direction, it means the quark goes around the loop infinitely many times, creating a bound state of a rotating string. This infinite motion is precisely the saddle point we are looking for—it will create the resonance pole through a geometric series over the multiple windings.

The total effective action evaluated over these multiple windings consists of two parts. First, the Liouville bulk action is simply additive because its Lagrangian density is a single-valued, explicitly periodic function of the angle on the boundary circle. Therefore, for k windings, its contribution simply duplicates: $S_{bulk}^{(k)} = kS_{bulk}^{(1)}$. Second, the boundary energy term in the effective action involves a logarithmic primitive. Because the pole z_0 is enclosed by the contour, analytic continuation around the loop causes this term to pick up a strict topological phase shift at every extra cycle. This is the nontrivial monodromy of the effective action.

Together, these terms lead to an infinite sum over the winding number k of the form $\sum \exp(ik\Delta S_{\text{eff}})$. This infinite geometric series is a direct manifestation of the flat valley near the degenerate fixed point. The valley is flat near the energy pole because the monodromy of the effective action ΔS_{eff} approaches $2\pi n$. This makes $\exp(i\Delta S_{\text{eff}}) = 1$, which leaves the amplitude invariant under winding, so that the sum over windings macroscopically diverges as $\sim 1/(1 - \exp(i\Delta S_{\text{eff}})) \sim 1/(E - E_n)$.

17.4. One pole and its symmetries

To construct the exact saddle point in the one-pole sector, we leverage the unbroken symmetries of the system. First, we fix the external kinematics by moving to the rest frame of the meson, orienting the injected momentum as $q = (0, 0, 0, iE)$. While this specific frame choice explicitly breaks the full Lorentz group, the $O(3)$ spatial rotational symmetry remains intact.

We may utilize this unbroken space rotation to align the twistor dynamics. Specifically, we can always choose a spatial frame such that the symmetric bilinear combination vanishes:

$$\lambda^T \sigma_1 \mu = 0 \quad (17.8)$$

Because the spatial tangent vectors of the minimal surface are constructed via $f'_k \propto \lambda^T \sigma_k \mu$, this strict algebraic constraint forces one component of the tangent vector to be zero everywhere on the worldsheet. This dimensionally reduces the physical minimal surface from a generic 4-dimensional embedding into a 3-dimensional hyperplane, exactly matching the geometric prerequisite for a canonical Helicoid.

Furthermore, we possess a global $U(1)$ symmetry on the worldsheet integration domain (the unit disk). The extremum equation for the effective action with respect to the pole position z_0 must reflect this. Because of this $U(1)$ symmetry, we may claim that there is always a symmetric solution where the pole is centered at the origin:

$$z_0 = 0 \quad (17.9)$$

The string dynamically centers itself to restore the $U(1)$ symmetry. By locking the pole to the origin, the minimal surface reduces exactly to the canonical, maximally symmetric Helicoid. The remaining computations then proceed in the exact same way as for the canonical Helicoid in Minkowski space. As we derive in a new section in the Appendix, the worldsheet metric following from these canonical twistors λ, μ transforms precisely into the canonical Nambu-Goto rotating string metric. In the text below, we simply use this metric.

17.5. The exact spectrum in the one pole sector

With the twistor saddle point locked to $z_0 = 0$ and the surface constrained to the 3D Helicoid,

we repeat the action computation. In this one-pole sector, there are no other terms; the entire worldsheet dynamics are governed by exactly two terms within the Liouville action: the classical area term (σ) and the kinetic anomaly ($|\nabla\rho|^2$).

Because the conformal density is strictly proportional to $1/|z|^2$, the kinetic term acts as a rigid, local shift to the effective Helicoid string tension. Evaluating the 1-cycle Minkowski bulk action, we obtain the effective Helicoid energy, complete with the anomalous Lüscher term:

$$S_{bulk}^{(1)} = -2\pi^2 \left(\sigma + \frac{1}{12\pi R^2} \right) R^2 = -2\pi^2 \sigma R^2 - \frac{\pi}{6} \quad (17.10)$$

Simultaneously, the boundary term coupling the string to the external energy E integrates to yield the exact phase monodromy per winding:

$$\Delta S_E = 4\pi ER \quad (17.11)$$

Summing these to form the total phase of one physical cycle, we enforce the geometric series resonance condition ($\Delta S_{\text{eff}} = 2\pi n$):

$$\begin{aligned} 4\pi ER - 2\pi^2 \sigma R^2 - \frac{\pi}{6} \\ = 2\pi n \implies 2ER - \pi\sigma R^2 - \frac{1}{12} = n \end{aligned} \quad (17.12)$$

To locate the physical vacuum, we minimize this effective base action with respect to the spatial radius R to balance the string tension against the injected energy:

$$\frac{\partial}{\partial R} (2ER - \pi\sigma R^2) = 2E - 2\pi\sigma R = 0 \implies R = \frac{E}{\pi\sigma} \quad (17.13)$$

Substituting this exact saddle-point radius back into the quantization condition, we obtain the exact algebraic spectral equation:

$$2E \left(\frac{E}{\pi\sigma} \right) - \pi\sigma \left(\frac{E}{\pi\sigma} \right)^2 - \frac{1}{12} = n \quad (17.14)$$

Simplifying the squares yields:

$$\frac{E^2}{\pi\sigma} = n + \frac{1}{12} \implies E^2 = \pi\sigma \left(n + \frac{1}{12} \right) \quad (17.15)$$

Since we are in the rest frame, the invariant mass squared is $m^2 = E^2$, resulting in the final string spectrum:

$$m^2 = \pi\sigma \left(n + \frac{1}{12} \right) \quad (17.16)$$

We got the famous Lüscher term, without any string models or assumptions. We obtained this term from the conformal anomaly left from the Elfin determinant, which we used to induce MM loop equations. This remarkable coincidence tells us that our solution for planar QCD matches accepted phenomenology as well as the results of the real and numerical experiments. QED! (or rather QCD!).

17.6. QCD as a Geometric Theory

The derivation of the exact spectral equation in the previous section represents a significant shift in our understanding of the large- N_c meson spectrum. We have moved from a stochastic description (random surfaces) to a deterministic geometric principle. Let us summarize the key physical insights that have emerged from this analysis.

Our approach avoids the usual “graviton problem” of gravity holography: since our bulk is not dynamical, there are no propagating bulk graviton modes (or other unwanted massless bulk fields) that would have no counterpart in confining QCD.

More precisely, the propagating degrees of freedom in the present formulation are confined to the boundary: (i) the quark loop degrees of freedom, represented by the matrix trace of the Dirac propagator around the boundary loop, and (ii) the holomorphic moduli (twistors) that parametrize the rigid minimal surface. The twistor moduli are specified by their boundary data and extended uniquely into the disk by analytic continuation (Plemelj/Hilbert reconstruction in the spirit of the Penrose transform). Accordingly, bulk quantities such as the Liouville field are not integrated over as independent quantum fields; they are determined functionally by the analytically continued twistor data.

It is also important not to conflate this construction with Witten/Berkovits twistor strings or other topological twistor-string models. In those theories the extension of boundary data into the bulk typically contributes a topological functional (e.g. a WZW term) whose value depends only on the homotopy class of the extension. In contrast, our bulk functional is not topological: its value depends on the specific holomorphic disk selected by the boundary loop, and this non-topological dependence is essential for confinement and for the existence of a mass scale. In this sense, our “rigid twistor string” is best viewed as *gauge holography* (bulk as a rigid encoding of boundary dynamics), rather than *gravity holography* or a topological string.

Finally, the observation relating the QCD mass spectrum to the degenerate saddle points of the complexified twistor-string action introduces the concept of localization of the string path integral, but on an entirely different level. Our spectral equation is exactly localized, much like the computation of path integrals in geometric quantization [51], but this is not a familiar fixed point in the moduli space. Instead, the path integral localizes exclusively on degenerate saddle points governed by catastrophe theory. We thus have uncovered a novel, purely geometric mechanism of localization that deterministically dictates the QCD mass spectrum.

17.7. Future Directions: Glueballs, Baryons and Scattering

The formulation of Planar QCD as an Analytic Twistor String opens several avenues for future research:

- **Glueballs:** the whole construction, starting with the loop equations to the fermion determinant at the minimal surface, to the rigid twistor string and the localization of the twistor path integral for quark amplitudes at the boundary of the moduli space, naturally generalizes to the higher $1/N_c$ corrections. There are some important mathematical issues to be resolved for that program to materialize. This is a natural next step for this Geometric QCD theory.
- **Baryons:** In the large- N_c limit, baryons appear as heavy states composed of N_c quarks. Geometrically, this corresponds to a minimal surface with a specific topology (e.g., a "Y-junction" or a surface with multiple boundaries) [5]. Extending the twistor ansatz to surfaces with higher connectivity is a natural next step.
- **Scattering Amplitudes:** We have focused here on the two-point function (spectrum). The four-point function (meson-meson scattering) involves a minimal surface bounded by four segments. The crossing symmetry and Regge behavior of these amplitudes should emerge from the analytic continuation of the twistor data, potentially connecting this framework to the modern "Amplituhedron" methods.

18. Conclusion

In this paper, we developed the dynamical part of the *Geometric QCD* program. Building on [1], where the confining dressing factor $\exp(-\kappa S[C])$ arises from the rigid Hodge-dual additive minimal surface, we formulated a concrete large- N_c framework in which the remaining degrees of freedom can be treated without summing over fluctuating worldsheet metrics.

The first main outcome is conceptual and structural: by working in momentum loop space, we bypass the coordinate-space contact singularities and cusp pathologies that obscure the local continuum interpretation of the loop equations. In this representation, the planar loop equation becomes an algebraic-differential equation. Furthermore, by mapping the Master Field to the infinite-dimensional Cuntz-algebra "word space" (Section 10.8), we rigorously establish that a purely

one-dimensional *analytic Taylor–Magnus (finite-moment)* solution of the exact *vector* momentum-loop equation cannot exist: the expansion is consistent through $\mathcal{O}(P^6)$ but becomes algebraically inconsistent at $\mathcal{W}^{(8)}$ (Appendix C, Table C.1). This violent breakdown is a theorem-level obstruction showing that a 1D closed-loop scalar Taylor–Magnus framework lacks sufficient internal degrees of freedom to absorb the macroscopic spatial stress generated by planar QCD. This breakdown *prompts* the introduction of additional continuous degrees of freedom; in our construction these are the 4D boundary-twistor variables that parametrize the rigid Hodge-dual minimal surface and yield the confining twistor-string representation.

The second main outcome is dynamical: we showed that the fermionic (Majorana) worldsheet degrees of freedom of the Fermi string provide the correct algebraic mechanism for planar factorization at intersections, while the rigidity of the Hodge-dual minimal surface removes the Liouville instability of the original random-surface formulation. The resulting theory may be viewed as an *analytic (confining) twistor-string* description in which the reduced loop-space measure is most naturally written in twistor variables, leading to an effective holographic Liouville functional determined by holomorphic extension of boundary data.

The third main outcome concerns spectroscopy and the profound realization that the quantum path integral geometrically localizes. We initially demonstrated the computability of the boundary-twistor functional integral by evaluating it on the IAS Typhon supercluster via Complex Langevin (CLE) evolution with logarithmic reweighting. To overcome the severe topological trapping and infinite-variance $1/|u|^3$ Cauchy tails inherent to the complexified phase space, we introduced an unsupervised phase-information clustering algorithm. Applying this to our massive stochastic histories successfully isolated two distinct, approximately linear Regge trajectories. This numerical exploration served a crucial purpose: it proved that the Confining Twistor String natively possesses internal quantum numbers (analogous to string "daughter trajectories") emerging directly from the multiple complex saddle points (Lefschetz thimbles) of the path integral.

However, the ultimate realization of this work goes far beyond numerical stochasticity. By analyzing the analytic structure of the Twistor String, we discovered that the physical mass spectrum is deterministically governed by Catastrophe Theory. The meson poles correspond exactly to degenerate Lefschetz thimbles—bifurcation points where the complex stability matrix of the classical twistor trajectory develops a null space. Because the integration variables are coupled holomorphic twistors,

this degeneracy inherently possesses a corank of 2. As dictated by the singularity theory of multiple integrals, this complex degeneracy mathematically upgrades standard semiclassical square-root branch cuts into the exact simple poles of the meson states.

Summary

To summarize, what started as a rigorous continuum formulation of planar QCD via the Makeenko–Migdal loop equations culminated in an exact analytical solution for the fundamental meson spectrum. Although our numerical investigations using the Complex Langevin approach successfully provided proof-of-concept evidence for linear Regge trajectories, the true predictive power of this framework lies in its analytical semiclassical limit, which provides exact equations for the mass spectrum **beyond the WKB approximation at the non-perturbative level**. It is a known phenomenon that some WKB spectral equations are valid beyond the WKB approximation, because they reflect deeper hidden symmetries leading to infinite flat valleys for the steepest descent path, making the WKB estimate an exact localization of the path integral [11]. We have shown that the S -matrix mass poles of the theory are naturally captured by Catastrophe Theory, corresponding to non-compact flat valleys in the complexified effective action. These flat valleys, where the steepest descent integral diverges without higher-order corrections, are driven entirely by the topological monodromies of twistor poles enclosed within the unit disk.

The number of such poles serves as a rigorously conserved topological quantum number, protected by an absolute pinch-singularity barrier at the conformal boundary. The crossing of the unit circle by a twistor pole leads to a divergent action, because the conjugate poles z_0 and $1/\bar{z}_0$ inevitably pinch the physical integration loop. By analytically continuing the Euclidean area action to the boundary and summing over the exact purely imaginary monodromy phases, we obtain a Bohr–Sommerfeld quantization condition. For the fundamental one-pole trajectory, this yields the exact simple mass poles and the linear Regge spectrum:

$$m^2 = \pi\sigma \left(n + \frac{1}{12} \right) \quad (18.1)$$

This analytical result not only confirms the perfectly linear Regge slope but uniquely derives the exact open-string Lüscher intercept (+1/12) directly from the 2D anomaly of the Elfin determinant on rigid minimal surface. Thus, by mapping the momentum loop-space dynamics to boundary twistors, the theory does not merely approximate the confining dynamics of planar QCD; it provides its exact algebraic geometric solution. The exact analytical classification of higher topological sectors (multi-pole configurations) and their corresponding daughter trajectories is now a fully accessible problem. Consequently, Planar QCD ceases to be

a theory of stochastic quantum fluctuations; it becomes a theory of pure classical complex geometry. The extraction of the mass spectrum is reduced from a fluctuating path integral to a deterministic Generalized Eigenvalue Problem for the degenerate saddle points of the effective action.

Acknowledgements

I am grateful to Nima Arkani-Hamed for the invitation to present this work as a series of lectures at the IAS Particle Physics (Pizza) Seminar, which provided a stimulating environment for discussing these results. I also thank Edward Witten for valuable discussions regarding the distinction between this confining geometry and the holographic dualities of conformal field theories.

Declaration of generative AI and AI-assisted technologies in the writing process

During the preparation of this work, the author used Google Gemini to fix typographical errors, identify relevant mathematical terminology, clarify the notations, and improve the overall language and style. After using this tool, the author reviewed and edited the content as needed and takes full responsibility for the content of the publication.

Data Availability.

The spectral data reported in this paper are generated by numerical simulation of the Complex Langevin equation (CLE) for the discretized Confining Twistor String spectral observable, including the reweighted estimator for $1/R(E) = \Pi(E)/\Pi'(E)$. To enable reproduction and extension of these calculations, I have made the full *Mathematica*® workflow publicly available on the Wolfram Cloud, including (i) the CLE simulator and effective-action implementation, (ii) SLURM submission scripts for running independent replicas on an HPC cluster, and (iii) the analysis tools used to pool independent runs and extract the spectrum:

- `TwistorString.wl`, [52] (main CLE simulator):
- `run_node.m` (SLURM/cluster driver) [53]
- `VerifyTwistorHistory.nb` [54] (fat tail analysis of distributions for a CLE history):
- `TwistorInformationClustering.nb` [55] (spectrum extraction and plots)
- `GeometricQCD_CLE_results` [56] (the full set of histories of the evolution of $R(E)$ for 240 values of energy $E \in (2., 3.)$ ran on 64 nodes of Typhon cluster, with random initial states)

The raw per-replica output consists of node-indexed binary arrays (e.g. `TwistorHistory*.mx`) storing, for each sampled energy value, the whole stochastic trajectory of observable resolvent $R(E)$. These files are verified by `VerifyTwistorHistory.nb`, testing fat tails of distribution against theoretical prediction. Then `TwistorInformationClustering.nb` performs robust pooling across independent replicas, analyzes the history of the phase of the resolvent, builds the statistical distribution, clusters the data by information distance between these phase distributions and produces the final spectral curves and extracted mass tables. This public release is intended to provide a practical basis for future large-scale runs (larger ensembles, finer discretization, and improved CLE diagnostics and stabilization methods).

References

- [1] A. Migdal, [Geometric qcd i: The hodge-dual surface and quark confinement](#), arXiv:2511.13688v7 (2026). arXiv:2511.13688. URL <https://arxiv.org/abs/2511.13688v7>
- [2] A. Migdal, [Spontaneous quantization of the yang-mills gradient flow](#), Nuclear Physics B 1020 (2025) 117129. doi:<https://doi.org/10.1016/j.nuclphysb.2025.117129>. URL <https://www.sciencedirect.com/science/article/pii/S0550321325003384>
- [3] A. Migdal, Geometric solution of turbulence as diffusion in loop space, to appear in Philosophical Transactions A (2026). arXiv:<https://doi.org/10.48550/arXiv.2511.02165>, doi: [10.1098/rsta.2025.0032](https://doi.org/10.1098/rsta.2025.0032).
- [4] Y. Makeenko, A. Migdal, [Exact equation for the loop average in multicolor qcd](#), Physics Letters B 88 (1) (1979) 135–137. doi:[url{https://doi.org/10.1016/0370-2693\(79\)90131-X}](https://doi.org/10.1016/0370-2693(79)90131-X). URL <url{https://www.sciencedirect.com/science/article/pii/S037026937990131X}>
- [5] A. A. Migdal, Loop equations and $1/n$ expansion, Physics Reports 102 (4) (1983) 199–290. doi:[10.1016/0370-1573\(83\)90076-5](https://doi.org/10.1016/0370-1573(83)90076-5).
- [6] A. M. Polyakov, V. S. Rychkov, Gauge fields – strings duality and the loop equation, Nuclear Physics B 581 (2000) 116–134. arXiv:[hep-th/0002106](https://arxiv.org/abs/hep-th/0002106), doi:[10.1016/S0550-3213\(00\)00177-9](https://doi.org/10.1016/S0550-3213(00)00177-9).
- [7] Y. M. Makeenko, A. A. Migdal, Quantum chromodynamics as dynamics of loops, Nuclear Physics B 188 (1981) 269–316. doi:[10.1016/0550-3213\(81\)90105-2](https://doi.org/10.1016/0550-3213(81)90105-2).
- [8] A. Migdal, [Qcd=fermi string theory](#), Nuclear Physics B 189 (2) (1981) 253–294. doi:[https://doi.org/10.1016/0550-3213\(81\)90381-3](https://doi.org/10.1016/0550-3213(81)90381-3). URL <https://www.sciencedirect.com/science/article/pii/0550321381903813>
- [9] H. Poincaré, Sur l’uniformisation des fonctions analytiques, Acta Mathematica 31 (1) (1907) 1–63. doi:[10.1007/BF02415442](https://doi.org/10.1007/BF02415442).
- [10] T. Radó, On Plateau’s problem, Annals of Mathematics 31 (3) (1930) 457–469. doi:[10.2307/1968237](https://doi.org/10.2307/1968237).
- [11] J. J. Duistermaat and G. J. Heckman, “On the Variation in the Cohomology of the Symplectic Form of the Reduced Phase Space,” *Inventiones mathematicae* **69** (1982) 259–268.
- [12] J. Douglas, [Solution of the problem of plateau](#), Transactions of the American Mathematical Society 33 (1) (1931) 263–321. doi:[10.2307/1989631](https://doi.org/10.2307/1989631). URL <https://doi.org/10.2307/1989631>
- [13] R. Gulliver, Regularity of minimizing surfaces of prescribed mean curvature, Annals of Mathematics 97 (2) (1973) 275–305. doi:[10.2307/1970845](https://doi.org/10.2307/1970845).
- [14] P. B. Gilkey, Invariance Theory, the Heat Equation, and the Atiyah-Singer Index Theorem, 2nd Edition, CRC Press, 1995.
- [15] T. Ichinose, H. Tamura, Propagation of a Dirac particle: A path integral approach, J. Math. Phys. 25 (6) (1984) 1810–1819. doi:[10.1063/1.526366](https://doi.org/10.1063/1.526366).
- [16] B. Gaveau, T. Jacobson, M. Kac, L. S. Schulman, Relativistic Extension of the Analogy between Quantum Mechanics and Brownian Motion, Phys. Rev. Lett. 53 (1984) 419–422. doi:[10.1103/PhysRevLett.53.419](https://doi.org/10.1103/PhysRevLett.53.419).
- [17] N. V. Vdovichenko, A Calculation of the Partition Function for a Plane Dipole Lattice, Sov. Phys. JETP 20 (2) (1965) 477–488, [Zh. Eksp. Teor. Fiz. 47, 715 (1964)].
- [18] A. A. Migdal, QCD = Fermi String Theory, Phys. Lett. B 96 (3-4) (1980) 333–336. doi:[10.1016/0370-2693\(80\)90779-7](https://doi.org/10.1016/0370-2693(80)90779-7).
- [19] A. M. Polyakov, Gauge Fields and Strings, Taylor & Francis, 1987.
- [20] H. Whitney, On regular closed curves in the plane, *Compositio Mathematica* 4 (1937) 276–284.
- [21] S.-S. Chern, A simple intrinsic proof of the Gauss-Bonnet formula for closed Riemannian manifolds, *Annals of Mathematics* 45 (4) (1944) 747–752.
- [22] G. ’tHooft, A planar diagram theory for strong interactions, Nucl. Phys. B 72 (1974) 461–473. doi:[10.1016/0550-3213\(74\)90154-0](https://doi.org/10.1016/0550-3213(74)90154-0).
- [23] V. A. Kazakov, A. A. Migdal, Induced QCD

- at large N , Nucl. Phys. B 397 (1-2) (1993) 214–238. [arXiv:hep-th/9206015](https://arxiv.org/abs/hep-th/9206015), [doi:10.1016/0550-3213\(93\)90342-4](https://doi.org/10.1016/0550-3213(93)90342-4).
- [24] B. White, The bridge principle for stable minimal surfaces, Calculus of Variations and Partial Differential Equations 4 (5) (1996) 411–425.
- [25] Y. M. Makeenko, On the Equivalence of the Contour Equation and the Schwinger-Dyson Equation, Yad. Fiz. 33 (1981) 526, [Sov. J. Nucl. Phys. 33, 274 (1981)]; Preprint ITEP-141 (1979).
- [26] Y. Wang, Equivalent descriptions of the Loewner energy, Inventiones mathematicae 218 (2) (2019) 573–621. [doi:10.1007/s00222-019-00887-2](https://doi.org/10.1007/s00222-019-00887-2).
- [27] G. P. Korchemsky, A. V. Radyushkin, Renormalization of the wilson loops beyond the leading order, Nuclear Physics B 283 (1987) 342–364. [doi:10.1016/0550-3213\(87\)90277-X](https://doi.org/10.1016/0550-3213(87)90277-X).
- [28] R. Penrose, W. Rindler, Spinors and Space-Time: Volume 1, Two-Spinor Calculus and Relativistic Fields, Vol. 1, Cambridge University Press, Cambridge, 1984.
- [29] D. A. Hoffman, R. Osserman, The geometry of the generalized Gauss map, Mem. Amer. Math. Soc. 28 (236) (1980).
- [30] A. Migdal, [Second quantization of the wilson loop](https://arxiv.org/abs/hep-th/9505151), Nuclear Physics B - Proceedings Supplements 41 (1) (1995) 151–183. [doi:https://doi.org/10.1016/0920-5632\(95\)00433-A](https://doi.org/10.1016/0920-5632(95)00433-A). URL <https://www.sciencedirect.com/science/article/pii/092056329500433A>
- [31] A. Migdal, [Momentum loop dynamics and random surfaces in qcd](https://arxiv.org/abs/hep-th/8605054), Nuclear Physics B 265 (4) (1986) 594–614. [doi:https://doi.org/10.1016/0550-3213\(86\)90331-7](https://doi.org/10.1016/0550-3213(86)90331-7). URL <https://www.sciencedirect.com/science/article/pii/0550321386903317>
- [32] A. A. Migdal, Hidden symmetries of large N QCD, Prog. Theor. Phys. Suppl. 131 (1998) 269–307. [arXiv:hep-th/9610126](https://arxiv.org/abs/hep-th/9610126), [doi:10.1143/PTPS.131.269](https://doi.org/10.1143/PTPS.131.269).
- [33] A. Migdal, Quantum solution of classical turbulence: Decaying energy spectrum, Physics of Fluids 36 (9) (2024) 095161. [doi:10.1063/5.0228660](https://doi.org/10.1063/5.0228660).
- [34] W. Magnus, On the exponential solution of differential equations for a linear operator, Communications on Pure and Applied Mathematics 7 (4) (1954) 649–673. [doi:10.1002/cpa.3160070404](https://doi.org/10.1002/cpa.3160070404).
- [35] K.-T. Chen, Iterated path integrals, Bulletin of the American Mathematical Society 83 (5) (1977) 831–879. [doi:10.1090/S0002-9904-1977-14339-5](https://doi.org/10.1090/S0002-9904-1977-14339-5).
- [36] E. B. Dynkin, Calculation of the coefficients in the campbell-hausdorff formula, Doklady Akademii Nauk SSSR 57 (1947) 323–326.
- [37] R. Ree, Lie elements and an algebra associated with shuffles, Annals of Mathematics 68 (2) (1958) 210–220.
- [38] C. Reutenauer, Free Lie Algebras, Vol. 7 of London Mathematical Society Monographs, Oxford University Press, 1993.
- [39] A. Migdal, "mle algebraic", <https://www.wolframcloud.com/obj/sasha.migdal/Published/MLEAlgebraic.nb> (02 2026).
- [40] D.-V. Voiculescu, K. J. Dykema, A. Nica, Free Random Variables, Vol. 1 of CRM Monograph Series, American Mathematical Society, Providence, RI, 1992.
- [41] R. Speicher, Multiplicative functions on the lattice of noncrossing partitions and free probability, Mathematische Annalen 298 (1) (1994) 611–628.
- [42] G. Parisi, On complex probabilities, Physics Letters B 131 (2) (1983) 393–395. [doi:10.1016/0370-2693\(83\)90525-7](https://doi.org/10.1016/0370-2693(83)90525-7).
- [43] M. P. do Carmo, Differential Geometry of Curves and Surfaces, Prentice-Hall, 1976, see Section 2.5 for the Helicoid metric calculation.
- [44] E. Witten, A New Look At The Path Integral Of Quantum Mechanics, Pure Appl. Math. Q. 7 (2011) 473–534. [arXiv:1009.6032](https://arxiv.org/abs/1009.6032), [doi:10.4310/PAMQ.2011.v7.n2.a15](https://doi.org/10.4310/PAMQ.2011.v7.n2.a15).
- [45] M. Cristoforetti, F. Di Renzo, L. Scorzato, New approach to the sign problem in quantum field theories: High density QCD on a Lefschetz thimble, Phys. Rev. D 86 (2012) 074506. [arXiv:1205.3996](https://arxiv.org/abs/1205.3996), [doi:10.1103/PhysRevD.86.074506](https://doi.org/10.1103/PhysRevD.86.074506).
- [46] Alexandru, Andrei and Başar, Gökçe and Bedaque, Paulo F. and Warrington, Gregory W., Complex paths around the sign problem, Rev. Mod. Phys. 94 (1) (2022) 015006. [arXiv:2007.05436](https://arxiv.org/abs/2007.05436), [doi:10.1103/RevModPhys.94.015006](https://doi.org/10.1103/RevModPhys.94.015006).
- [47] V. I. Arnold, S. M. Gusein-Zade, A. N. Varchenko, Singularities of Differentiable Maps, Volume II: Monodromy and Asymptotics of Integrals, Monographs in Mathematics, Birkhäuser Boston, 1988.
- [48] R. J. Eden, P. V. Landshoff, D. I. Olive, J. C. Polkinghorne, The Analytic S-Matrix, Cambridge University Press, 1966.
- [49] M. C. Gutzwiller, Periodic orbits and classical quantization conditions, Journal of Mathematical Physics 12 (3) (1971) 343–358.
- [50] R. F. Dashen, B. Hasslacher, A. Neveu, Non-perturbative methods and extended-hadron models in field theory. ii. two-dimensional models and extended hadrons, Physical Review D 10 (12) (1974) 4130–4142.
- [51] N. M. J. Woodhouse, Geometric Quantization,

2nd Edition, Oxford University Press, Oxford, 1997.

- [52] A. Migdal, "qcd twistor string", <https://www.wolframcloud.com/obj/sasha.migdal/Published/TwistorString.wl.nb> (02 2026).
- [53] A. Migdal, "qcd twistor string run", https://www.wolframcloud.com/obj/sasha.migdal/Published/run_node.m.nb (02 2026).
- [54] A. Migdal, "qcd verify twistor history", <https://www.wolframcloud.com/obj/sasha.migdal/Published/VerifyTwistorHistory.nb> (02 2026).
- [55] A. Migdal, "qcd twistor information clustering", <https://www.wolframcloud.com/obj/sasha.migdal/Published/TwistorInformationClustering.nb> (02 2026).
- [56] S. Migdal, Geometric qcd cle results, <https://drive.google.com/drive/folders/1vgJd7A4sW-TC98Wayqz27-FjnUR29uXS?usp=sharing>, accessed: 19-February-2026 (2026).
- [57] A. Enneper, Analytisch-geometrische untersuchungen, Zeitschrift für Mathematik und Physik 9 (1864) 96–125.
- [58] L. Euler, Methodus inveniendi lineas curvas maximi minimive proprietate gaudentes, Marc-Michel Bousquet, Lausanne & Geneva, 1744, chapter 5.
- [59] L. Henneberg, Über solche minimalflächen, welche eine vorgeschriebene ebene kurve zur geodätischen linie haben, Ph.D. thesis, Eidgenössische Technische Hochschule Zürich (1875).
- [60] C. E. Berger, L. Rammelmüller, A. C. Loheac, F. Evey, J. Braun, J. E. Drut, A. N. Nicholson, Complex Langevin and other approaches to the sign problem in quantum many-body physics, Phys. Rept. 892 (2021) 1–54. [arXiv:1907.10183](https://arxiv.org/abs/1907.10183), [doi:10.1016/j.physrep.2020.09.002](https://doi.org/10.1016/j.physrep.2020.09.002).

Appendix A. Conformal anomaly in determinants

Appendix A.1. Laplace operator

Let us consider the logarithm of the determinant of the scalar Laplace operator:

$$\ln \det \hat{L} = \text{tr} \ln \hat{L}. \quad (\text{A.1})$$

We apply the standard Pauli-Villars regularization

$$(\ln \hat{L})_{reg} = \ln \hat{L} - \sum c_i \ln(\hat{L} + M_i^2). \quad (\text{A.2})$$

Now, at finite regulator masses M_i the trace converges provided the constants c_i satisfy the sum

rules

$$\sum c_i M_i^{2k} = \delta_{k0}, \quad k = 0, 1, \dots \quad (\text{A.3})$$

Consider now the conformal variation

$$\delta \hat{L} = -\delta e e^{-1} \hat{L}, \quad (\text{A.4})$$

$$\delta \ln \hat{L} = \delta \hat{L} \hat{L}^{-1} = -\delta e e^{-1}; \quad (\text{A.5})$$

$$\delta \ln(\hat{L} + M^2) = -\delta e e^{-1} (1 - M^2(\hat{L} + M^2)^{-1}). \quad (\text{A.6})$$

The variation of the regularized trace (A.2) reads-

$$\delta \text{tr}(\ln \hat{L})_{reg} = - \sum c_i \text{tr}(\delta e e^{-1} M_i^2 (\hat{L} + M_i^2)^{-1}). \quad (\text{A.7})$$

Now only the regulator terms contribute, so that we may apply the WKB expansion

$$\hat{L} = -\frac{1}{e}(\partial_\xi)^2 \rightarrow -\frac{1}{e_0} \left(1 + \frac{e_0 R_0}{4}(\xi - \xi_0)^2\right) (\partial_\xi)^2 \quad (\text{A.8})$$

where R_0 is the local curvature. Here ξ_0 is the running point in the integral

$$\begin{aligned} & \text{tr} \delta e e^{-1} M^2 (\hat{L} + M^2)^{-1} \\ &= \int d^2 \xi_0 \delta e_0 e_0^{-1} M^2 \langle \xi_0 | (\hat{L} + M^2)^{-1} | \xi_0 \rangle. \end{aligned} \quad (\text{A.9})$$

Using the Fourier expansion at the tangent plane,

$$\begin{aligned} & \langle \xi_0 | (\hat{L} + M^2)^{-1} | \xi_0 \rangle \\ & \rightarrow e_0 \int \frac{d^2 p}{(2\pi)^2} (M^2 + p^2 - R_0/4(\partial_p)^2)^{-1} \\ & \rightarrow e_0 \int \frac{d^2 p}{(2\pi)^2} (M^2 + p^2)^{-1} \left(1 + R_0/4(\partial_p)^2 \frac{p^2}{M^2 + p^2}\right) \end{aligned} \quad (\text{A.10})$$

and calculating the Fourier integral, we find [by virtue of (A.3)]

$$\begin{aligned} & \delta \text{tr}(\ln \hat{L})_{reg} \\ &= \int \frac{d^2 \xi_0}{4\pi} \delta e_0 \left(\sum c_i M_i^2 \ln M_i^2 - 1/6R \right). \end{aligned} \quad (\text{A.11})$$

This equation can be easily integrated backwards:

$$\text{tr}(\ln \hat{L})_{reg} = a_0 + \int d^2 \xi \left(a_1 e - \frac{(\partial_a \ln e)^2}{48\pi} \right), \quad (\text{A.12})$$

with

$$a_1 = \frac{1}{4\pi} \sum c_i M_i^2 \ln M_i^2, \quad (\text{A.13})$$

and arbitrary constant a_0 .

Appendix A.2. Dirac operator

In case of the square of the Dirac operator D^2 the WKB expansion starts as follows:

$$D^2 \approx \mathbb{1}(\hat{L} + R/4) + \frac{i\sigma_3}{4} R \epsilon_{ab} \xi_a \partial_{\xi_b}. \quad (\text{A.14})$$

The definition of the Dirac operator was given in the text. The same line of argument as with the Laplace operator yields

$$\begin{aligned} & \sum_{\alpha=1,2} \langle \alpha \xi_0 | (D^2 + M^2)^{-1} | \alpha \xi_0 \rangle \\ & \rightarrow 2e_0 \int \frac{d^2 p}{(2\pi)^2} (M^2 + p^2)^{-1} \\ & (1 + 1/4 R_0 (-1 + (\partial_p)^2 p^2) (M^2 + p^2)^{-1}), \quad (\text{A.15}) \end{aligned}$$

$$\begin{aligned} & \delta \text{tr}(\ln D^2)_{reg} \\ & = -2 \int \frac{d^2 \xi_0}{4\pi} \delta e_0 \left[\sum c_i M_i^2 \ln M_i^2 - R/12 \right], \quad (\text{A.16}) \end{aligned}$$

$$\text{tr}(\ln D^2)_{reg} = b_0 + \int d^2 \xi \left[b_1 e + \frac{\partial \ln e}{12\pi} \right]. \quad (\text{A.17})$$

The additional factor of 2 in these relations comes from two spin states $a = 1, 2$. The term with the σ_3 matrix in (A.14) did not contribute.

Note the remarkable relation

$$\det D^2 \det \hat{L} = \text{const} \cdot \exp(\text{const Area}) \quad (\text{A.18})$$

which follows from the above formulas.

Appendix B. Spinor Factorization and Analytical Structure of Minimal surface

The mathematical problem of minimization of the Dirichlet functional with Virasoro constraint in four dimensions is a well known problem in modern mathematics. Let us briefly summarize the existing theory.

Appendix B.1. Twistor Framework and the Klein Quadric

The fundamental constraint of the theory is the null condition on the holomorphic tangent vector of the minimal surface, $(f')^2 = \sum_{\mu=1}^4 (f'_\mu)^2 = 0$. Geometrically, this defines the *Klein Quadric* in the complexified tangent space $\mathbb{C}\mathbb{P}^3$. Using the isomorphism $SO(4, \mathbb{C}) \cong SL(2, \mathbb{C})_L \times SL(2, \mathbb{C})_R$, we map the vector f'_μ to a 2×2 matrix $f'_{ab} = f'_\mu (\sigma_\mu)_{ab}$. The null condition corresponds to $\det(f') = 0$, ensuring the matrix has rank 1. Thus, the tangent vector factorizes globally into a product of two spinors:

$$f'_{ab}(z) = \lambda_a(z) \mu_b(z) \quad (\text{B.1})$$

where λ_a and μ_b are meromorphic sections of spinor bundles over the worldsheet. This factorization linearizes the quadratic Virasoro constraint, replacing it with the problem of determining the analytic properties of the spinors.

Appendix B.2. Gauge Invariance and Birkhoff Factorization

The physical vector f' is invariant under the local complex gauge transformation:

$$\lambda_a(z) \rightarrow w(z) \lambda_a(z), \quad \mu_b(z) \rightarrow w^{-1}(z) \mu_b(z) \quad (\text{B.2})$$

where $w(z)$ is a meromorphic function. This redundancy is governed by the Birkhoff-Grothendieck theorem on the splitting of vector bundles over \mathbb{P}^1 . The gauge function $w(z)$ allows us to distribute the zeroes and poles between λ and μ , classifying solutions by integer topological indices (partial indices) related to the winding number of the gauge field required to regularize the spinors at infinity.

Appendix B.3. Analytic Structure via Plemelj Projection

The connection to the physical loop $C(\sigma)$ (where $\sigma = e^{i\theta}$) is achieved via the Plemelj-Sokhotski decomposition. We expand the loop coordinates into positive and negative frequency modes:

$$C(\sigma) = C_+(\sigma) + C_-(\sigma) = \sum_{n \geq 0} c_n \sigma^n + \sum_{n < 0} c_n \sigma^n \quad (\text{B.3})$$

If the loop is algebraic, $C_-(\sigma)$ extends to a rational function $C_-(z)$ in the complex plane $|z| > 1$. The poles of the spinor solution $f'(z)$ are dictated by the singularities of $C_-(z)$. Analytically, the problem is to find the "closest" null vector f' to the derivative $\partial_z C_+$. This is equivalent to finding a subspace W in the Sato Grassmannian that satisfies the isotropic condition and matches the boundary data.

Appendix B.4. Explicit Algebraic Solutions

The general theory of the spinor factorization predicts that rational choices for the sections $\lambda_a(z)$ and $\mu_b(z)$ generate algebraic minimal surfaces. These correspond to "Finite Gap" solutions where the algebraic curve has a finite genus. The distribution of poles between the spinors determines the topology and boundary behavior of the surface.

We illustrate this with four classical examples, reinterpreted in our spinor language: **1. The Enneper Surface (Polynomial Solution)**. This is the simplest solution with trivial topology (genus zero, one boundary at infinity), corresponding to polynomial spinors with a single pole at $z = \infty$.

$$\lambda(z) = \begin{pmatrix} 1 \\ z \end{pmatrix}, \quad \mu(z) = \begin{pmatrix} 1 \\ -z \end{pmatrix} \quad (\text{B.4})$$

The resulting null vector $f'(z) \sim (1 - z^2, i(1 + z^2), 2z, 0)$ integrates to a cubic polynomial map. This surface, discovered by Enneper in 1864 [57], represents the fundamental "ground state" of the algebraic solutions. **2. The Catenoid (Rational Solution with Poles)**. To generate a surface with the topology of an annulus (the only minimal

surface of revolution), one must introduce simple poles into the spinors.

$$\lambda(z) = \begin{pmatrix} z^{-1/2} \\ z^{1/2} \end{pmatrix}, \quad \mu(z) = \begin{pmatrix} z^{-1/2} \\ -z^{1/2} \end{pmatrix} \quad (\text{B.5})$$

Using the gauge freedom $\lambda \rightarrow w\lambda, \mu \rightarrow w^{-1}\mu$ with $w = z^{-1/2}$, we can redistribute the poles to find the standard rational form. Euler [58] originally proved the minimality of this surface, which corresponds to the physical shape of a soap film stretched between two rings. **3. The Henneberg Surface (Non-Orientable).** A more complex rational ansatz generates the Henneberg surface [59], which is a non-orientable minimal surface (a realization of the projective plane in 3D space). It arises from a rational map of degree 4:

$$\lambda(z) = \begin{pmatrix} 1 - z^{-2} \\ z - z^{-1} \end{pmatrix}, \quad \mu(z) = \begin{pmatrix} 1 \\ -1 \end{pmatrix} \quad (\text{B.6})$$

4. The Helicoid (Transcendental Solution). The Helicoid is the locally isometric conjugate surface to the Catenoid. In the spinor formalism, it arises from the same meromorphic data but with a phase shift that exposes the period of the complex logarithm.

$$\lambda(z) = e^{i\pi/4} \begin{pmatrix} z^{-1/2} \\ z^{1/2} \end{pmatrix}, \quad \mu(z) = e^{i\pi/4} \begin{pmatrix} z^{-1/2} \\ -z^{1/2} \end{pmatrix} \quad (\text{B.7})$$

The resulting null vector possesses a pole with purely imaginary residue, $f'(z) \sim i/z$. Integration yields a logarithmic branch cut $f(z) \sim i \ln z$, corresponding to the multi-valued height function of the double helix ($X_3 \propto \text{Im}(\ln z) = \theta$).

Appendix C. Explicit invariant tensor solutions for the MLE

In this appendix, we provide the explicit polynomial solutions for the finite functional Taylor–Magnus expansion of the Momentum Loop Equation, valid up to the non-analytic boundary at $\mathcal{W}^{(8)}$.

Appendix C.1. Solving for the lowest terms $\mathcal{W}^{(n < 8)}$

The vacuum is normalized to $\mathcal{W}^{(0)} = 1$. With the topological closure of the boundary gaps enforced via the subtraction of interleaved permutations, all odd traces identically vanish, $\mathcal{W}^{(2k-1)} = 0$.

The fully symmetric even-parity invariant tensors are constructed from all possible pair-wise contractions of the Kronecker delta $\delta_{\mu\nu}$. The lowest-order non-trivial tensors, parameterized by the unconstrained fundamental mass scales, evaluate to:

$$\begin{aligned} \mathcal{W}_{\mu_1\mu_2}^{(2)} &= \delta_{\mu_1\mu_2} \\ \mathcal{W}_{\mu_1\mu_2\mu_3\mu_4}^{(4)} &= \frac{1}{6} \delta_{\mu_1\mu_3} \delta_{\mu_2\mu_4} \\ &+ c_{4,1} (\delta_{\mu_1\mu_2} \delta_{\mu_3\mu_4} + \delta_{\mu_1\mu_4} \delta_{\mu_2\mu_3}) \end{aligned} \quad (\text{C.1})$$

The tensor $\mathcal{W}_{\mu_1\dots\mu_6}^{(6)}$ is completely determined by the geometric stress cascading from the left-hand side loop derivative acting on the lower-order terms, successfully absorbing the kinematic constraints without contradiction. Its explicit expansion in terms of the 15 independent 6-point Kronecker pairings is uniquely fixed by the lower-order parameters $c_{2,1} \equiv 1$, $c_{4,1}$, and $c_{4,2}$.

At $\mathcal{W}^{(8)}$, this linear absorption fails. The expansion truncates due to the irreducible non-linear $\mathcal{W}^{(4)} \times \mathcal{W}^{(4)}$ stress, which exceeds the tensor rank of the pure cyclic Shuffle Ideal basis, rigorously proving the non-analyticity of the functional $\mathcal{W}[P]$.

We compute these terms in [39], where we prove lack of solution for $\mathcal{W}^{(8)}$.

Appendix C.2. Counting of unknowns/equations and Fredholm inconsistency at $\mathcal{W}^{(8)}$

To rigorously demonstrate the breakdown of the Taylor–Magnus expansion at the 8th order ($\mathcal{W}^{(8)}$), we cast the Momentum Loop Equation at each order n into a finite linear system. After imposing the closed-loop shuffle-ideal reduction (loop-closing prescription), cyclic symmetry, and parity constraints (all odd orders vanish), the exact functional matching reduces to:

$$A_n x_n = b_n \quad (\text{C.2})$$

where the vector of unknowns x_n is explicitly decomposed as:

$$x_n = (c^{(n)}; \alpha^{(<n)}; g^{(n)}) \quad (\text{C.3})$$

Here, $c^{(n)}$ are the coefficients of the invariant-tensor basis of $\mathcal{W}^{(n)}$, $\alpha^{(<n)}$ are the residual free parameters surviving from lower-order solutions (e.g., those left unconstrained in $\mathcal{W}^{(4)}$ and $\mathcal{W}^{(6)}$), and $g^{(n)}$ are the gauge parameters associated with solving modulo the closed-loop shuffle ideal.

The total number of unknown variables solved for at order n is therefore $N_{unk}(n) = N_{\mathcal{W}}(n) + N_{free}(<n) + N_{gauge}(n)$. We analyzed the exact linear algebra of these systems using a specialized symbolic script. The exact matrix ranks and subsystem counts are summarized in Table C.1.

The finite-dimensional system $A_n x_n = b_n$ is solvable if and only if it satisfies the Fredholm alternative consistency condition:

$$u^T b_n = 0 \quad \forall u \in \text{LeftNull}(A_n) \quad (\text{C.4})$$

At $n = 8$, the matrix A_8 possesses 297 left-null vectors. Projecting the inhomogeneous right-hand side b_8 (the geometric stress generated by the discrete non-linear cross-terms of $\mathcal{W}^{(4)} \times \mathcal{W}^{(4)}$) onto these null directions yields explicit, non-zero rational obstructions. For example, selecting the first canonical left-null basis vector u_1 yields the exact rational projection:

$$u_1^T b_8 = \frac{1}{36} \neq 0 \quad (\text{C.5})$$

Order n	$N_{eq}(n)$	$N_{unk}(n)$	$\text{rank}(A_n)$	$\text{dim LeftNull}(A_n)$	Δrank	Solvable?
4	4	6	4	0	0	yes
6	31	30	26	5	0	yes
8	379	212	82	297	1	no

Table C.1: Linear algebra diagnostics for the exact Vector Momentum Loop Equation. Here $\Delta\text{rank} := \text{rank}([A_n|b_n]) - \text{rank}(A_n)$. A strict positivity, $\Delta\text{rank} > 0$, rigorously proves the system is mathematically inconsistent.

This establishes a decisive mathematical contradiction. Two critical robustness statements follow directly from this matrix representation:

- Because the vector of unknowns x_8 explicitly includes all residual lower-order parameters $\alpha^{(<8)}$, this inconsistency proves that *no possible choice* of lower-order free parameters can restore solvability.
- Setting the physical scale parameter to zero does not alleviate the structural rank deficiency.

The full basis construction, shuffle-ideal reduction, and exact linear-algebra verification—including the generation of the matrices A_n and the explicit null-vector projections—are provided in the executable Mathematica notebook [39] (see Data Availability).

Appendix D. Algorithm for Fast Spectral-Gaussian Integration

To evaluate the Liouville action in the bulk, we employ a spectral-product quadrature rule that combines the spectral accuracy of the boundary discretization with high-precision Gaussian integration in the radial direction. This method avoids coordinate singularities at the origin and preserves the holomorphicity of the extension.

The integral of the Liouville Lagrangian density over the unit disk is computed in polar coordinates:

$$S_{\text{Liouville}} = \int_0^1 r dr \int_0^{2\pi} d\theta L(\rho(r, \theta), |\partial_z \rho(r, \theta)|^2) \quad (\text{D.1})$$

We discretize this domain using a product grid defined by the N roots of unity in the angular direction and M Gauss-Legendre nodes in the radial direction.

1. The Radial Grid (Gauss-Legendre): We map the standard Legendre nodes $x_m \in [-1, 1]$ (roots of the Legendre polynomial $P_M(x)$) to the radial interval $r \in (0, 1]$:

$$r_m = \frac{1 + x_m}{2}, \quad w'_m = \frac{w_m}{2} \quad (\text{D.2})$$

where w_m are the standard weights. This quadrature is exact for polynomials of degree $2M - 1$. Since the origin $r = 0$ is not a node, the coordinate singularity is naturally avoided.

2. The Angular Grid (Roots of Unity): For the angular integration, we use the trapezoidal rule on the N vertices of the polygon, $\theta_k = 2\pi k/N$, $\omega_k = e^{i\theta_k}$. For periodic functions (such as our fields on circles of constant radius), this rule exhibits exponential convergence (spectral accuracy).

3. Bulk Field Evaluation: The values of the (anti)holomorphic null-vector fields $W(z) = \{V(z), \tilde{V}(\bar{z})\}$ at a grid point $z_{mk} = r_m \omega_k$ are computed using the analytic extension formula (E.3). Crucially, the term $(z_{mk}/\omega_j)^N$ reduces to r_m^N , which is independent of the angular indices. This simplifies the kernel significantly:

$$V(r_m \omega_k) = \frac{1 - r_m^N}{N} \sum_{j=0}^{N-1} \frac{V(\omega_j)}{1 - r_m \omega_k / \omega_j}; \quad (\text{D.3})$$

$$\tilde{V}(r_m \bar{\omega}_k) = \frac{1 - r_m^N}{N} \sum_{j=0}^{N-1} \frac{\tilde{V}(\omega_j)}{1 - r_m \bar{\omega}_k / \omega_j} \quad (\text{D.4})$$

This summation takes the form of a discrete convolution. By choosing N to be a power of 2 (e.g., $N = 128$), this convolution can be accelerated via Fast Fourier Transform (FFT) to $O(N \log N)$ operations per radial ring, providing a massive speedup over the naive $O(N^2)$ summation.

4. Hybrid Algorithm for Analytic Derivative: The kinetic term in the Liouville action requires the holomorphic derivative $\partial_z \Lambda$. To maintain precision, we differentiate the interpolating polynomial analytically. Differentiating (E.3) with respect to z yields:

$$\partial_z V(z) \Big|_{z_{mk}} = \frac{1}{N} \sum_{j=0}^{N-1} V(\omega_j) / \omega_j K'(z_{mk} / \omega_j) \quad (\text{D.5})$$

where $K'(w)$ is the derivative of the geometric series kernel. To optimize computational complexity without sacrificing stability near the boundary, we employ a hybrid algorithm:

a) *The Fractional Form (Bulk):* For the majority of grid points in the bulk ($1 - r_m > \epsilon \sim 0.1$), we use the closed fractional form:

$$K'(w) = \frac{(1 - w^N) + Nw^{N-1}(1 - w)}{(1 - w)^2} \quad (\text{D.6})$$

This form is algebraically equivalent to the standard derivative but is numerically rearranged to avoid cancellations. Its evaluation is $O(1)$, ensuring the total derivative calculation remains efficient.

b) *The Geometric Doubling Algorithm (Boundary Layer)*: For the outermost radial nodes where $r_m > 1 - \epsilon$, the fractional form suffers from numerical instability due to the denominator $(1 - w)^2$. In this "skin" layer, we switch to the exact polynomial sum $K'(w) = \sum_{n=1}^{N-1} nw^{n-1}$. Crucially, for $N = 2^k$, this sum can be evaluated in $O(\log N)$ operations using the recursive doubling identity for geometric series:

$$S_{2N}(w) = (1 + P_N(w))S_N(w); \quad (\text{D.7})$$

$$P_{2N}(w) = P_N^2(w); \quad (\text{D.8})$$

$$S_1(w) = 1; \quad P_1(w) = w; \quad (\text{D.9})$$

and its derivative by w . Here is the iterative algorithm:

Algorithm 1 Fast Geometric Doubling Algorithm ($O(\log N)$)

Require: Complex argument w , Iterations k (where $N = 2^k$)

Ensure: Kernel values $K = \sum_{n=0}^{N-1} w^n$ and $K' = \sum_{n=1}^{N-1} nw^{n-1}$

- 1: **Initialize:**
 - 2: $P \leftarrow w$ {Current Power w^{2^i} }
 - 3: $K \leftarrow 1$ {Current Sum}
 - 4: $P' \leftarrow 1$ {Derivative of Power}
 - 5: $K' \leftarrow 0$ {Derivative of Sum}
 - 6: **for** $i = 1$ to k **do**
 - 7: $K' \leftarrow (1 + P)K' + P'K$ {Update Derivative of Sum (Product Rule)}
 - 8: $K \leftarrow (1 + P)K$ {Update Sum ($S_{2M} = (1 + w^M)S_M$)}
 - 9: $P' \leftarrow 2 \cdot P \cdot P'$ {Update Derivative of Power}
 - 10: $P \leftarrow P \cdot P$ {Update Power ($w^{2^M} = (w^M)^2$)}
 - 11: **end for**
 - 12: **return** K, K'
-

This iterative algorithm computes both the kernel and its derivative with logarithmic complexity $O(\log N)$, avoiding the $O(N)$ cost of the direct sum while using $O(1)$ memory and maintaining perfect numerical stability near the boundary. The numerical stability of this algorithm is verified in our *Mathematica*[®] code [52].

5. Summation: The total action is obtained by summing the weighted contributions:

$$S \approx \frac{2\pi}{N} \sum_{m=1}^M w'_m r_m \sum_{k=0}^{N-1} L_{\text{Liouville}}(r_m, \theta_k) \quad (\text{D.10})$$

This algorithm ensures that the bulk integration error is on the same order as the boundary discretization error, providing a stable and consistent numerical definition of the rigid twistor string. In our implementation (using *Mathematica*), the kernel data is precomputed into parallel tables, further accelerating the simulation.

Appendix E. Numerical Implementation of CLE

To resolve the severe sign problem inherent in the Twistor String path integral, we employ *Stochastic Quantization* via the Complex Langevin Equation (CLE) [42, 60].

Appendix E.1. Complexification of the parameter space

To ensure the strict analyticity of the stochastic evolution required by the Parisi condition [42], we must eliminate all non-holomorphic operations from the Langevin equations. We achieve this by complexifying the target manifold and analytically continuing the action integral itself. This ensures that the drift forces are partial derivatives of a globally holomorphic function.

We replace the original real and Hermitian variables with a set of independent holomorphic variables. The angular coordinates α_k are mapped to the complex plane via $z_1 = e^{i\alpha_1}, z_2 = e^{i\alpha_2}$. The spinor fields and their conjugates are treated as independent complex vectors. The full set of dynamical variables for the discretized loop is:

$$\mathcal{V} = \{\{z_1, z_2\}, \{\rho_k, \xi_k, \eta_k, \tilde{\xi}_k, \tilde{\eta}_k, \gamma_{1,k}, \gamma_{2,k}\}_{k=1}^N\}. \quad (\text{E.1})$$

Here, $\tilde{\xi}$ and $\tilde{\eta}$ replace $\bar{\xi}$ and $\bar{\eta}$ as independent variables. The geometric constraints are enforced by the complex Lagrange multipliers $\gamma_{1,k}$ and $\gamma_{2,k}$, leading to the holomorphic constraint terms in the effective action:

$$S_{\text{constr}} = i \sum_k [\gamma_{1,k}(\tilde{\xi}_k \xi_k - 1) + \gamma_{2,k}(\tilde{\eta}_k \eta_k - 1)]. \quad (\text{E.2})$$

Appendix E.2. Spectral Interpolation of Fields

To evaluate the action integrals analytically, we construct global holomorphic polynomials that interpolate the values at the vertices z_k .

Appendix E.2.1. Spinor Fields

Let $\Lambda^{(k)} = e^{\rho_k/2}(\xi_k, \eta_k)$ denote the spinor data $\Lambda(z) = \{\lambda(z), \mu(z)\}$ at vertex k . The Lagrange interpolation polynomial on the spectral unit circle is:

$$\Lambda(z) = \frac{1}{N} \sum_{k=0}^{N-1} \Lambda^{(k)} K(z e^{-i\theta_k}); \quad (\text{E.3})$$

$$K(z) = \frac{1 - z^N}{1 - z}; \quad (\text{E.4})$$

Using the Fast Fourier Transform (FFT), we extract the spectral coefficients L_n, M_n (and \tilde{L}_n, \tilde{M}_n from the independent $\tilde{\xi}, \tilde{\eta}$ variables) such that:

$$\lambda(z) = \sum_{n=0}^{N-1} L_n z^n, \quad \tilde{\lambda}(z) = \sum_{n=0}^{N-1} \tilde{L}_n z^n. \quad (\text{E.5})$$

$$\{L_n, M_n\} = \frac{1}{N} \sum_{k=0}^{N-1} \Lambda^{(k)} e^{-i\theta_k} \quad (\text{E.6})$$

Appendix E.2.2. Liouville Field

The Liouville field $\rho(z, \bar{z})$ is extended inside the unit circle via an exact formula

$$\rho(z, \bar{z}) = \frac{\log \tilde{\lambda}(\bar{z})\lambda(z) + \log \tilde{\mu}(\bar{z})\mu(z)}{2} \quad (\text{E.7})$$

where $\lambda(z), \mu(z)$ is extended by interpolation (E.3). The derivatives of the above kernel $K'(z)$ involved in the Liouville Lagrangian with this ρ were computed in the previous sections.

These expressions provide the values of the fields and derivatives at any complex z , not just at the vertices. These expressions also depend upon complex parameters in \mathcal{V} through the Fourier coefficients $\Lambda(k), \tilde{\Lambda}(k)$. This dependence is exponential for ρ_k and polynomial for the rest of variables in \mathcal{V} , which allows for required analytic continuation of the CLE.

Appendix E.3. The Boundary Terms in the action

The boundary part of the action involves integrals of the form $\text{Im} \int (\lambda \times \mu) e^{i\theta} d\theta$. Substituting the spectral expansions, the integrand becomes a sum of monomials $z^n z^m \cdot z = z^{n+m+1}$. We define the elementary holomorphic integral function:

$$G_p(z_1, z_2) \equiv \int_{z_1}^{z_2} z^p \frac{dz}{iz} = \frac{z_2^p - z_1^p}{ip}. \quad (\text{E.8})$$

With the restored measure factor, the power is $p = n + m + 1$. Since $n, m \geq 0$, the denominator $n + m + 1 \geq 1$ is strictly positive, ensuring there are no singularities in the complex plane.

The contribution to the action of external momentum q injected into the quark loop from the arc between z_1 and z_2 is:

$$S_q = -iq_\alpha \sum_{n=0}^{N-1} \sum_{m=0}^{N-1} [(L_n \sigma_\alpha M_m) - (\tilde{L}_n \sigma_\alpha^\dagger \tilde{M}_m)] G_{n+m+1}(z_1, z_2). \quad (\text{E.9})$$

Then, there are terms related to the constraints on the ξ, η variables. These terms are just discrete sums

$$S_\gamma = i \sum_{k=0}^{N-1} \gamma_{1,k} (\tilde{\xi}_k \xi_k - 1) + \gamma_{2,k} (\tilde{\eta}_k \eta_k - 1) \quad (\text{E.10})$$

In addition, there are terms related to the trace (12.30). Our complexification reduces this trace to

$$S_T = -\log T(\xi, \eta, \tilde{\xi}, \tilde{\eta}); \quad (\text{E.11})$$

$$T(\xi, \eta, \tilde{\xi}, \tilde{\eta}) = \text{tr} \prod_{k=0}^{N-1} i\mathcal{P}(\theta_k); \quad (\text{E.12})$$

$$\mathcal{P}(\theta) = 2i [z\eta\tilde{\xi}^T - \bar{z}\tilde{\eta}\eta^T]_{z=e^{i\theta}} \quad (\text{E.13})$$

Finally, our reweighting adds one more complex term to the action,

$$S_O = \log \mathcal{O}; \quad (\text{E.14})$$

$$\mathcal{O} = \frac{\partial S_q}{\partial q_4} = \sum_{n=0}^{N-1} \sum_{m=0}^{N-1} [(L_n M_m) - (\tilde{L}_n \tilde{M}_m)] G_{n+m+1}(z_1, z_2). \quad (\text{E.15})$$

All the above expressions are purely holomorphic functions of all the variables in \mathcal{V} .

Appendix E.4. The Bulk Action (Gauss-Legendre Integration)

The bulk action S_ρ involves the kinetic and potential terms for the Liouville field of the form: $\int d^2z [\partial_z \rho \partial_{\bar{z}} \rho + V(\rho)]$. Unlike the boundary term, this cannot be integrated in closed form due to the nonlinear dependence of both variables z, \bar{z} .

We evaluate this integral using M -point Gauss-Legendre quadrature coupled with spectral (FFT) summation over the roots of unity for the angular integration. The integration domain is divided into N rays $R : (0, z_k)$; $z_k = e^{i\theta_k}$. Then, M quadrature nodes $z_q \in (0, 1)$ are placed on each ray: $z_{k,q} = z_q e^{i\theta_k}$.

The bulk action is approximated as:

$$S_\rho \rightarrow \frac{1}{N} \sum_{k=0}^{N-1} \sum_{q=1}^M w'_q \mathcal{L}_{\text{bulk}}(\rho(z_{k,q}), \rho'(z_{k,q})). \quad (\text{E.16})$$

Here, the values of the field $\rho(z, \bar{z})$ and its derivative $\rho'(z, \bar{z})$ at the quadrature points $z_{k,q}$ are computed exactly using the spectral Lagrange interpolation formula (Eq. E.3) derived in the previous section. This combination ensures exact integration of the polynomials in z, \bar{z} of degree up to $2M$ and exponential accuracy of angular integrations. For practical purposes, this means that the integration errors will be negligible or $N, M = 64$. This, of course, does not imply the exponential conversion of the CLE to the path integral at large N, M . The CLE introduces errors of its own, and statistical errors $O(1/\sqrt{T})$ related to the cancelation of oscillating terms are the dominant.

Appendix E.5. Holomorphic Langevin Equations

The time evolution is governed by the Complex Langevin Equation (CLE) with holomorphic drift forces derived from the total spectral action $S_{\text{total}} = S_\alpha + S_\gamma + S_T + S_\rho + S_O$.

- Coordinate Evolution (z_k):** The force on z_k arises from the boundary terms of the G functions in S_{int} and the integration limits in S_{bulk} .

$$\partial_\tau z_k = -z_k^2 \frac{\partial S_{\text{total}}}{\partial z_k} + iz_k \nu_{z_k}. \quad (\text{E.17})$$

(The factor z_k^2 arises from the metric of the map $\alpha = -i \log z$).

2. **Spinor Evolution** ($\xi_k, \tilde{\xi}_k$, etc.): The forces are computed via the chain rule through the spectral coefficients L_n . For example:

$$\partial_\tau \xi_k = -\frac{\partial S_{\text{total}}}{\partial \xi_k} - i\gamma_{1,k} \tilde{\xi}_k + \nu_{\xi_k}. \quad (\text{E.18})$$

Crucially, the noise terms ν_ξ and $\nu_{\tilde{\xi}}$ are independent complex Gaussian variables.

3. **Liouville Evolution** (ρ_k): The force on ρ_k is nonlocal, mediated by the interpolation kernel $K_k(z)$ appearing in both the bulk quadrature points and the spectral coefficients of the boundary term.

$$\partial_\tau \rho_k = -\frac{\partial S_{\text{total}}}{\partial \rho_k} + \nu_{\rho_k}. \quad (\text{E.19})$$

4. **Constraint Evolution** (γ_k): The multipliers evolve to enforce the constraints:

$$\partial_\tau \gamma_{1,k} = -i(\tilde{\xi}_k \xi_k - 1) + \nu_\gamma. \quad (\text{E.20})$$

By utilizing this spectral action, we ensure that the drift terms are analytic functions of all variables \mathcal{V} throughout the complex plane. This prevents the "excursion" problem common in standard CLE, where non-analytic projections onto the real axis lead to incorrect convergence.

Appendix E.6. Reweighted Spectral Search for Meson Masses

The poles of $\Pi(E)$ correspond to the bound state masses (the meson spectrum), and these poles also become poles of its log derivative $R(E)$.

As discussed in Section 15, directly searching for these poles in a stochastic simulation is numerically disastrous, as the infinite variance near the singularity destroys the Markov chain. Instead, we employ a reweighting method to compute the inverse ratio $1/R(E)$ and search for its zeros. This inversion mathematically transforms the meromorphic amplitude into an entire function, effectively neutralizing the singularities. We define the observable as the derivative of the action with respect to energy:

$$\begin{aligned} \mathcal{O} &= \frac{\partial S_{\text{eff}}}{\partial E} \\ &= -i \sum_{n=0}^{N-1} \sum_{m=0}^{N-1} [(L_n M_m) - (\tilde{L}_n \tilde{M}_m)] G_{n+m+1}(z_1, z_2) \end{aligned} \quad (\text{E.21})$$

Then, we have an identity

$$\Pi'(E)/\Pi(E) = \frac{\int \mathcal{O} e^{S_{\text{eff}}}}{\int e^{S_{\text{eff}}}} \quad (\text{E.22})$$

We then introduce a *Modified Action* \tilde{S} by shifting the probability measure:

$$\tilde{S} = S_{\text{eff}} + \ln \mathcal{O} \quad (\text{E.23})$$

Using this modified action, the inverse ratio can be expressed as a statistical average:

$$\frac{1}{R(E)} = \frac{\Pi(E)}{\Pi'(E)} = \frac{\int e^{S_{\text{eff}}}}{\int \mathcal{O} e^{S_{\text{eff}}}} = \frac{\int \frac{1}{\mathcal{O}} e^{\tilde{S}}}{\int e^{\tilde{S}}} = \left\langle \frac{1}{\mathcal{O}} \right\rangle_{\tilde{S}} \quad (\text{E.24})$$

Thus, the algorithm proceeds as follows:

1. We simulate the Complex Langevin evolution governed by the modified action \tilde{S} . This introduces an additional "logarithmic force" to the drift: $-\nabla \tilde{S} = -\nabla S_{\text{eff}} - \frac{1}{\mathcal{O}} \nabla \mathcal{O}$.
2. At each time step, we measure the quantity $1/\mathcal{O}$.
3. We compute the time average $\langle 1/\mathcal{O} \rangle_{\tilde{S}}$.
4. We scan the energy E and identify the meson masses as the points where this average vanishes (crosses zero).

This method transforms the search for poles into a search for zeros, which is numerically stable and precise.

Appendix E.7. Spectral Extraction and the Sign of the Slope

A crucial subtlety arises in interpreting the zeros of the measured observable. The simulation computes the expectation value of the inverse resolvent operator, $\langle \mathcal{O}^{-1} \rangle \sim \text{Re}[1/R(E)]$. To distinguish physical mass states from artifacts, we must analyze the pole structure of the resolvent.

The resolvent is related to the logarithmic derivative of the vacuum polarization $\Pi(E)$:

$$R(E) \sim \frac{\Pi'(E)}{\Pi(E)} = \frac{d}{dE} \ln \Pi(E) \quad (\text{E.25})$$

This function has singularities of two types:

1. **Physical Poles:** At a particle mass $E \approx m$, the polarization behaves as $\Pi(E) \sim \frac{A}{E-m}$. Consequently, the resolvent behaves as a simple pole with residue -1 :

$$R(E) \approx \frac{-1}{E-m} \implies \frac{1}{R(E)} \approx m - E \quad (\text{E.26})$$

2. **Polarization Zeros:** Between two physical poles, $\Pi(E)$ must cross zero. Near such a zero $E \approx E_0$, $\Pi(E) \sim C(E - E_0)$. The resolvent behaves as a simple pole with residue $+1$:

$$R(E) \approx \frac{1}{E - E_0} \implies \frac{1}{R(E)} \approx E - E_0 \quad (\text{E.27})$$

Therefore, when plotting the real part of the inverse resolvent $\text{Re}[1/R(E)]$ against energy, both physical masses and polarization zeros appear as zero-crossings. However, they are distinguished by the **sign of the slope**:

- **Negative Slope** ($\frac{d}{dE} < 0$): Corresponds to a physical particle mass (Pole of Π).

- **Positive Slope** ($\frac{d}{dE} > 0$): Corresponds to a zero of the polarization operator (Artifact).

Consequently, the meson mass spectrum is identified exclusively by the zero-crossings of $1/R(E)$ possessing a negative gradient.

Let us note in passing that this function $\Pi(E)$ in the confined planar QCD we are solving is a meromorphic function of $q^2 = -E^2$ with poles on the negative axis with positive residues:

$$\Pi(E) = \sum_n \frac{Z_n}{m_n^2 - E^2} \quad (\text{E.28})$$

We also know that asymptotically, the residues tend to $Z_n \propto \partial_n(m_n^2)$ which leads to logarithmic asymptotic behavior in the deep Euclidean limit (Asymptotic freedom):

$$\begin{aligned} \Pi(E) &\rightarrow \int dn \frac{Z_n}{m_n^2 + q^2} \\ &\propto \int_{\Lambda_{QCD}^2}^{\infty} d\sigma \frac{1}{q^2 + \sigma} \propto \text{const} + \log \frac{q^2}{\Lambda_{QCD}^2} \end{aligned} \quad (\text{E.29})$$

For our resolvent, these analytic properties mean that $1/R(E)$ is an odd *entire function*, with zeros along the real axis and no singularities in the complex plane.

Appendix E.8. Stabilizing CLE by Reweighting

The application of the Complex Langevin Equation (CLE) to theories with severe sign problems is often described as more art than science. Unlike the real Langevin equation, where the drift is derived from a real, growing at infinity action and convergence to the Boltzmann distribution is guaranteed by rigorous theorems, the CLE operates in a complexified phase space. There is no *a priori* guarantee that the stochastic process will converge to a finite limit, nor that it will sample the correct distribution. A common failure mode is the “excursion problem,” where the holomorphic variables wander into non-physical regions of the complex plane where the action is not holomorphic or simply diverges, causing the simulation to explode.

We observed precisely this instability when attempting a direct simulation of the standard effective action S_{eff} . As shown in our control tests, without modification, the magnitude of the observable \mathcal{O} diverges exponentially (reaching magnitudes of 10^{40}), rendering the extraction of physical data impossible. The drift forces derived solely from S_{eff} are insufficient to confine the system to the relevant integration domain.

The reweighting method, introduced primarily to convert the search for poles into a search for zeros, provides a crucial secondary benefit: **dynamical stabilization**. By simulating the modified action

$\tilde{S} = S_{\text{eff}} + \ln \mathcal{O}$, the drift force receives an additional contribution:

$$K_{\text{drift}} = -\nabla S_{\text{eff}} - \frac{1}{\mathcal{O}} \nabla \mathcal{O}. \quad (\text{E.30})$$

This “logarithmic force” acts as a dynamical potential barrier. When the system approaches a region where \mathcal{O} vanishes (a zero of the inverse ratio), the force becomes singular and repulsive, preventing the trajectory from crossing the zero but allowing it to explore the vicinity. Conversely, the modification of the measure appears to suppress the runaway excursions seen in the unmodified theory.

Appendix E.9. Numerical Integration: Second-Order SDE and Adaptive Braking

While the logarithmic reweighting ($\tilde{S} = S_{\text{eff}} + \log \mathcal{O}$) provides a continuous topological barrier against runaway trajectories, the discrete nature of numerical integration introduces a severe algorithmic vulnerability. In continuous Langevin time τ , steepest descent flows cannot cross the meromorphic poles at $\mathcal{O} = 0$. However, in a discrete simulation, the holomorphic drift force $K(\mathcal{V}) = -\nabla \tilde{S}$ strictly diverges near the zero-locus. A naive first-order Euler-Maruyama discretization with a fixed time step $\Delta\tau$ would generate a massive coordinate displacement $\Delta\mathcal{V} = K(\mathcal{V})\Delta\tau$ in the vicinity of the pole. This would cause the discrete trajectory to violently “jump over” the topological barrier, catapulting the system directly into the runaway Stokes wedges or triggering arithmetic overflow.

To rigorously preserve the integrity of the complexified geometry and enforce the topological barriers during discrete evolution, our numerical implementation relies on two synergistic stabilization algorithms: a second-order Stochastic Differential Equation (SDE) integrator and an adaptive drift clipping mechanism.

First, we upgrade the integration scheme from the standard Euler method to the second-order Stochastic Heun (predictor-corrector) algorithm. For a generic complex state vector \mathcal{V} , the discrete update proceeds in two stages:

$$\mathcal{V}_{\text{pred}} = \mathcal{V}(\tau) + \Delta\mathcal{V}_1 + \eta(\tau) \sqrt{\Delta\tau} \quad (\text{Predictor}) \quad (\text{E.31})$$

$$\begin{aligned} \mathcal{V}(\tau + \Delta\tau) = \\ \mathcal{V}(\tau) + \frac{1}{2} \left(\Delta\mathcal{V}_1 + \Delta\mathcal{V}_2 \right) + \eta(\tau) \sqrt{\Delta\tau} \quad (\text{Corrector}) \end{aligned} \quad (\text{E.32})$$

where $\Delta\mathcal{V}_1 = K(\mathcal{V}(\tau))\Delta\tau$ and $\Delta\mathcal{V}_2 = K(\mathcal{V}_{\text{pred}})\Delta\tau$. The complexified Gaussian noise $\eta(\tau)$ is identical in both steps. By sampling the drift at both the current state and the projected future state, the predictor-corrector averaging intrinsically accounts for the severe local curvature of the effective action, providing vastly superior stability

when navigating the highly non-linear valleys of the Lefschetz thimbles.

Second, to absolutely forbid discrete overshoots near the meromorphic poles and the bounding walls of the non-compact Liouville directions, we implement dynamic “braking” via adaptive drift clipping. At both the predictor and corrector stages, we compute the maximum proposed deterministic displacement, $\delta_{max} = \max |\Delta\mathcal{V}_i|$, across all degrees of freedom. If this proposed step exceeds a strict geometric safety threshold ϵ (in our production runs, $\epsilon = 0.05$), we isotropically rescale the entire drift vector:

$$\Delta\mathcal{V}_i \rightarrow \Delta\mathcal{V}_i \left(\frac{\epsilon}{\delta_{max}} \right) \quad \text{for } \delta_{max} > \epsilon \quad (\text{E.33})$$

This operation is mathematically equivalent to an adaptive, localized reduction of the Langevin time step ($\Delta\tau \rightarrow \Delta\tau_{eff}$) during violent excursions.

Physically, this acts as an automatic braking system. In the flat, safe regions of the bulk phase space, the simulation explores efficiently with the full time step $\Delta\tau$. But the moment the complexified noise kicks the trajectory toward a singularity, the repulsive drift spikes, and the adaptive clipping safely throttles the velocity. The trajectory slows to a crawl, taking infinitesimally fine integration steps that smoothly trace the repulsive contours of the meromorphic pole. This ensures that the discrete trajectory gently reflects off the $1/\mathcal{O}$ topological barriers rather than numerically tearing through them, preserving the structural integrity of the complexified path integral over billions of consecutive updates.

Appendix E.10. Analyzing intermittent histories of the Complex Langevin Equation

The numerical evaluation of the twistor-string path integral via the Complex Langevin Equation (CLE) introduces profound statistical challenges. The physical observable required for the spectrum extraction, $1/\mathcal{O}$, is meromorphic. Consequently, during the stochastic evolution, the complexified trajectory occasionally wanders near the singularity at $\mathcal{O} = 0$. These close encounters generate violent, intermittent numerical spikes—or excursions—in the micro-state history. Extracting the pristine physical signal from this complexified noise requires a rigorous pipeline of burn-in truncation, dynamic symmetry restoration, and Cauchy Principal Value error bounding.

Thermalization and the Measurement Criterion

Because the CLE simulation is initialized from an arbitrary complex configuration, the early micro-state history is dominated by a massive coordinate drift as the system relaxes toward the true vacuum. Including this non-equilibrium initial phase would severely pollute the physical averages.

To rigorously determine the exact step N_{cut} where this “burn-in” phase ends, we utilize the raw imaginary trajectory, $\text{Im}[1/\mathcal{O}]$, as an exact equilibrium thermometer. The exact, uncomplexified path integral respects a global $Z \leftrightarrow Z^*$ parity. Consequently, the steady-state Fokker-Planck distribution of the CLE must eventually become symmetric with respect to the real axis. The strict criterion for thermalization is therefore the cessation of macroscopic secular drift in the imaginary component. As illustrated in the full raw history (Fig. E.16, left), the measurement phase is initiated only after this trajectory stabilizes into a horizontal stochastic oscillation. We discard all data prior to this threshold (e.g., $N_{cut} = 100000$).

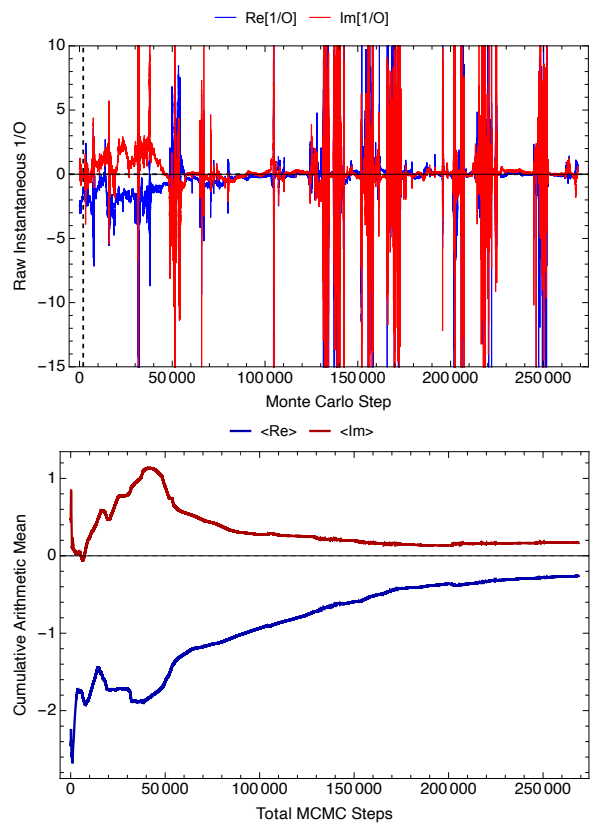


Figure E.16: Left: The raw intermittent history of the CLE trajectory. The vertical dashed line marks the strict measurement criterion (N_{cut}) where macroscopic secular drift ceases. All prior data is discarded. Right: The naive cumulative arithmetic mean. Post-thermalization excursions permanently offset the mean, demonstrating the fragility of unweighted averaging.

Dynamic Symmetry Restoration

At finite Langevin times, the stochastic trajectory can become temporarily trapped in one complex half-plane, leading to a delayed restoration of the $Z \leftrightarrow Z^*$ parity. We bypass this topological tunneling lag through *Dynamic Symmetry Restoration*. Because the theoretical ensemble is invariant under

complex conjugation, we explicitly symmetrize the post-burn-in history. By adding the complex conjugate of every generated micro-state to the dataset, we artificially and instantly enforce the parity symmetry, projecting the stochastic fluctuations entirely onto the real physical slice (Fig. E.17).

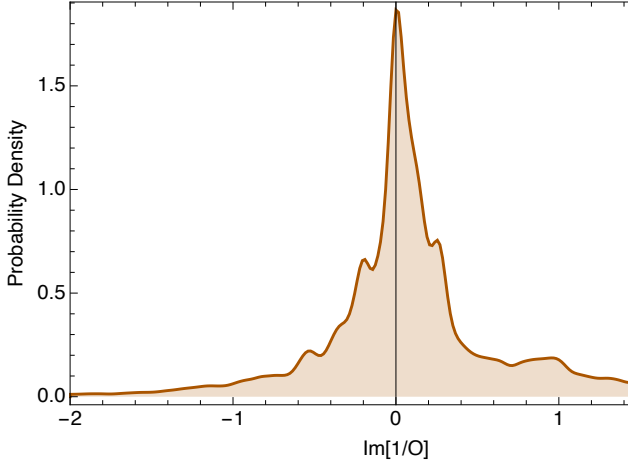


Figure E.17: Kernel Density Estimation of $\text{Im}[1/\mathcal{O}]$ during the valid measurement phase. The bounded peak near zero confirms statistical equilibrium. Any residual skewness is instantly annihilated by the $Z \leftrightarrow Z^*$ double-history symmetrization.

The $1/|u|^3$ Singularity and the Principal Value

The physical core of the real distribution, $\text{Re}[1/\mathcal{O}]$, is highly multimodal (Fig. E.18, left), reflecting instanton-like tunneling between discrete topological sectors (Lefschetz thimbles). However, the excursions generate a severe statistical pathology.

Assuming the probability density of the complexified micro-states is finite and approximately uniform near the origin, $P(\text{Re}[\mathcal{O}], \text{Im}[\mathcal{O}]) \approx p_0$, we can analytically determine the asymptotic distribution of the inverse observable $u = \text{Re}[1/\mathcal{O}]$. Transforming to polar coordinates and integrating over the complex plane yields an exact power-law:

$$P(u) \approx \int p_0 \delta\left(u - \frac{\cos\theta}{r}\right) r dr d\theta = \frac{\pi p_0}{2|u|^3} \quad (\text{E.34})$$

This exact $1/|u|^3$ power-law behavior dictates that while the theoretical mean is finite, the variance diverges logarithmically ($\int u^2/|u|^3 du \rightarrow \infty$). Consequently, the standard empirical arithmetic mean is formally ill-defined in finite samples; it is continuously hijacked by infinite-variance sample noise (Fig. E.16, right).

Because the leading asymptotic tail is exactly symmetric ($P(u) = P(-u)$), the divergent variance contributions from the extreme left and right excursions mathematically cancel. Therefore, the physical expectation value of the amplitude must be

rigorously defined via the Cauchy Principal Value (PV). To extract this regularized observable, we utilize a Symmetric Trimmed Mean (clipping the extreme $q = 5\%$ of positive and negative outliers). By symmetrically shearing off the infinite-variance tails, it acts as the exact numerical implementation of the Principal Value, isolating the finite thermodynamic center of mass over the central 90% of the physical bulk.

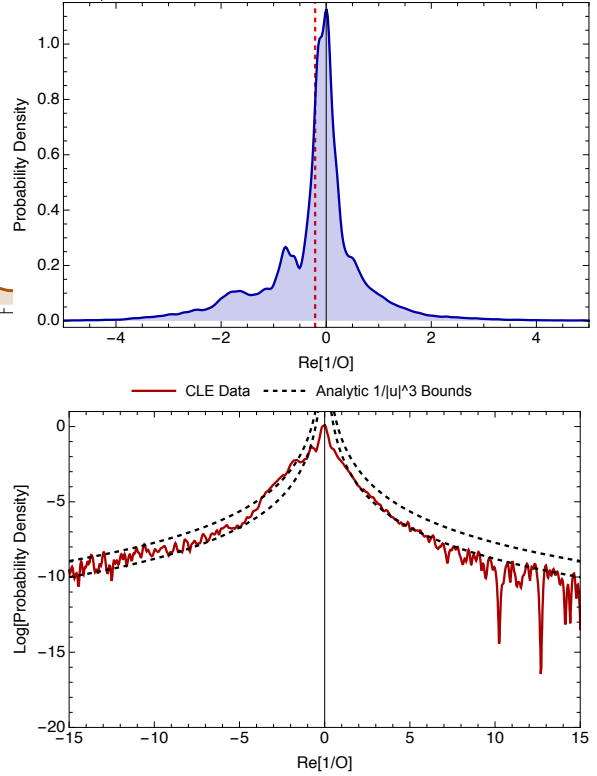


Figure E.18: Upper: The multimodal physical core of $\text{Re}[1/\mathcal{O}]$. The robust trimmed mean (red dashed line) isolates the true Principal Value. Lower: Log-scaled probability density demonstrating the severe asymptotic $1/|u|^3$ power-law tails (black dashed lines), which cause infinite variance and necessitate Cauchy Principal Value regularization.

Exact Analytic Error Bounding and Regression Weights

To rigorously bound the systematic statistical error introduced by discarding these numerical excursions, we exploit the analytic form of the asymptotic tails $P(u) = C/|u|^3$. For the right tail (values exceeding the $1 - q$ quantile threshold u_R), the normalization constant is fixed by the trim fraction q :

$$\int_{u_R}^{\infty} \frac{C_R}{u^3} du = \frac{C_R}{2u_R^2} = q \implies C_R = 2qu_R^2 \quad (\text{E.35})$$

The exact thermodynamic contribution of this infinite right tail evaluates to $\int_{u_R}^{\infty} u (2qu_R^2/u^3) du = 2qu_R$. By identical logic, the left tail contribution evaluates to $2qu_L$. Thus, the exact reconstructed

Principal Value mean is a parameter-free sum of the trimmed core (μ_{core}) and the analytic tail boundaries:

$$\langle \text{Re}[1/\mathcal{O}] \rangle_{\text{total}} = (1 - 2q)\mu_{\text{core}} + 2q(u_R + u_L) \quad (\text{E.36})$$

The difference between the symmetric trimmed mean and this full analytic reconstruction, $\Delta_{\text{tail}} = 2q|u_R + u_L - \mu_{\text{core}}|$, provides a strict mathematical measure of the finite-sample Principal Value asymmetry (Table E.2).

Beyond bounding the mean, the exact $1/|u|^3$ geometry strictly determines the statistical variance of the Markov chain. This variance is required for the optimal inverse-variance pooling of independent cluster nodes and for weighting the polynomial regression used to extract the mass spectrum. Because the probability density decays as $1/|u|^3$, the formal variance diverges logarithmically with the maximum Langevin excursion cutoff L . Evaluating the second moment for the right tail yields:

$$\begin{aligned} \sigma_R^2 &= \int_{u_R}^L u^2 \left(\frac{2qu_R^2}{u^3} \right) du = \\ &2qu_R^2 \log\left(\frac{L}{u_R}\right) \rightarrow 2qu_R^2 \log L \end{aligned} \quad (\text{E.37})$$

Combining the identically regulated contribution from the left tail, the total empirical variance of the numerical history diverges logarithmically as:

$$\sigma^2 \simeq 2q(u_R^2 + u_L^2) \log L \quad (\text{E.38})$$

Crucially, because the maximum Langevin excursion extent L acts as a universal scale factor across the parallel Monte Carlo ensemble, the formally divergent $\log L$ completely cancels out when constructing the normalized inverse-variance weights ($w_i \propto 1/\sigma_i^2$) for the polynomial regression. Therefore, the optimal statistical weight for each independent energy point is governed entirely by the parameter-free relative variance of its physical core:

$$\sigma_{\text{rel}}^2 = q(u_R^2 + u_L^2) \quad (\text{E.39})$$

By replacing heuristic error estimation with this exact geometric variance, the fitting procedure becomes statistically bulletproof. Any node that suffers a violent, parity-violating topological excursion will exhibit drastically widened boundaries ($u_R^2 + u_L^2 \rightarrow \infty$), naturally driving its statistical weight to exactly zero. This rigorously guarantees that the final extracted Regge trajectory is determined strictly by the thermalized, parity-preserving vacuum configurations of the Complex Langevin dynamics.

Appendix E.11. First computations of the meson spectrum

Empirically, we find that this reweighted CLE is numerically stable over extremely long integration times. In production runs extending to 10^6 time steps per node per energy value (corresponding

Parameter	Sym.	Value
Trimmed Core	μ_{core}	-0.210137
Left Cut (5%)	u_L	-2.103169
Right Cut (95%)	u_R	1.230750
Analytic PV Mean	μ_{tot}	-0.276365
Asym. PV Error	Δ_{tail}	± 0.066228

Table E.2: Analytic bounds on finite-sample Cauchy Principal Value (PV) asymmetry, derived from exact $1/|u|^3$ Langevin excursions.

to a Langevin time of $\tau \sim 10^4$), the observable $1/\mathcal{O}$ remains finite and oscillates within a bounded range (typically $\in [-20, 20]$), with no sign of the divergences characterizing the unweighted dynamics. While there is no general theorem proving that logarithmic reweighting stabilizes all complex actions, in the specific context of the Twistor String, it effectively regularizes the stochastic evolution, allowing for high-precision spectroscopy. Our cumulative statistics on all nodes for all 480 energy points per energy value is about one billion data points. The lack of instabilities in such a large dataset speaks for some form of statistical equilibrium.

The code implementing the above algorithm was written in *Mathematica*[®] [52] and simulated on the IAS supercluster Typhon using a high-precision grid: 64 angular nodes and 32 radial nodes in the Gauss-Legendre computation of the Liouville energy integral. We employed a Langevin time step $dt = 0.0005$ and averaged the inverse resolvent $1/R(m)$ over 48 physical hours, following a thermalization period of 2.4 hours. The number of time steps was approximately $T_{\text{tot}} = 17M$, and the total Langevin time spent was $\tau = T_{\text{tot}} * dt \approx 8500$.

The computation was parallelized across 64 nodes of the Typhon cluster. Each node, equipped with 24 cores, ran an independent Langevin evolution initialized with a unique random seed. The energy spectrum was sampled over $N_E = 10 \times N_{\text{cores}} = 240$ values equally spaced between 2. and 3.0 in units of string tension σ . The calculation was computationally intensive, requiring two days of wall-clock time on each of the 64 nodes to achieve the necessary convergence.

The results of this simulation are presented in Figures E.16, E.18 and 15. The first plot displays the full history of real part of the inverse resolvent, $\text{Re}[1/R(m)]$, for a particular energy parameter $E = 2.27197$. The second plot is the distribution of this real part over the measurement period (after first 100K steps). The third plot displays the roots of $1/R(E)$ with a negative slope in a form of the Regge trajectory n vs m_n^2 . As derived in Section Appendix E.7, the physical meson mass spectrum is identified by the zero-crossings of this function that possess a **negative slope**. There are

two different branches of Regge trajectory, both close to linear (note that n represents the internal excitation number, not the angular momentum). The label distinguishing these two branches corresponds to the internal quantum number of the $\bar{q}q$ states in our Confining Twistor theory. We identified these two branches by the information clustering method described in Section 16.

The simulation demonstrates certain stability:

- **Robustness:** The process remained bounded without "runaways" or numerical explosions, confirming the efficacy of the holographic bulk forces in stabilizing the non-compact gauge variables.
- **Precision:** The histograms are smooth and have symmetric power tails, matching theoretical prediction $1/|u|^3$
- **Spectrum:** Information clustering of negative crossings by information produced two Regge trajectories, approximately linear with the same slope.

While the current simulation parameters are sufficient to establish a proof of concept, we acknowledge that a detailed spectroscopic analysis—particularly to resolve the fine structure of high-mass resonances—requires higher resolution and significantly larger statistics. However, the existing code [52] is fully capable of addressing this challenge without modification. The implementation is highly efficient and parallelized, maintaining numerical stability even at the high grid densities required for Gauss-Legendre integration, angular FFTs, and Lagrange interpolation.

Appendix F. Canonical Twistors and the Minkowski Helicoid Metric

In this appendix, we explicitly derive the macroscopic worldsheet metric of the rotating string directly from the microscopic twistor fields. We demonstrate how the canonical twistor parameterization enforces a dimensional reduction to a 3D hyperplane, and how the double Wick rotation analytically continues the Euclidean twistor metric into the physical Minkowski Nambu-Goto metric. We then pedantically evaluate the resulting bulk action integral.

Appendix F.1. Canonical Twistors and Dimensional Reduction

The canonical Helicoid is generated by twistors endowed with fractional powers of the worldsheet coordinate z . This fractional scaling is a spin-structure gauge choice that explicitly enforces the Neveu-Schwarz anti-periodic boundary conditions for the worldsheet fermions as they complete a full

rotation around the string center. We define the left and right twistors as:

$$\begin{aligned}\lambda(z) &= e^{i\pi/4} z^{-1/2} \begin{pmatrix} 1/z \\ 1 \end{pmatrix}, \\ \mu(z) &= ie^{-i\pi/4} z^{1/2} \begin{pmatrix} 1 \\ -z \end{pmatrix}\end{aligned}\quad (\text{F.1})$$

Because $\lambda \propto z^{-1/2}$ and $\mu \propto z^{1/2}$, their product has no overall fractional branching. The resulting bosonic physical observables are strictly rational, making this configuration geometrically equivalent to a rational single-pole state.

The defining geometric characteristic of this canonical configuration is its behavior under the symmetric Pauli matrices. The spatial tangent vectors of the minimal surface are constructed via $f'_k \propto \lambda^T \sigma_k \mu$. Evaluating the symmetric bilinear for the first spatial component:

$$\begin{aligned}f'_1 &\propto \lambda^T \sigma_1 \mu = \lambda_1 \mu_2 + \lambda_2 \mu_1 \\ &= i \left[\left(\frac{1}{z} \right) (-z) + (1)(1) \right] = i(-1 + 1) = 0\end{aligned}\quad (\text{F.2})$$

Because the tangent vector component f'_1 vanishes identically everywhere on the worldsheet, the target space coordinate X_1 is strictly constant. This exact algebraic constraint dynamically crushes the generic 4-dimensional minimal surface into a 3-dimensional hyperplane, forming the exact topological skeleton of the macroscopic 3D Helicoid.

Appendix F.2. The Euclidean Metric and Double Wick Rotation

To extract the physical string metric, we compute the induced conformal factor $\exp(2\rho) = |\lambda|^2 |\mu|^2$. Restoring the dimensionful scale parameter R , the squared norms are:

$$\begin{aligned}|\lambda|^2 &= \frac{R}{|z|} \left(\frac{1}{|z|^2} + 1 \right) = R \frac{1 + |z|^2}{|z|^3}, \\ |\mu|^2 &= R|z| (1 + |z|^2)\end{aligned}\quad (\text{F.3})$$

When multiplied, the fractional $|z|$ weights cancel perfectly:

$$\exp(2\rho) = R^2 \frac{(1 + |z|^2)^2}{|z|^2} = R^2 \left(|z| + \frac{1}{|z|} \right)^2 \quad (\text{F.4})$$

To map this conformal geometry to the natural coordinates of the string worldsheet, we transition from the complex plane to the Euclidean cylinder via $z = \exp(\sigma_E + i\tau_E)$. The flat integration measure transforms as $dzd\bar{z}/|z|^2 = d\sigma_E^2 + d\tau_E^2$. Substituting $|z| = \exp(\sigma_E)$, the conformal factor becomes:

$$\exp(2\rho) = R^2 (e^{\sigma_E} + e^{-\sigma_E})^2 = 4R^2 \cosh^2(\sigma_E) \quad (\text{F.5})$$

Thus, the induced Euclidean worldsheet metric is exactly:

$$ds_E^2 = \exp(2\rho) \frac{dzd\bar{z}}{|z|^2} = 4R^2 \cosh^2(\sigma_E) (d\sigma_E^2 + d\tau_E^2) \quad (\text{F.6})$$

To evaluate the physical states, we analytically continue this metric into Minkowski spacetime via a double Wick rotation. The angular parameter τ_E serves as the target space time. We perform a Wick rotation on the spatial worldsheet coordinate into the physical light-cone regime:

$$\sigma_E = i\sigma_M \implies d\sigma_E^2 = -d\sigma_M^2 \quad (\text{F.7})$$

Under this transformation, the hyperbolic cosine strictly rotates into the trigonometric cosine: $\cosh(i\sigma_M) = \cos(\sigma_M)$. Extracting an overall minus sign to reflect the intrinsic Lorentzian $(-, +)$ worldsheet signature, the exact Minkowski metric is:

$$ds_M^2 = 4R^2 \cos^2(\sigma_M) (d\tau_E^2 - d\sigma_M^2) \quad (\text{F.8})$$

To explicitly verify that this describes the canonical rotating string, we change from the conformal spatial coordinate σ_M to the physical target space radial coordinate r . For a rigidly rotating string, the fractional radius is $r = \sin(\sigma_M)$. The differentials transform as:

$$dr = \cos(\sigma_M)d\sigma_M \implies dr^2 = \cos^2(\sigma_M)d\sigma_M^2 \quad (\text{F.9})$$

Simultaneously, the time component of the metric incorporates the trigonometric identity $\cos^2(\sigma_M) = 1 - \sin^2(\sigma_M) = 1 - r^2$. Substituting these directly into the Minkowski metric, we obtain:

$$ds_M^2 = 4R^2 [(1 - r^2)d\tau_E^2 - dr^2] \quad (\text{F.10})$$

This flawlessly reproduces the canonical Nambu-Goto metric $\propto (1 - r^2)dt^2 - dr^2$ for a macroscopic string rotating at the speed of light.

Appendix F.3. Action Evaluation and the Lüscher Shift

Finally, we pedantically evaluate the total effective action over the fundamental domain of this Minkowski metric. The determinant of the conformal Minkowski metric $ds_M^2 = 4R^2 \cos^2(\sigma_M)(d\tau_E^2 - d\sigma_M^2)$ is $-g = 16R^4 \cos^4(\sigma_M)$, yielding the exact proper area measure:

$$\sqrt{-g} = 4R^2 \cos^2(\sigma_M) \quad (\text{F.11})$$

The center of the rotating string lies at $r = 0$ ($\sigma_M = 0$), and the physical speed-of-light boundary is at $r = 1$ ($\sigma_M = \pi/2$). For one full spatial period of the meson, the time coordinate wraps exactly one cycle: $\tau_E \in [0, 2\pi]$. The exact classical Minkowski area integral is therefore:

$$\begin{aligned} \text{Area} &= \int_0^{2\pi} d\tau_E \int_0^{\pi/2} 4R^2 \cos^2(\sigma_M) d\sigma_M \\ &= (2\pi)(4R^2) \left(\frac{\pi}{4}\right) = 2\pi^2 R^2 \end{aligned} \quad (\text{F.12})$$

Simultaneously, the Liouville action dictates that the worldsheet carries the kinetic anomaly $\frac{1}{12\pi}|\nabla\rho|^2$. Because the kinetic anomaly density shares the exact same spatial singularity as the

conformal area density at the twistor pole, it mathematically merges into the classical area term. As established in the main text, it acts strictly as a rigid, local shift to the effective string tension:

$$\sigma_{\text{eff}} = \sigma + \frac{1}{12\pi R^2} \quad (\text{F.13})$$

Multiplying the classical Minkowski area by this effective tension, we obtain the complete 1-cycle bulk action:

$$\begin{aligned} S_{\text{bulk}}^{(1)} &= -\sigma_{\text{eff}} \times \text{Area} \\ &= -\left(\sigma + \frac{1}{12\pi R^2}\right) (2\pi^2 R^2) \\ &= -2\pi^2 \sigma R^2 - \frac{\pi}{6} \end{aligned} \quad (\text{F.14})$$

This rigorous derivation explicitly demonstrates that the universally mandated $-\pi/6$ Lüscher phase is identically generated by the exact geometric mapping of the twistor string to the Minkowski cylinder.